

*Annual Review of Astronomy and Astrophysics*  
Quasars and the Intergalactic  
Medium at Cosmic Dawn

Xiaohui Fan,<sup>1</sup> Eduardo Bañados,<sup>2</sup>  
and Robert A. Simcoe<sup>3</sup>

<sup>1</sup>Steward Observatory, University of Arizona, Tucson, Arizona, USA; email: xfan@arizona.edu

<sup>2</sup>Max-Planck-Institut für Astronomie, Heidelberg, Germany; email: banados@mpia.de

<sup>3</sup>MIT Kavli Institute for Astrophysics and Space Research, Cambridge, Massachusetts, USA;  
email: simcoe@space.mit.edu

Annu. Rev. Astron. Astrophys. 2023. 61:373–426

First published as a Review in Advance on  
June 12, 2023

The *Annual Review of Astronomy and Astrophysics* is  
online at [astro.annualreviews.org](http://astro.annualreviews.org)

<https://doi.org/10.1146/annurev-astro-052920-102455>

Copyright © 2023 by the author(s). This work is licensed under a Creative Commons Attribution 4.0 International License, which permits unrestricted use, distribution, and reproduction in any medium, provided the original author and source are credited. See credit lines of images or other third-party material in this article for license information.

ANNUAL  
REVIEWS **CONNECT**

[www.annualreviews.org](http://www.annualreviews.org)

- Download figures
- Navigate cited references
- Keyword search
- Explore related articles
- Share via email or social media

## Keywords

supermassive black hole, galaxy evolution, cosmic reionization

## Abstract

Quasars at cosmic dawn provide powerful probes of the formation and growth of the earliest supermassive black holes (SMBHs) in the Universe, their connections to galaxy and structure formation, and the evolution of the intergalactic medium (IGM) at the epoch of reionization (EoR). Hundreds of quasars have been discovered in the first billion years of cosmic history, with the quasar redshift frontier extended to  $z \sim 7.6$ . Observations of quasars at cosmic dawn show the following:

- The number density of luminous quasars declines exponentially at  $z > 5$ , suggesting that the earliest quasars emerge at  $z \sim 10$ ; the lack of strong evolution in their average spectral energy distribution indicates a rapid buildup of the active galactic nucleus environment.
- Billion-solar-mass black holes (BHs) already exist at  $z > 7.5$ ; they must form and grow in less than 700 Myr, by a combination of massive early BH seeds with highly efficient and sustained accretion.
- The rapid quasar growth is accompanied by strong star formation and feedback activity in their host galaxies, which show diverse morphological and kinetic properties, with typical dynamical mass lower than that implied by the local BH/galaxy scaling relations.

- H $\alpha$  absorption in quasar spectra probes the tail end of cosmic reionization at  $z \sim 5.3$ –6 and indicates the EoR midpoint at  $6.9 < z < 7.6$ , with large spatial fluctuations in IGM ionization. Observations of heavy element absorption lines suggest that the circumgalactic medium also experiences evolution in its ionization structure and metal enrichment during the EoR.

## Contents

|  |     |
|--|-----|
| 1. INTRODUCTION .....  | 374 |
| 2. THE QUASAR REDSHIFT FRONTIER .....  | 376 |
| 2.1. Progress in High-Redshift Quasar Surveys .....                                      | 376 |
| 2.2. Optimization of Photometric Selection of High-Redshift Quasars .....                | 379 |
| 2.3. A Database of $z > 5.3$ Quasars .....   | 381 |
| 2.4. Future Quasar Surveys .....   | 382 |
| 3. AN EVOLVING QUASAR POPULATION .....   | 383 |
| 3.1. Evolution of the Quasar Luminosity Function .....                                   | 383 |
| 3.2. (A Lack of) Evolution of the Quasar Spectral Energy Distributions .....             | 385 |
| 4. GROWTH OF SUPERMASSIVE BLACK HOLES IN THE<br>FIRST BILLION YEARS .....                | 388 |
| 4.1. Black Hole Mass Measurements in High-Redshift Quasars .....                         | 389 |
| 4.2. Current Demographics .....  | 390 |
| 4.3. Constraints on Early Black Hole Seeds and Growth .....                              | 391 |
| 4.4. The (Near) Future for Black Hole Mass Measurements at High Redshift .....           | 392 |
| 5. A MULTIWAVELENGTH VIEW OF QUASAR/GALAXY<br>COEVOLUTION AT THE HIGHEST REDSHIFTS ..... | 393 |
| 5.1. Quasar Fueling: Ly $\alpha$ Nebulae .....   | 393 |
| 5.2. Quasar Host Galaxy Observations: Sites of Massive Galaxy Evolution .....            | 394 |
| 5.3. Constraints on Galaxy Mass and Black Hole/Galaxy Coevolution .....                  | 397 |
| 5.4. Evidence of Quasar Feedback .....   | 399 |
| 5.5. Protoclusters and Large-Scale Structure .....                                       | 400 |
| 6. QUASARS AS PROBES OF COSMIC REIONIZATION .....  | 401 |
| 6.1. Active Galactic Nuclei and the Ionizing Photon Budget .....                         | 402 |
| 6.2. Neutral Hydrogen Absorption in the Diffuse Intergalactic Medium .....               | 402 |
| 6.3. Neutral Hydrogen Absorption in the Quasar Environment .....                         | 410 |
| 6.4. Heavy Element Enrichment of Intervening Quasar Absorbers .....                      | 415 |
| 6.5. Metal Absorption in the Vicinity of Quasi-Stellar Object Hosts .....                | 417 |
| 7. SUMMARY .....   | 418 |

## 1. INTRODUCTION

Quasars, and active galactic nuclei (AGNs) in general, are powered by accretion onto the supermassive black holes (SMBHs) at the center of their host galaxies. Quasars are the most luminous nontransient sources in the Universe and have been observed up to a redshift of  $z \sim 7.6$  (Wang et al. 2021b). SMBH activities are a key ingredient of galaxy formation. Quasars provide crucial probes of galaxy evolution and cosmology across cosmic history at three critical spatial scales:

1. At the scale of the AGN central engine ( $< 1$  pc), quasar emission originates from well within the SMBH sphere of influence, at which the gravitational influence of the black hole (BH) dominates. Quasars are fundamental in understanding the physics of BH accretion and growth and the physics of AGN activity.
2. At the scale of quasar host galaxies ( $\sim 1$ – $10$  kpc), the evolution of quasars and galaxies are strongly coupled, as shown by the tight correlation between SMBH mass and the mass/velocity dispersion of their host galaxies seen at low redshift (e.g., the  $M$ - $\sigma$  relation; Kormendy & Ho 2013). Quasars are key to understanding the assembly, growth, and quenching of massive galaxies.
3. At the scale of galaxy clusters and superclusters ( $> 1$  Mpc), quasars can be used to probe the growth of early large-scale structure. They also provide sightlines to study the properties of the intergalactic medium (IGM), including the history of cosmic reionization, the chemical enrichment of the IGM, the distribution of baryons, and the evolution of the ionization state of the IGM and its connection to galaxy formation through the circumgalactic medium (CGM).

The history of quasar studies is driven and shaped by innovations in systematic surveys and multiwavelength observations of quasars. These observations aim toward reaching higher redshifts, covering the full range of quasar luminosities, and spatially resolving quasar hosts and their central AGN structure. Studies of high-redshift quasars within the first few billion years of cosmic history started with the advent of large-area digital or digitized sky surveys, highlighted by progress made using data from the Sloan Digital Sky Survey (SDSS; York et al. 2000), which resulted in the first detections of quasars at  $z > 5$  and  $z > 6$  (Fan et al. 2001). Observations of  $z \sim 6$  quasars in the early 2000s provided fundamental insights in the three key scales of galaxy evolution mentioned above:

1. SMBHs with masses up to a few billion solar masses already existed in the Universe within one billion years after the Big Bang, requiring a combination of early massive BH seeds and rapid BH accretion.
2. Early luminous quasars are sites of intensive galaxy-scale star formation and the assembly of early massive galaxies.
3. Detection of strong IGM absorption in quasar spectra, especially the emergence of complete Gunn–Peterson absorption troughs (Gunn & Peterson 1965), shows a rapid transition of the ionization state of the IGM at  $z \sim 5$ – $6$ , marking this epoch as the end of cosmic reionization.

In this review, we focus on the progress since then, including the quests for the earliest quasars, and the detailed studies of quasars during and right after the epoch of reionization (EoR). We limit our discussions to (a) the redshift range of  $z > 5.3$ ; this is the lower redshift limit at which there are still detectable signatures of reionization activity. This redshift corresponds to 1.1 Gyr after the Big Bang, when the Universe was at 8% of its current age. We consider  $z > 5.3$  as “cosmic dawn” in the context of this review; (b) luminous type-1 quasars, for which secure spectroscopic observations and systematic surveys are currently possible; and (c) IGM studies using quasar absorption spectra. We do not discuss other probes of EoR in detail. This review focuses mainly on observations, and we discuss theories and simulations largely in the context of understanding and predicting observations.

At the time of this review, the *James Webb Space Telescope* (JWST) has started routine observations, and initial JWST results have begun to appear in the literature. We do not include any early JWST results in this article. JWST observations of high-redshift quasars will undoubtedly

provide many new insights that result in discoveries and challenges that should be the subject of a future review.

There have been a number of excellent Annual Review articles on related topics that we will not repeat: Inayoshi et al. (2020) reviewed topics related to the initial BH seeds and early growth; Kormendy & Ho (2013) presented a very detailed discussion of BH/galaxy coevolution; Carilli & Walter (2013) reviewed early [pre-ALMA (Atacama Large Millimeter/submillimeter Array)] millimeter/submillimeter observations of high-redshift galaxies, including quasar hosts. Fan et al. (2006a) discussed early observational studies of reionization; McQuinn (2016) provided a general discussion of the evolution of the IGM.

This review is organized as follows: In Section 2, we review the progress in searching for the highest-redshift quasars and in establishing a large sample of quasars at cosmic dawn, as a result of the new generations of wide-field sky surveys and the developments in data mining and machine learning. In this section, we present a database of all published type-1 quasars at  $z > 5.3$ . In Section 3, we discuss the evolution of quasars as a population at high redshift, presenting the measurements of the quasar luminosity function (QLF), and the trend in the evolution of quasar intrinsic properties in early epochs. We also highlight special populations of high-redshift quasars. In Section 4, we discuss the use of high-redshift quasars as probes of the history of SMBH growth in the early Universe and review statistics of measurements of quasar BH masses and accretion characteristics. In Section 5, we review the observations of quasar host galaxies from the rest-frame UV to far-IR (FIR) bands, in the context of the coevolution of early SMBH growth and galaxy formation, and the roles quasars played in early galaxy and structure formation. In Section 6, we review the progress in using IGM absorption in quasar sightlines and properties of quasar proximity zones to probe the history of cosmic reionization and IGM chemical enrichment. Throughout this review, we assume a spatially flat lambda cold dark matter (LCDM) cosmological model with  $\Omega_m = 0.3$  and  $H_0 = 70 \text{ km s}^{-1} \text{ Mpc}^{-1}$ , consistent with the final Planck results.

## 2. THE QUASAR REDSHIFT FRONTIER

Advances in the studies of high-redshift quasars are first and foremost driven by advances in high-redshift quasar surveys and new discoveries. The quasar redshift frontier continues to expand as a result of new sky surveys: The first quasar discoveries at  $z > 4$  in the 1980s were made possible by digital or digitized large sky surveys and the first implementations of color drop-out selection techniques (e.g., Warren et al. 1987). After the SDSS discoveries of the first  $z > 5$  (Fan et al. 1999) and  $z > 6$  (Fan et al. 2001) quasars in the early 2000s, wide-field near-IR (NIR) sky surveys in the following decade, such as U.K. Infrared Deep Sky Survey (UKIDSS) (Lawrence et al. 2007), led to the detection of the first quasars at  $z > 7$  (e.g., Mortlock et al. 2011), deep into the EoR. At the time of this review, the quasar redshift frontier stands at  $z = 7.64$  (Wang et al. 2021b). Meanwhile, increasingly large samples of high-redshift quasars are established by continued mining and systematic spectroscopic follow-up observations based on these new surveys. Currently, about 1,000 quasars have been discovered at  $z > 5$ , and more than 200 at  $z > 6$ .

### 2.1. Progress in High-Redshift Quasar Surveys

Surveys of the highest-redshift quasars face three technical challenges. First, quasars at cosmic dawn are among the rarest objects in the Universe. The final SDSS  $z \sim 6$  quasar sample covers more than  $11,000 \text{ deg}^2$  but contains only 52 quasars (Jiang et al. 2016). Their discoveries require large surveys that cover a significant fraction of the sky. The second challenge is often referred to as “finding needles in a haystack.” Most high-redshift quasar surveys are based on Lyman-break dropout selections using optical and NIR photometric survey data. However, other populations of

celestial objects, in particular cool galactic dwarfs with spectral types M, L, and T (usually referred as MLTs) and compact early-type intermediate-redshift galaxies, have similar optical and NIR colors. Barnett et al. (2019) show that these contaminant populations outnumber  $z \sim 7$  quasars by 2–4 orders of magnitude in deep photometric surveys. A number of photometric selection techniques have been developed, and the choices of how to apply these techniques require careful consideration of the balance between selection efficiency and completeness. Finally, spectroscopic identifications of candidate quasars require observations on large aperture telescopes. Until recently, such observations were only possible with single-object spectroscopy because of the low spatial density of high-redshift quasars. The demand of telescope resources for discovery drives the need for both high selection efficiency and sometimes special observing strategies. For example, Wang et al. (2017) improved spectroscopic identification efficiency by using low-resolution ( $R \sim 300$ ) long-slit NIR spectroscopy, which could capture the prominent Lyman-break features in the quasar spectra and reject contaminants with shorter exposures than higher-resolution spectra (which is more common for quasar spectroscopy follow-up work).

**Figure 1** presents the distribution of all published  $z \geq 5.3$  quasars, as of December 2022, on the absolute magnitude–redshift plane, highlighting the major survey programs from which most of these quasars are selected. The progress illustrated in **Figure 1b** is a result of the availability

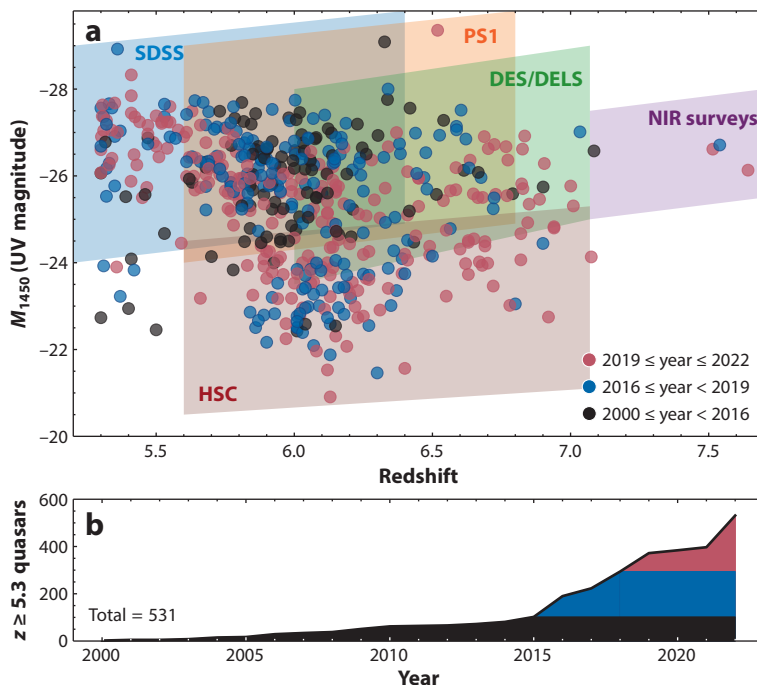


**Figure 1**

(a) Distribution of all known  $z \geq 5.3$  quasars in the absolute magnitude–redshift plane. The shaded areas are the parameter space probed by selected large quasar survey programs. (b) The cumulative number of quasars known at  $z \geq 5.3$  as a function of year of publication. Abbreviations: DES, Dark Energy Survey; DELS, DESI (Dark Energy Spectroscopic Instrument) Legacy Imaging Survey; HSC, Hyper Suprime-Cam; NIR, near-infrared; PS1, Panoramic Survey Telescope & Rapid Response System 1; SDSS, Sloan Digital Sky Survey.

of large-scale optical and NIR sky surveys, improvements in selection and contaminant rejection, and efficient spectroscopic identification.

Quasar candidates are separated from other point sources in photometric surveys because of their distinct spectral energy distributions (SEDs). The intrinsic spectra of quasars in the rest-frame UV and optical bands are characterized by a blue power-law continuum and a number of strong broad emission lines. At  $z > 3$ , the strong IGM neutral hydrogen (H $\text{I}$ ) absorption from Lyman series lines and the Lyman continuum redshifts into the observed optical wavelength. Thus, high-redshift quasars are “dropout” objects with a strong Lyman break, and the dropout bands correspond to the observed wavelength of the Lyman break. At longer wavelength, quasars have blue broadband colors due to their power-law continuum. The Lyman dropout selection method for quasars has been used since the discoveries of the first  $z > 4$  quasars (Warren et al. 1987). A more recent development is the inclusion of mid-IR (MIR) photometric surveys in the candidate selection (e.g., Wu et al. 2015). The long-wavelength baseline from NIR to MIR, in particular using the *Wide-Field Infrared Survey Explorer* (WISE; Wright et al. 2010) data, allows more effective separation of high-redshift quasars and MLT dwarfs by colors.

**Figure 2** illustrates how to use the combination of optical and IR colors to select  $z > 6.5$  quasars. At  $z \sim 6.5$ , the strong Lyman- $\alpha$  (Ly $\alpha$ ) emission line is in the  $y$  band. At higher redshift, this band starts to be dominated by IGM absorption, and quasars become “ $y$ -dropouts” with increasing red  $y$ - $J$  colors. Meanwhile, the  $J$ - $W1$  color is determined by the quasar power-law continuum and has a near constant value, which is redder than most of the sub/stellar objects with spectral types earlier than L. The main contaminants for this redshift range are L and T dwarfs.

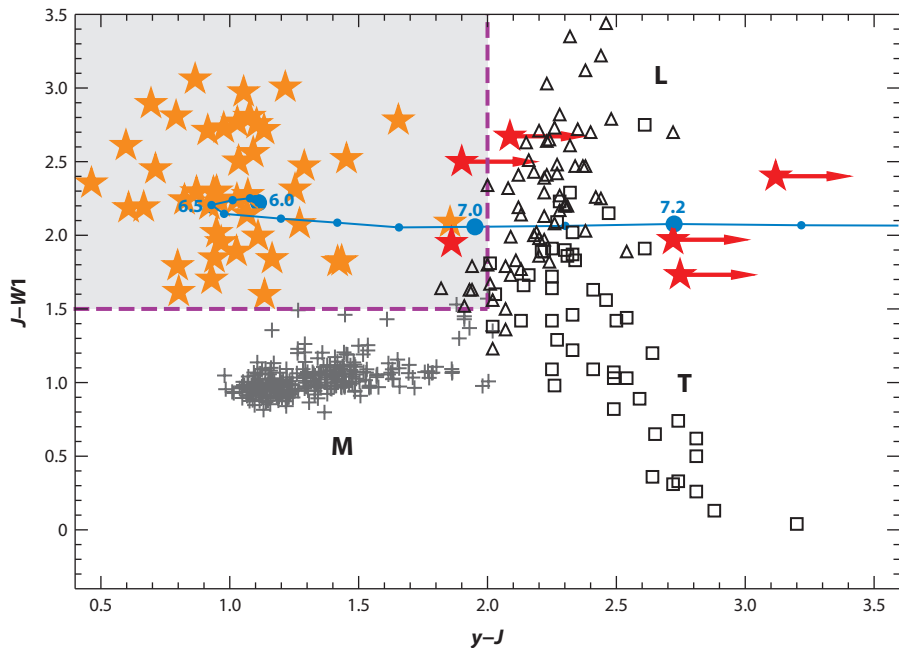


**Figure 2**

Example of  $y$ - $J$  versus  $J$ - $W1$  color-color diagram used for high-redshift quasar selections. The cyan line represents the average color-redshift relation for quasars at  $z = 6$ - $7.3$  based on simulated quasar spectra. Orange stars are known quasars at  $6.5 < z < 7.0$ ; magenta lines show the selection criteria used by Wang et al. (2019) for this redshift range. Red stars are known quasars at  $z > 7.0$ ; black symbols are known MLT contaminants. Figure adapted from Wang et al. (2019).

**Table 1** Quasars at  $z > 7$ 

| Quasar               | $z$    | $M_{1450}$ mag | $M_{\text{BH}} 10^8 M_{\odot}$ | Discovery reference   | $M_{\text{BH}}$ reference |
|----------------------|--------|----------------|--------------------------------|-----------------------|---------------------------|
| J031343.84–180636.40 | 7.6423 | −26.13         | 16.1                           | Wang et al. 2021b     | Yang et al. 2021          |
| J134208.11+092838.61 | 7.54   | −26.71         | 8.1                            | Bañados et al. 2018   | Yang et al. 2021          |
| J100758.27+211529.21 | 7.5149 | −26.62         | 14.3                           | Yang et al. 2020b     | Yang et al. 2021          |
| J112001.48+064124.30 | 7.0848 | −26.58         | 13.5                           | Mortlock et al. 2011  | Yang et al. 2021          |
| J124353.93+010038.50 | 7.0749 | −24.13         | 3.6                            | Matsuoka et al. 2019b | Matsuoka et al. 2019b     |
| J003836.10–152723.60 | 7.034  | −27.01         | 13.6                           | Wang et al. 2018      | Yang et al. 2021          |
| J235646.33+001747.30 | 7.01   | −25.31         | ND                             | Matsuoka et al. 2019a | ND                        |
| J025216.64–050331.80 | 7.0006 | −25.77         | 12.8                           | Yang et al. 2019b     | Yang et al. 2021          |

Abbreviation: ND, no data.

Inayoshi et al. (2020) presented a summary table of the photometric surveys used in the discoveries of  $z > 6$  quasars in the past 15 years. Early surveys such as SDSS and Panoramic Survey Telescope & Rapid Response System 1 (PS1; Chambers et al. 2016) used 2–4-m-class telescopes with relatively short exposure times; thus they are optimized to discover rare, luminous quasars in large sky areas. Selection of fainter quasars requires photometric observations on large-aperture telescopes: The Subaru High- $z$  Exploration of Low-Luminosity Quasars (SHELLQs) project (Matsuoka et al. 2022) is based on the Hyper Suprime-Cam (HSC) survey on the 8.2-m Subaru Telescope (Aihara et al. 2018). As shown in **Figure 2**, at  $z > 7$ , quasars begin to drop out in the  $y$  band at the red limit of CCD (charge-coupled device) detector sensitivities. The discovery of quasars at this redshift requires the combination of wide-field IR surveys, which provide detection of the quasar rest-frame UV continuum, and deep optical surveys, which sample the strong Lyman break. Following the first quasar discovery at  $z > 7$  using photometric data from the UKIDSS survey (Mortlock et al. 2011), there have been eight quasars published at  $z > 7$  (see **Table 1**). The current redshift frontier is represented by the three luminous quasars known at  $z > 7.5$ , selected using a combination of NIR, optical, and MIR (WISE) surveys: J1342+0928 at  $z = 7.54$  (Bañados et al. 2018); J1007+2115 at  $z = 7.52$  (“Pōniuō’ena”; Yang et al. 2020b); and J0313–1806 at  $z = 7.64$  (Wang et al. 2021b).

## 2.2. Optimization of Photometric Selection of High-Redshift Quasars

The vast majority of high-redshift quasars have been discovered using color selection. The most commonly used method is to implement a series of “color cuts”: select objects that meet a set of criteria in the flux/flux-error space (usually referred to as the color space) as high-redshift quasar candidates. These cuts are often initially guided by a combination of photometry of existing high-redshift quasars and simulated colors based on synthetic quasar spectra, as well as observed and simulated data of the contaminant populations. These cuts are refined as surveys progress with larger training sets and better understanding of the contaminant populations. Fan (1999) presented an early example of color space simulation of different populations of objects with compact morphology (quasars, normal stars, white dwarfs, and compact galaxies) in the SDSS photometric system. This simulation was used to formulate color selections for both the SDSS main spectroscopic survey (Richards et al. 2002) and selections of  $z \sim 6$  quasars (Fan et al. 2001). Works such as those by Hewett et al. (2006), McGreer et al. (2013), Barnett et al. (2019), and Temple et al. (2021) expanded these simulations by including more realistic quasar population models and models of MLT and intermediate-redshift galaxies, extending to higher redshifts, and including NIR and MIR photometric bands.

High-redshift surveys based on SDSS (e.g., Jiang et al. 2016) and PS1 (e.g., Bañados et al. 2016), as well as works using the DESI (Dark Energy Spectroscopic Instrument) Legacy Survey

(e.g., Wang et al. 2019), used color cuts as their primary selection method. The color cut method is simple to implement and has high selection completeness even for objects that have unusual spectral features such as broad absorption lines (BALs), weak emission lines, or those with modest reddening, because the color cuts are usually fairly loose and cover a large portion of color space, and the strong Lyman break is not strongly affected by the intrinsic quasar SEDs. By contrast, because all candidates that satisfy the cuts are selected without considering the relative density distribution of the targeted (quasar) population and the contaminant populations (primary MLTs and compact galaxies), or how the candidate SEDs match the quasar template, color cut selection tends to have a higher contamination rate. For example, Wang et al. (2019) find a 30% spectroscopic success rate when searching for  $z > 6.5$  quasars. The contamination grows significantly worse for  $z \sim 7.5$  (F. Wang, private communication).

A number of techniques have been applied to improve the efficiency of color selection. These improvements are especially important for quasars at the highest redshifts ( $z > 6.5$ ), where quasars are increasingly rare compared to the contaminant populations, and at fainter fluxes for which increasing photometric errors result in more contaminants scattering into the selected area in color space. Mortlock et al. (2012) first introduced a selection algorithm based on Bayesian model comparison (BMC). In BMC, the posterior quasar probability for a given object with survey photometry  $\mathbf{d}$  is given by

$$P_q = p(q|\mathbf{d}) = \frac{W_q(\mathbf{d})}{W_q(\mathbf{d}) + W_b(\mathbf{d}) + W_g(\mathbf{d})}, \quad 1.$$

where q, b, and g represent quasar, brown dwarf (MLTs), and galaxy populations, respectively. The weights  $W$  for each population are calculated using a population model that describes its surface density distribution integrated over a Gaussian likelihood function based on model colors. BMC was applied by Mortlock et al. (2011) to data from the UKIDSS survey to identify the first quasar at  $z > 7$ . The SHELLQs survey (Matsuoka et al. 2022) used BMC to select faint quasars in the HSC survey with great success in achieving a high spectroscopic identification rate ( $\sim 75\%$ ) even at the low-luminosity end at  $z \sim 6$ . Wagenveld et al. (2022) presented a similar probabilistic approach that also includes radio data in the selection.

Reed et al. (2017) applied an SED fitting method for high-redshift quasar selection. In this method, after the initial color cuts, reduced  $\chi^2$  values are calculated for each candidate, matching the observed colors of the candidate observed SEDs to a series of model SEDs, including different MLT spectral types as well as early-type galaxies at various redshifts. Objects with high reduced  $\chi^2$  for the contaminant populations and low values for the quasar SED models are selected as quasar candidates.

Barnett et al. (2021) presented a detailed comparison study of different selection techniques in searching for  $z > 6.5$  quasars using VIKING [VISTA (Visible and Infrared Survey Telescope for Astronomy) Kilo-degree Infrared Galaxy Survey] data. They show that BMC is highly complete in recovering previously known quasars in the survey area, and at the same time this method effectively rejects confirmed contaminants. Using simulations, they calculate the survey selection function—completeness as a function of quasar redshift and luminosity and find that both BMC and the SED methods represent a significant improvement in selection completeness and depth compared to simple color cuts.

Wenzl et al. (2021) used a random forest supervised machine learning method to select  $z > 5$  quasars from PS1 data with high efficiency. Nanni et al. (2022) proposed an alternative probabilistic approach, in which the density of the contaminant populations in color space is modeled as Gaussian mixtures based on observed photometric data and calculated using the extreme deconvolution technique instead of using simulated population models.

High-redshift quasar selection can also be considered in the context of supervised machine learning. The training sets of existing objects are small, and in most cases are subject to the bias of previously selected samples or extrapolations from low-redshift populations. The choice of high-redshift quasar selection algorithm in a given survey is a trade-off between completeness and efficiency. Selections that rely on SED and contaminant population models run the risk of missing objects that are highly valuable but have unusual properties. An example is the discovery of J0100+2802, the most luminous unlensed quasar currently known at  $z > 5$  (Wu et al. 2015). The object was assigned as low priority in the original SDSS survey due to its relatively red color and bright apparent magnitude, indicating a high probability of it being a brown dwarf. It is not surprising that a record-breaking discovery is made often—but not always (e.g., Mortlock et al. 2011)—using the less restrictive color cut method, and probabilistic methods are more effective once a large training set has been established.

If high-redshift quasar candidates could be part of the overall target selection in a large automated spectroscopic survey program, then the color selection could be relaxed to be more complete and less sensitive to templates or model assumptions, because high-redshift quasar candidates are rare and are thus only a small fraction of the total targets. The SDSS main quasar survey (Richards et al. 2002) targeted quasars up to  $z \sim 5.4$ . The DESI (DESI Collab. 2022) is using spectrographs with 5,000 fibers on the 4-m Mayall Telescope at Kitt Peak to conduct a five-year spectroscopic survey of  $\sim 40$  million galaxies, quasars, and stars. DESI is expected to more than double the number of quasars known at  $z > 5$  when completed. A similar survey is being planned for the 4MOST (4-metre Multi-Object Spectroscopic Telescope) project (Merloni 2019).

Other established quasar selection methods include variability, astrometry (i.e., lack of proper motion; Lang et al. 2009), detections in X-ray and radio wavelengths, and MIR colors, as well as wide-field slitless spectroscopy. Except for the last method (e.g., Schneider et al. 1989, 1999), most selection methods are not sensitive to the quasar redshifts. Therefore, some color cuts are usually used to identify high-redshift quasar candidates. McGreer et al. (2006) and Zeimann et al. (2011) report the first discoveries of radio-loud  $z > 6$  quasars by matching radio surveys such as FIRST (Faint Images of the Radio Sky at Twenty centimeters) with optical photometric surveys. X-ray observations provide fundamental probes of AGN evolution across cosmic time. New wide-field X-ray surveys such as eROSITA (extended Roentgen Survey with an Imaging Telescope Array; Wolf et al. 2021) will enable selections of luminous X-ray quasars at the highest redshifts. We discuss the X-ray and radio properties of high-redshift quasars in Section 3.2.

### 2.3. A Database of $z > 5.3$ Quasars

At the time of this review, there are 532  $z \geq 5.3$  quasars in the published literature. We present their spectra in **Figure 3**. The locations of the  $z \geq 5.3$  quasars on the redshift–luminosity plane is shown in **Figure 1**. We include a database with their basic properties in the **Supplemental Database** associated with this review. To be included in this database, we require the object to meet the following criteria: (a) have a spectroscopically confirmed redshift  $z \geq 5.3$ —we do not include objects with only photometric redshifts; (b) have at least one broad emission line ( $FWHM > 2,000 \text{ km s}^{-1}$ ) in the rest-frame UV—we do not include narrow-line (type-2) quasars or obscured AGNs at high redshift. In addition to the quasar name, coordinates, redshift, and references, the database also includes measurements of the quasar’s continuum luminosity at the rest-frame 1450 Å and 3000 Å, properties of the MgII emission line, and BH mass derived from MgII measurements quoted in the literature, estimated using Equation 4. We only consider MgII measurements for quasars at  $z > 5.9$ , as MgII lines are usually in regions highly affected by telluric absorption in the NIR at lower redshift.

**Supplemental Material** >

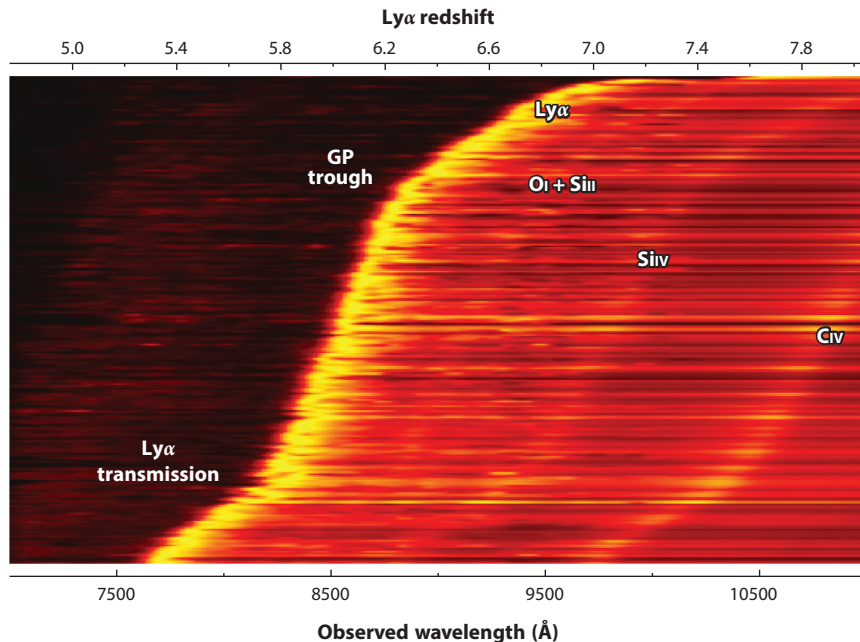


**Figure 3**

Two-dimensional image representation of 527/532 of all published spectra of  $z \geq 5.3$  quasars. Traces of major emission lines are labeled. On the blue side of the  $\text{Ly}\alpha$  line, there are clear signatures of the  $\text{Ly}\alpha$  transmission at  $z < 6$ , whereas at higher redshift, the spectra are dominated by long GP absorption troughs. Abbreviation: GP, Gunn–Peterson.

The high-redshift quasar database includes 275 objects at  $z > 6$  and 8 at  $z > 7$ . At the time of writing, there are 113  $z > 5.9$  quasars with robust  $\text{MgII}$ -based BH mass estimates. We list the properties of quasars currently known at  $z > 7$  in **Table 1**. This database expands the compilation in the supplemental material of Inayoshi et al. (2020). The quasar luminosities lie between  $M_{1450} = -20.9$  and  $-29.4$ ; the median luminosity of these objects is  $M_{1450} = -25.8$ . The brightest object is J0439+1634, a gravitationally lensed quasar at  $z = 6.5$  (Fan et al. 2019b). **Figure 3** shows a two-dimensional image representation of all spectra of the quasars in the database. In this image, each row is the one-dimensional spectrum of a quasar, ordered in ascending redshift. The flux level of each column is normalized by its peak  $\text{Ly}\alpha$  flux. The image shows how the quasar  $\text{Ly}\alpha$  emission lines move to NIR wavelengths as the redshift increases from  $z \sim 5$  to  $> 7$ . On the blue side of the  $\text{Ly}\alpha$  emission, the spectra show the extent of the highly ionized quasar proximity zone (Section 6.3.1), where the flux does not immediately drop to zero. Further blueward, the spectrum is dominated by strong Gunn–Peterson absorption. Complete Gunn–Peterson absorption troughs can be seen at  $z > 6$ . At lower redshift, the presence of transmission spikes indicates that the IGM is, on average, highly ionized (Section 6). On the red side of  $\text{Ly}\alpha$  emission, broad emission lines such as  $\text{OI} + \text{SiII} \lambda 1306$ ,  $\text{SiIV} + \text{OIV} \lambda 1402$ , and  $\text{CIV} \lambda 1549$  are visible.

## 2.4. Future Quasar Surveys

New surveys are on the horizon to further expand the quasar redshift frontier. The Legacy Survey of Space and Time (LSST) by the Vera C. Rubin Observatory will cover the southern sky at optical wavelengths to unprecedented depths. LSST will reach  $5\sigma$  coadded depths in the  $z$  and  $y$  bands at

25–26-mag level in 5–10 years (Ivezić et al. 2019), allowing selections of several thousand quasars and AGNs at  $z \sim 6$ –7.5 using both color and variability selection methods while providing deep photometry in the dropout bands for selection of  $z > 7$  quasars. The European Space Agency’s *Euclid* mission will provide deep NIR photometry not possible with ground-based observations. It will cover 15,000 deg<sup>2</sup> of the sky to a  $5\sigma$  depth of 24 mag in the *Y*, *J*, and *H* bands (Scaramella et al. 2022), enabling selection of quasar candidates up to  $z \sim 10$ . Barnett et al. (2019) predicted that *Euclid* together with LSST will allow discoveries of  $\sim 25$  quasars at  $z > 7.5$ , including  $\sim 8$  beyond  $z > 8$ , although the exact yields strongly depend on the assumed evolution of the QLF. Further in the future is NASA’s *Nancy Grace Roman Space Telescope*, which will cover a smaller area in its High Latitude Survey but reach  $\sim 2$  mag deeper.

Fan et al. (2019a) show that by extrapolating the current measurement of the QLF, there will be only one SDSS-like quasar ( $M_{1450} < -26$ , powered by a billion-solar-mass SMBH) over the entire observable Universe at  $z > 9$ . The combination of LSST, *Euclid*, and *Roman Space Telescope* will allow the discovery of the earliest luminous quasars in the Universe. However, in addition to the challenges of their selection (Barnett et al. 2019, Nanni et al. 2022), their spectroscopic identification will require IR spectrographs more powerful than those with the current ground-based telescopes: 30-m-class extremely large telescopes and JWST will be the primary tools for their confirmation and follow-up observations.

### 3. AN EVOLVING QUASAR POPULATION

In this section, we first review the evolution of the QLF at high redshift, which directly constrains the growth history of early SMBHs (Section 3.1). The number density of quasars is found to decline rapidly toward high redshift, in sharp contrast to the lack of strong evolution in the SEDs of quasars (Section 3.2), from X-ray to radio, and in particular in the rest-frame UV to NIR, at which the quasar SED peaks, although a number of subtypes of quasars appear to be more common at  $z > 5$ –6.

#### 3.1. Evolution of the Quasar Luminosity Function

Soon after the initial discovery of quasars, Schmidt (1968) found that their density rises sharply with redshift up to  $z \gtrsim 2$ . Wide-field surveys such as 2dF (Two-degree Field Galaxy Redshift Survey; Boyle et al. 2000) and SDSS (Richards et al. 2006b) established that the density of luminous quasars peaks at  $z \sim 2$ –3. Osmer (1982) presented the first evidence that quasar density at  $z > 3.5$  appears to be declining. Schmidt et al. (1995) characterized this decline as an exponential function with redshift:

$$\rho(z) \propto 10^{kz}, \quad 2.$$

where  $k$  is measured to be  $\sim -0.5$  at  $z \sim 3$ –5. The shape of the QLF is usually described as a double, or broken, power law:

$$\Phi(M_{1450}, z) = \frac{\Phi^*(z)}{10^{0.4(\alpha+1)(M_{1450}-M_{1450}^*)} + 10^{0.4(\beta+1)(M_{1450}-M_{1450}^*)}}, \quad 3.$$

where  $M_{1450}$  is the absolute magnitude of the quasar continuum at rest-frame 1450 Å;  $\alpha$  and  $\beta$  are the faint-end and bright-end slopes, respectively;  $M_{1450}^*$  is the characteristic absolute magnitude or break magnitude measured at 1450 Å; and  $\Phi^*$  is the normalization of the QLF which has an exponential decline described in Equation 2.

Early high-redshift surveys such as the SDSS were only sensitive to the most luminous quasars. Based on a sample of nine SDSS quasars at  $z > 5.7$ , Fan et al. (2004) found that at  $z \sim 6$ , the comoving spatial density of quasars with  $M_{1450} < -26.7$  is  $6 \times 10^{-10}$  Mpc<sup>-3</sup>, which is consistent with

extrapolation from lower-redshift trends. Jiang et al. (2009) extended the SDSS quasar survey to the Stripe 82 region, reaching 2 mag deeper than the SDSS main survey. They found a bright-end slope  $\beta$  between  $-2.6$  and  $-3.1$ . Willott et al. (2010) combined the faint quasars discovered in the Canada-France High- $z$  Quasar Survey (CFHQS) with the brighter SDSS quasars and presented the first measurement of QLF at  $z \sim 6$  using a sample of 40 quasars. They found a bright-end slope of  $\beta = -2.81$  and a break magnitude of  $M_{1450}^* = -25.1$ ; the faint-end slope was still poorly constrained at this redshift. Jiang et al. (2016) presented the final results of the  $z \sim 6$  quasar survey in the SDSS footprint. Using this sample of 52 quasars at  $5.7 < z < 6.4$ , they found a bright-end slope of  $\beta = -2.8 \pm 0.2$ . In addition, they found a density evolution with the exponential evolution parameter  $k = -0.72 \pm 0.11$ , which is a significantly steeper slope than the value at  $z \sim 3-5$ , suggesting an accelerated evolution of luminous quasars between  $z \sim 5$  and 6.

The SHELLQs project (Matsuoka et al. 2016) extended the  $z \sim 6$  quasar sample to significantly lower luminosity. Matsuoka et al. (2018) presented measurements of the QLF down to  $M_{1450} \sim -22$ , which is well fit with a double power law that has a faint-end slope of  $\alpha = -1.23_{-0.34}^{+0.44}$ , a bright-end slope of  $\beta = -2.73_{-0.31}^{+0.23}$ , and a break magnitude of  $M_{1450}^* = -24.90_{-0.90}^{+0.75}$ . Their measured QLF showed a strong break and a significant flattening at the faint end at  $z \sim 6$ . Schindler et al. (2023) used the combination of the bright PS1 quasar sample that includes 125 quasars at  $z \sim 5.7-6.2$  with the fainter quasars from SHELLQs for a new QLF measurement at  $z \sim 6$ . They found a steeper bright-end slope of  $\beta = -3.84_{-1.21}^{+0.63}$ , as well as a steeper faint-end slope of  $\alpha = -1.70_{-0.19}^{+0.29}$ , with a bright break magnitude of  $M_{1450}^* = -26.38_{-0.60}^{+0.79}$ . Their study yields a constant redshift evolution of  $k \sim -0.7$  over a wide redshift range of  $z = 4-7$ .

Measurement of the QLF becomes increasingly difficult at higher redshift due to the rapid decline in spatial density of quasars. Wang et al. (2019) conducted the first measurement of the QLF at redshift approaching 7 based on a sample of 17 quasars at  $6.45 < z < 7.05$  (see also Venemans et al. 2013). They found a quasar spatial comoving density of  $\rho(M_{1450} < -26) = 0.39 \pm 0.11 \text{ Gpc}^{-3}$  at  $z \sim 6.7$  and an exponential density evolution parameter of  $k = -0.78 \pm 0.18$ . The density of luminous quasars declines by a factor of  $\sim 6$  per unit redshift. The  $e$ -folding time of quasar density evolution and that of BH accretion (Section 4) become comparable, underlying the strong constraints quasar evolution could place on the SMBH accretion mode.

**Figure 4b** illustrates the overall density evolution of luminous ( $M_{1450} < -26$ ) quasars with measurements from various surveys at  $z = 3-7$ . Although a strong exponential decline in the comoving spatial density of luminous quasars has been well established, there are still significant uncertainties in the evolution of the shape of the QLF (**Figure 4a**). As discussed by Schindler et al. (2023), the bright-end slope determination is strongly influenced by small-number statistics. At the faint end, selection incompleteness could be a significant factor when a completeness correction of  $\gtrsim 2$  is often needed.

There have been a number of ambitious efforts to combine QLF measurements across the electromagnetic spectrum and different cosmic epochs to obtain a complete picture of quasar/AGN evolution from reionization to the current epoch. Hopkins et al. (2007) presented the bolometric QLF up to  $z \sim 6$ . They explicitly modeled the X-ray column density distribution and SED shape variation of quasars to allow determinations of bolometric luminosities of high-redshift populations. Kulkarni et al. (2019b) constructed a sample of more than 80,000 color-selected quasars and AGNs with a homogeneous treatment of survey selection effects, and derived the AGN UV LF from  $z = 0$  to 7.5. Their measurement suggested a continued steepening of the faint-end slope  $\beta$  and a brightening of the break magnitude. Shen et al. (2020) updated the early Hopkins et al. work. They found bolometric QLF evolution consistent with those based on UV-selected samples alone and concluded that the faint-end slope measurement is still uncertain at high redshift.

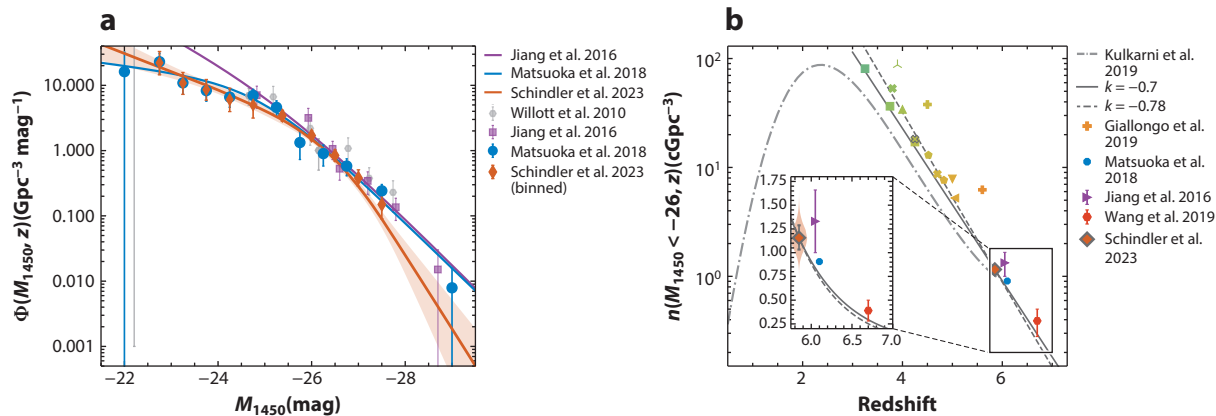


**Figure 4**

QLF measurements at high-redshift. (a) The QLF at  $z \sim 6$  from SDSS, CFHTQS, SHELLQs, and PS1 surveys and best-fit double power-law results. (b) The density of luminous ( $M_{1450} < -26$ ) quasars as a function of redshift (for measurements at  $z < 5.3$ , see references in Schindler et al. 2023). Panels adapted from Schindler et al. (2023). Abbreviations: CFHQs, Canada–France High- $z$  Quasar Survey; PS1, Panoramic Survey Telescope & Rapid Response System 1; QLF, quasar luminosity function; SDSS, Sloan Digital Sky Survey; SHELLQs, Subaru High- $z$  Exploration of Low-Luminosity Quasars.

For the purpose of comparison with theoretical models or making predictions of future surveys, we suggest using the combined QLF measurements presented by Kulkarni et al. (2019b) or Shen et al. (2020) for  $z \lesssim 6$ , where the QLF is well measured over a wide range of luminosities. At  $z \gtrsim 6$ , the uncertainty is still large for both the QLF shape and its redshift evolution; Schindler et al. (2023) presented the most up-to-date measurements.

A key limitation of current high-redshift quasar surveys is that the quasar selection methods assume a blue power-law continuum in the rest-frame UV. It is possible that current surveys are missing a significant number of red or reddened quasars. Kato et al. (2020) reported the discovery of two dust-reddened quasars at  $z > 5.6$  in the SHELLQs survey based on their MIR WISE detection. Endsley et al. (2022) discovered an obscured radio-loud AGN at  $z = 6.85$  in the 1.5-deg<sup>2</sup> COSMOS field with bolometric luminosity comparable with that of luminous SDSS  $z \sim 6$  quasars. Ni et al. (2020) studied the obscuration of high-redshift quasars using the BlueTides simulation and predicted that the dust-extincted UV LF is about 1.5 dex lower than the intrinsic LF, and the vast majority of  $z \sim 7$  AGNs have been missed by UV-based surveys due to dust extinction. This would imply a much higher bolometric luminosity density of early quasars and would have a profound impact on the growth of SMBHs and early galaxy evolution overall. A reliable determination of the obscured fraction of quasars at  $z \gtrsim 5$  needs a combination of wide-field deep X-ray survey and effective spectroscopic identification of faint, obscured sources with either JWST or NOEMA (Northern Extended Millimeter Array)/ALMA.

### 3.2. (A Lack of) Evolution of the Quasar Spectral Energy Distributions

High-redshift galaxies have intrinsic blue SEDs that are dominated by young stellar populations. Metallicity, or chemical abundance, in their ISM has also been shown to be lower than in low-redshift galaxies (Stark 2016). However, the overall SEDs and the chemical abundance in quasar broad-line regions (BLRs) do not evolve significantly with redshift, although quasar density decreases drastically at high redshift. This apparent lack of spectral evolution in the UV properties of quasars was noticed as soon as the first  $z \sim 6$  quasars were discovered (e.g., Barth et al. 2003,

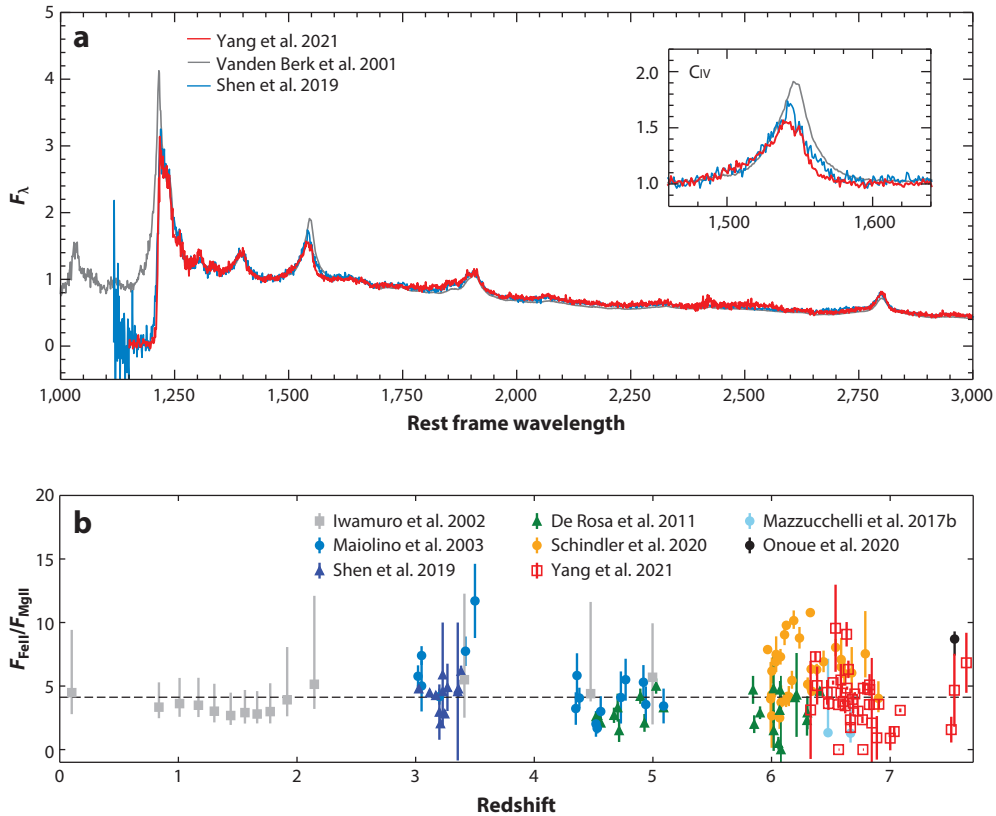


**Figure 5**

(a) Quasar composite spectrum (*red solid line*) from Yang et al. (2021) compared with the low-redshift ( $z \lesssim 3$ ) composite from Vanden Berk et al. (2001) (*gray line*) and the  $z \sim 6$  quasar composite from Shen et al. (2019) (*blue line*). The average intrinsic spectrum of quasars does not exhibit significant redshift evolution. (b) The evolution of the Fe/ Mg emission line ratio in quasars as a function of redshift. The quasar broad-line region is highly enriched even at the highest redshift. Figure adapted from Yang et al. (2021).

Fan et al. 2004, Iwamuro et al. 2004, Jiang et al. 2007). Shen et al. (2019) conducted an optical/NIR spectroscopic survey of 50 quasars at  $z > 5.7$ . Their observations covered the wavelength range from the Ly $\alpha$  to Mg II emission lines. Yang et al. (2021) presented a spectroscopic survey of 34 quasars at  $6.3 < z < 7.6$ , covering a similar wavelength range. Both papers presented composite rest-frame UV spectra of their high-redshift samples. **Figure 5** compares the quasar composite spectra at  $z \sim 6-7$  with the standard low-redshift SDSS quasar composite from Vanden Berk et al. (2001). The average continuum slope and emission line strength/width do not evolve significantly with redshift, with the exception of a weaker and blueshifted C IV emission line (see discussion in Section 5.4).

Broad emission line ratios in quasars have been used to constrain metallicities in the quasar BLR. Jiang et al. (2007) and De Rosa et al. (2014) studied emission line ratios in a series of UV lines and found no evidence of evolution from lower-redshift samples, with the gas metallicity being a few times solar based on photoionization modeling. This is confirmed by studies using high signal-to-noise (S/N) spectroscopy from the XQR30 survey (<https://xqr30.inaf.it/>) of quasars at  $z = 5.8-7.5$  (Lai et al. 2022). The line ratio of Fe II/Mg II is of particular interest because of the different enrichment histories of these two lines: Mg is an  $\alpha$  element predominantly

produced by core-collapse supernovae, whereas Fe is mainly from type-1a supernovae with an evolutionary lifetime delay of a few hundred million years to 1 Gyr. The evolution of the Fe/Mg ratio in quasars has been studied extensively (e.g., Barth et al. 2003, Iwamuro et al. 2004, De Rosa et al. 2014, Mazzucchelli et al. 2017b, Shen et al. 2019, Yang et al. 2021). Schindler et al. (2020) carried out detailed modeling of FeII and MgII lines using a large sample of quasar spectra from XSHOOTER on the Very Large Telescope (VLT) and compared their measurements with those in the literature. There is no evidence of evolution in the Fe/Mg ratio up to the highest redshift, although scatter is large at any given redshift (**Figure 5**). The lack of spectral evolution in quasar rest-frame UV spectra, especially in the emission line properties, indicates that quasar BLRs are chemically enriched very rapidly, within the first few hundred million years after the initial star formation in the host galaxy. This is not surprising, as we examine in Section 5: Quasar host galaxies are sites of the most intense star formation in the early Universe.

However, there are a few noticeable evolutionary trends in quasars at cosmic dawn that could be related to the early phase of quasar growth. In Section 5.4, we discuss an increasing fraction of quasars with strongly blue-shifted high-ionization UV emission lines and with strong BAL features as evidence for early quasar feedback. In Section 6.3.1, we present the discovery of  $z \sim 6$  quasars with IGM absorption features indicative of very young ages.

A subset of high-redshift SDSS quasars have much weaker UV emission lines, in particular Ly $\alpha$  and CIV. Diamond-Stanic et al. (2009) identified them as  $>3\sigma$  outliers in the quasar emission line strength distributions. They represent  $\sim 1\%$  of quasar population at  $z < 4$ , after correction for selection incompleteness (Diamond-Stanic et al. 2009). Bañados et al. (2016) showed that this fraction increases to  $\sim 14\%$  among  $z > 5.6$  PS1 quasars based on Ly $\alpha$  measurements. Shen et al. (2019) found a similar fraction using CIV measurements. It remains unclear whether weak line quasars are related to the young age or high accretion rate in the high-redshift quasar population (Plotkin et al. 2015).

X-ray emission originates from the accretion disk and surrounding hot corona close to the central SMBH and provides crucial information about BH accretion and AGN feedback (Fabian 2012). Brandt et al. (2001) detected the first  $z \sim 6$  quasar in X-rays using the XMM-Newton (*X-ray Multi-Mirror Mission-Newton*) telescope. More than 30 quasars at  $z \gtrsim 6$  have now been detected in X-rays, using either the *Chandra X-ray Observatory* or XMM-Newton telescopes. Nanni et al. (2017) analyzed 29 quasars at  $z > 5.5$  with X-ray detections. They found a mean X-ray power-law photon index of  $\Gamma \sim 1.9$ , which is similar to that at low redshift. The optical–X-ray spectral slopes of the high redshift also follow the relation established at low redshift. Vito et al. (2019b) carried out a similar analysis and found a slightly steeper X-ray power-law index, consistent with a generally higher Eddington ratio among SMBHs in these quasars at  $z > 6$ . Wang et al. (2021a) extended the X-ray analysis to quasars at  $z \sim 7$  (see also Pons et al. 2020). They also found a steepening of X-ray spectra with  $\Gamma \sim 2.3$ . The optical–X-ray power-law slope,  $\alpha_{OX}$ , traces the relative importance of the accretion disk and corona emission in quasars and AGNs. At low redshift, there is a tight correlation between  $\alpha_{OX}$  and the quasar UV luminosity (e.g., Just et al. 2007). There is no evolution in this correlation up to  $z \sim 7$  (e.g., Wang et al. 2021a). The X-ray observations show a consistent picture that the inner accretion-disk and hot-corona structure in quasars was established at the highest redshift with minimal evolution in their properties across cosmic time.

At rest-frame NIR and MIR wavelengths, the radiation from quasars is dominated by reprocessed emission from the hot dust component beyond the accretion disk structure (see review by Lyu & Rieke 2022). At the highest redshift, dust observations (at rest frame  $>1.5 \mu\text{m}$ ) have been largely limited to photometric observations of bright sources using the *Spitzer Space Telescope* (e.g., Jiang et al. 2006) and *Herschel Space Observatory* (Leipski et al. 2014), although this will change with the launch of JWST. These observations also showed a lack of evolution: The average IR-SEDs of

quasars at  $z \sim 5\text{--}6$  are consistent with low-redshift templates, and the hot dust structure is already in place by  $z \sim 6$ . Jiang et al. (2010) reported the detection of two quasars at  $z \sim 6$  with weak hot dust emissions using *Spitzer*. Later studies suggested that these dust-deficient quasars are not unique to  $z > 6$ , and examples with similar SEDs are found even in the low-redshift Paloma–Green sample (e.g., Lyu et al. 2017).

Quasars were initially discovered as point-like sources emitting strong radio emissions (Schmidt 1963). However, the fraction of quasars that exhibit strong jet-powered radio emission (radio-loud quasars) is around 10% with no significant dependence on redshift, at least up to  $z \sim 6$  (Bañados et al. 2015, Gloude-mans et al. 2021, Liu et al. 2021). The highest-redshift radio-loud quasar known is at  $z = 6.82$  (Bañados et al. 2021), and the highest-redshift blazar is at  $z = 6.10$  (Belladitta et al. 2020). It is still debated whether the seemingly constant radio-loud fraction is due to two intrinsically different populations of quasars or is a consequence of the duty cycle of jet emission during the life of a quasar. If the latter were the case, one should expect an increase in the radio-loud fraction at the highest redshifts (where the available time for a quasar shortens), something we have not yet witnessed and that depends on the lifetime of the radio-loud phase.

The lack of evolution in the radio-loud fraction discussed above concerns the compact core radio emission. However, there is an important evolution with redshift if we focus on the extended radio emission: the lack of giant (on the order of hundreds of kiloparsecs) radio lobes at  $z > 4$ , which are common at lower redshifts (Fabian et al. 2014). Indeed, the most extended radio jet known at  $z \sim 6$  is  $< 2$  kpc (Momjian et al. 2018). A plausible physical explanation is that at  $z > 4$ , the CMB energy density [ $\propto (1+z)^4$ ] exceeds the magnetic energy density in radio lobes. In that case, inverse Compton (IC) scattering losses make any large lobes at high redshift radio weak and X-ray bright (Ghisellini et al. 2014). The IC/CMB effect has been challenging to probe with current X-ray telescopes. Recent deep *Chandra* observations of the two  $z \sim 6$  quasars with the most extended radio jets resulted in tentative evidence of larger X-ray jets (Connor et al. 2021, Ighina et al. 2022). Obtaining this marginal evidence was expensive, even for our most powerful X-ray telescopes observing the best existing targets to test this effect. To robustly measure the IC/CMB effect in a sample of radio-loud quasars, we will likely need to wait for the next generation of X-ray telescopes.

The discussions in this subsection present a picture that on average, the intrinsic SEDs of quasars at the highest redshift, with emission from the accretion disk (X-ray, UV/optical), broad emission line regions, hot dust, and radio jets, show little evolution from their low-redshift counterparts. The AGN structure is already in place and fully formed up to the highest redshift we have observed to date.

JWST will enable detailed studies of the physical properties of high-redshift quasars in the rest-frame optical and IR wavelengths that are not possible from the ground. It will be especially interesting to see if the dust component of the quasar population shows any evolution, because the dust production mechanism (e.g., Maiolino et al. 2004) and the ISM conditions in the host galaxies are likely different in early epochs. X-ray observations with *Chandra* and XMM-Newton of even the most luminous quasars at cosmic dawn can only yield a small number of photons. Future X-ray missions (e.g., Martocchia et al. 2017) could allow high S/N spectroscopic observations of early quasars to characterize their accretion properties (including BH spin) and X-ray obscuration.

#### 4. GROWTH OF SUPERMASSIVE BLACK HOLES IN THE FIRST BILLION YEARS

SMBHs are thought to be ubiquitous in the centers of massive galaxies, but their formation mechanism is still an outstanding question in astrophysics. Since the discovery of quasars at  $z \gtrsim 6$  (Fan et al. 2001), the formation and growth of SMBHs have become even more intriguing and

challenging to explain. In this section, we first review the current methods used to measure the BH masses at high redshift (Section 4.1), then give an overview of the properties of the observed population (Section 4.2) and the implications for early BH seeds and growth (Section 4.3). Finally, we briefly describe additional methods that in the near future can be used to improve current BH mass estimates at high redshift (Section 4.4).

#### 4.1. Black Hole Mass Measurements in High-Redshift Quasars

The spectra of  $z \gtrsim 6$  quasars show the typical signatures of broad (FWHM of thousands of  $\text{km s}^{-1}$ ) emission lines that are superimposed on the power-law continuum emission of the quasar's accretion disk. These broad lines are thought to emerge from a region very close to the accreting BH (the so-called BLR) and thus provide a unique tool to constrain the properties of the central BH. The size of the BLR scales with the quasar luminosity, and the width of the lines is a measure of the potential depth (Peterson et al. 2004). Thus, a single-epoch spectrum gives enough information to estimate the mass of the central accreting BH (Vestergaard & Osmer 2009).

One of the most reliable estimators of BH mass and Eddington ratio is the  $\text{H}\beta$  line (e.g., Park et al. 2012). At  $z > 6$ ,  $\text{H}\beta$  is shifted to the MIR and is thus not accessible from the ground. As an alternative, the  $\text{CIV } \lambda 1549$  and  $\text{MgII } \lambda 2800$  lines have been extensively used to measure BH masses of quasars at these redshifts (e.g., De Rosa et al. 2014, Farina et al. 2022). Estimates based on the high-ionization  $\text{CIV}$  line are uncertain, as this line shows large velocity offsets, implying significant nonvirialized motions (Park et al. 2017, Mejía-Restrepo et al. 2018). Furthermore, there is mounting evidence that large  $\text{CIV}$  blueshifts ( $> 2,000 \text{ km s}^{-1}$ ) are more common at  $z > 6$  than at lower redshifts (e.g., Meyer et al. 2019, Schindler et al. 2020; see also Section 5.4). Therefore, in this review, we only focus on results based on  $\text{MgII}$  measurements, which are thought to be the most reliable until  $\text{H}\beta$ -derived masses are possible (Bahk et al. 2019; see Section 4.4).

One of the most widely used relations for BH mass estimation in high-redshift quasars includes the following:

$$M_{\text{BH}} = 10^{6.86} \left[ \frac{\text{FWHM}(\text{MgII})}{1,000 \text{ km s}^{-1}} \right]^2 \left[ \frac{L_{3000}}{10^{44} \text{ erg s}^{-1}} \right]^{0.5} M_{\odot}, \quad 4.$$

where  $\text{FWHM}(\text{MgII})$  is the full width at half maximum of the  $\text{MgII}$  line, and  $L_{3000}$  is the luminosity at  $3000 \text{ \AA}$ . Vestergaard & Osmer (2009) presented the scaling relation from Equation 4. The intrinsic scatter in the relation is 0.55 dex, which dominates the uncertainty for individual measurements.

The theoretical maximum luminosity that a source can achieve when the gravitational and radiation forces are in equilibrium is called the Eddington luminosity (Eddington 1926). The Eddington luminosity for pure ionized hydrogen in spherical symmetry is defined as

$$\begin{aligned} L_{\text{Edd}} &= \frac{4\pi c G m_p M_{\text{BH}}}{\sigma_T} \\ &= 1.26 \times 10^{38} \text{ erg s}^{-1} \left( \frac{M_{\text{BH}}}{M_{\odot}} \right), \end{aligned} \quad 5.$$

where  $c$  is the speed of light,  $G$  is the gravitational constant,  $m_p$  is the mass of a proton, and  $\sigma_T$  is the Thomson scattering cross section. The ratio between the bolometric and Eddington luminosities (referred to as the Eddington ratio;  $\lambda_{\text{Edd}} = L_{\text{Bol}}/L_{\text{Edd}}$ ) is useful to assess the quasar population's accretion properties. Although several bolometric corrections are published in the literature (e.g., Runnoe et al. 2012, Trakhtenbrot & Netzer 2012, Duras et al. 2020), in this review (e.g., in

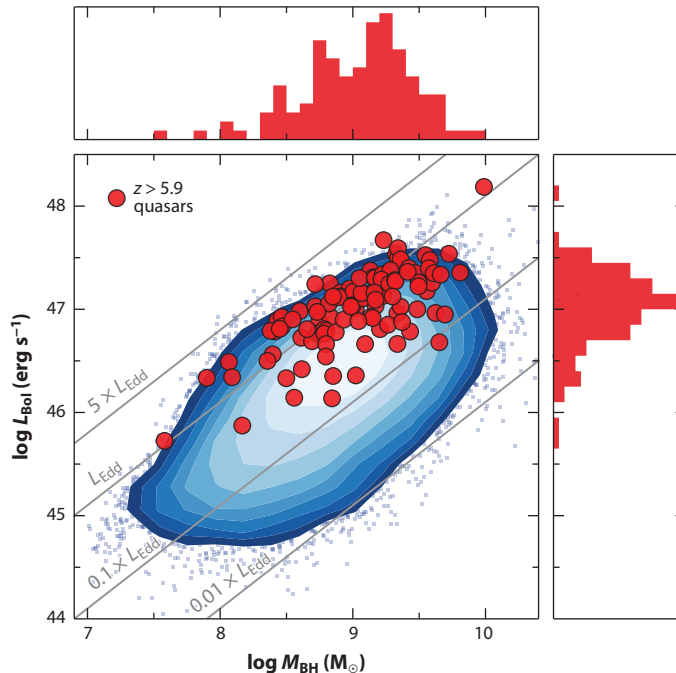


**Figure 6**

Bolometric luminosity versus BH mass. The blue contours and points show the distribution for low-redshift SDSS quasars, whereas the red circles are measurements for  $z > 5.9$  quasars. Solid gray lines show the location of constant accretion rate at 0.01, 0.1, 1, and 5 times the Eddington luminosity. All BH masses are from MgII measurements using Equation 4 and the bolometric luminosities are derived using Equation 6. Abbreviations: BH, black hole; SDSS, Sloan Digital Sky Survey.

**Figure 6**), we adopt the bolometric correction first presented by Richards et al. (2006a) and used in several studies of high-redshift quasars (e.g., Shen et al. 2011, Yang et al. 2021, Farina et al. 2022):

$$L_{\text{bol}} = 5.15 \times L_{3000}. \quad 6.$$

Farina et al. (2022) argued that bolometric luminosities estimated using Equation 6 are on average in between the ones calculated using the bolometric corrections from Runnoe et al. (2012) and Trakhtenbrot & Netzer (2012). In the high-redshift quasar database provided in the **Supplemental Material**, we report  $L_{3000}$  so readers can apply their preferred bolometric correction.

## 4.2. Current Demographics

At redshifts  $6.0 \lesssim z \lesssim 7.6$ , the MgII line falls in the NIR K band. The vast majority of the MgII-based BH masses come from NIR spectra taken with powerful ground-based telescopes such as Gemini, VLT, the Giant Magellan Telescope (GMT), and the Keck Observatory (Onoue et al. 2019, Shen et al. 2019, Yang et al. 2021, Farina et al. 2022). At the time of writing, there are 113 quasars at  $z > 5.9$  with reliable MgII-based BH mass estimates. Currently, there is a strong bias toward luminous ( $\gtrsim 10^{46}$  erg  $\text{s}^{-1}$ ) quasars, but obtaining reliable measurements for fainter sources is challenging with current facilities (see Onoue et al. 2019). We need JWST and Extremely Large Telescopes (ELTs) to enlarge the sample toward the faint end significantly. **Figure 6** shows

**Supplemental Material** >

the bolometric luminosity and BH mass distribution for all quasars with MgII-based masses at  $z > 5.9$ . The median BH mass is  $1.3 \times 10^9 M_\odot$ , whereas the least and most massive quasars are J0859+0022 at  $z = 6.39$  ( $\sim 4 \times 10^7 M_\odot$ ; Onoue et al. 2019) and J0100+2802 at  $z = 6.33$  ( $\sim 10^{10} M_\odot$ ; Wu et al. 2015), respectively.

The first samples of NIR spectroscopic observations of  $\gtrsim 6$  quasars showed that they accrete close to the Eddington limit, i.e.,  $\lambda_{\text{Edd}} \approx 1$  (e.g., Willott et al. 2003, Kurk et al. 2007, De Rosa et al. 2011). Extending the measurements to larger samples (Shen et al. 2019) or probing to fainter luminosities (Onoue et al. 2019) revealed a significant number of quasars accreting at sub-Eddington rates. The recent works by Yang et al. (2021) and Farina et al. (2022) analyzed some of the largest samples of NIR spectra of  $z \gtrsim 6$  quasars. Yang et al. (2021) studied 37 quasars at  $z > 6.3$  and found that these quasars have significantly higher Eddington ratios (mean of 1.08 and median 0.85) than a luminosity-matched quasar sample at low redshift. Farina et al. (2022) studied the NIR spectra of 135  $z \gtrsim 5.7$  quasars (including BH properties derived from MgII and CIV), finding that at  $z \sim 6$  the Eddington ratio distributions are consistent with a luminosity-matched low-redshift sample independent of the luminosity, whereas there is evidence for a mild increase in the median Eddington ratios for  $z \gtrsim 6.5$  (in agreement with Yang et al. 2021).

In our current compilation (**Figure 6**), the Eddington ratio ranges from 0.08 to 2.70, with a median of 0.79 and a mean of 0.92. Some 40 quasars exceed the nominal Eddington limit, and 8 have  $\lambda_{\text{Edd}} > 2$ . These values must be considered with caution as there is a substantial scatter in the BH mass estimations and bolometric corrections (see Section 4.1).

### 4.3. Constraints on Early Black Hole Seeds and Growth

As shown in **Figure 7**, the SMBHs powering the first quasars have quickly grown to enormous sizes, and explaining this mass growth remains challenging. Assuming a 100% duty cycle, the mass of the SMBH would grow exponentially as

$$M_{\text{BH}}(t) = M_{\text{BH,seed}} \times \exp \left[ (1 - \epsilon_r) \lambda_{\text{Edd}} \frac{t}{t_{\text{Sal}}} \right], \quad 7.$$

where  $\epsilon_r$  is the radiative efficiency, which is the efficiency of converting mass to energy, and the Salpeter time is defined as

$$t_{\text{Sal}} = \frac{\epsilon_r \sigma_{\text{T}} c}{4\pi G m_{\text{p}}} \approx \epsilon_r 450 \text{ Myr}. \quad 8.$$

Assuming  $\lambda_{\text{Edd}} = 1$  and  $\epsilon_r = 0.1$ , Equation 7 is equal to

$$M_{\text{BH}}(t) = M_{\text{BH,seed}} \times \exp \left[ \frac{t}{50 \text{ Myr}} \right]. \quad 9.$$

We used these assumptions for the growth tracks in **Figure 7**. We note that either a higher  $\epsilon_r$  or a <100% duty cycle would make the constraints on BH growth even tighter. **Figure 7** showcases how pushing the redshift frontier makes the formation and growth of SMBHs ever more challenging. Several potential theories have been developed to explain the existence of  $\sim 10^9 M_\odot$  BHs at  $z < 6$ . However, for the current redshift records at  $z \sim 7.5$ , at least under standard assumptions (i.e., Eddington-limited growth with  $\epsilon_r = 0.1$ ), only the heaviest seeds seem to be big enough to form these sources in such a short time, although they need to have sustained accretion during their entire lifetimes. For a thorough overview of the theoretical BH seeds, we refer to the review by Inayoshi et al. (2020). Other alternatives not represented in **Figure 7** involve radiative inefficient/highly obscured growth ( $\epsilon_r \ll 0.1$ ; Davies et al. 2019) or jet-enhanced accretion growth (Jolley & Kuncic 2008). According to Pacucci & Loeb (2022), the discovery of one  $\sim 10^{10} M_\odot$  BH at  $z \gtrsim 9$  would exclude the entire parameter space available for  $\sim 100 M_\odot$  seeds.

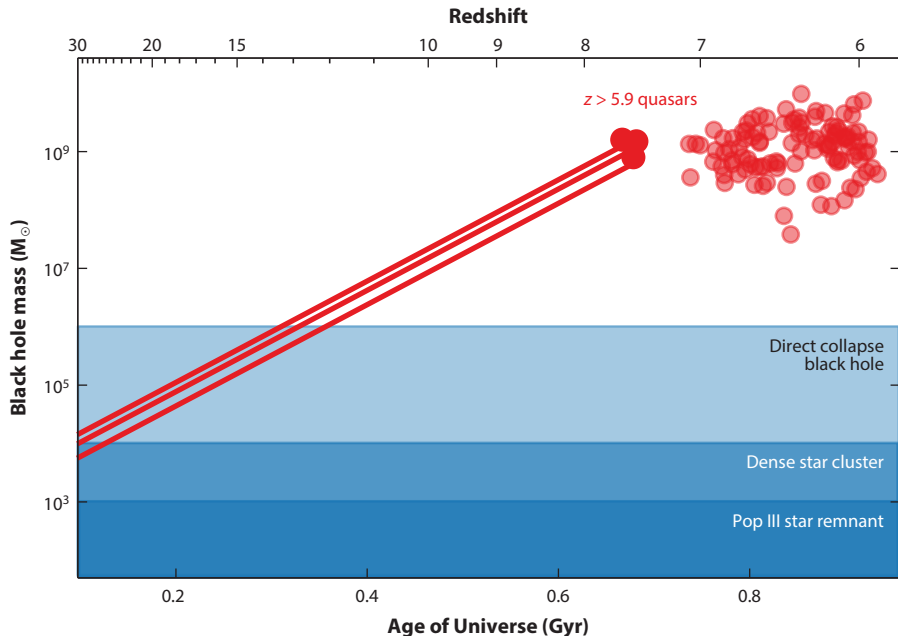


**Figure 7**

BH growth history: BH mass versus age of the Universe (redshift at the *top*). The red circles mark our compilation of robust MgII BH masses for  $z > 5.9$  quasars. The red lines show the growth history (assuming constant, maximum Eddington-limited accretion) of the most distant quasars at  $z > 7.5$ , which set the strongest challenges for BH formation theories. The shaded regions represent the mass ranges for popular BH seed formation scenarios (see Inayoshi et al. 2020). Abbreviation: BH, black hole.

However, it is important to note that these stringent constraints mainly apply to the most massive BHs at the highest redshift. For objects at lower redshift ( $z < 5$ ), SMBH growth is no longer strongly limited by the available cosmic time. In other words, there could be multiple channels of SMBH growth, and the channel with massive seeds and high accretion rate is required only for the formation of the most extreme objects.

#### 4.4. The (Near) Future for Black Hole Mass Measurements at High Redshift

We expect that future observations of high-redshift quasars with JWST and ALMA will improve their black hole mass measurements by using more robust mass estimators, and by directly resolving the black hole gravitational sphere of influence with gas dynamics.

**4.4.1. H $\beta$ -derived masses.** With JWST, robust H $\beta$ -based mass estimates of the most distant quasars finally has become feasible (see Section 4.1). The JWST instruments Near Infrared Spectrograph (NIRSpec) and Near Infrared Camera (NIRCam) can obtain spectroscopic observations of the H $\beta$  line in quasars at  $5 \lesssim z \lesssim 10$ . H $\beta$  BH masses are expected to be one of the first results from the first observations of high-redshift quasars with JWST.

**4.4.2. Direct dynamical mass measurements.** The unprecedented resolution provided by ALMA can spatially resolve the sphere of influence of central BHs in nearby galaxies, enabling direct gas-dynamical BH mass measurements (e.g., Cohn et al. 2021). The sphere of influence is

the region where the SMBH dominates the gravitational potential; its radius is commonly defined as

$$r < \frac{GM_{\text{BH}}}{\sigma^2}, \quad 10.$$

where  $G$  is the gravitational constant,  $M_{\text{BH}}$  is the mass of the BH, and  $\sigma$  is the stellar velocity dispersion. For reference, the radius of influence of a  $10^9$ - $M_{\odot}$  SMBH in a galaxy with  $\sigma = 150 \text{ km s}^{-1}$  is  $\sim 190 \text{ pc}$ .

Obtaining a direct kinematic mass measurement of an SMBH at  $z > 6$  would be tremendously important to corroborate that the mass scaling relations used thus far (Equation 4) still hold at the highest accessible redshifts. Recent ALMA observations of the [CII] emission line in  $z > 6$  quasar hosts are approaching resolutions comparable with the expected sphere of influence of SMBHs (e.g., Walter et al. 2022). We anticipate that in the upcoming years, such measurement will be possible, at least for some selected objects, and this will be an active area of research with the Next Generation Very Large Array (ngVLA) (Carilli & Shao 2018).

## 5. A MULTIWAVELENGTH VIEW OF QUASAR/GALAXY COEVOLUTION AT THE HIGHEST REDSHIFTS

In the local Universe there are tight correlations between the mass of the central SMBHs and the stellar bulge of the galaxy (see the review by Kormendy & Ho 2013). When and how these tight correlations arose is an open question. Constraints at the highest redshifts can provide essential clues when the time to grow a galaxy and BH is limited. Did the BH grow first and the galaxy follow? Vice versa? Or did they grow together? What are the main feedback mechanisms? How are the massive galaxies hosting quasars connected to their large-scale environment?

In this section, we first review the current efforts to detect the gas reservoirs required for the growth of the central SMBH and the formation of stars (Section 5.1). We then give an overview of the efforts to measure the stellar UV light from the  $z > 6$  quasar hosts and the recent successes in constraining their cold dust and gas via (sub)millimeter observations (Section 5.2). We then discuss how we can use this information to constrain BH/galaxy coevolution (Section 4.3) and describe observational evidence (or lack thereof) of quasar feedback (Section 5.4). Finally, we give an overview of the efforts for using  $z \gtrsim 6$  quasars as signposts for overdensities and large-scale structure in the early Universe (Section 5.5).

### 5.1. Quasar Fueling: Ly $\alpha$ Nebulae

Enormous gas reservoirs are required to grow the SMBHs seen in the highest-redshift quasars continuously. Extended Ly $\alpha$  nebulae (also referred to as Ly $\alpha$  halos) trace the cold gas reservoirs likely feeding the central SMBH. In principle, such gas reservoirs are likely also star-forming regions (Haiman & Rees 2001, Di Matteo et al. 2017). The first efforts to look for these nebulae used narrow-band filters centered on the expected Ly $\alpha$  emission (e.g., Goto et al. 2009, Decarli et al. 2012, Momose et al. 2019) and deep long-slit spectroscopy (e.g., Willott et al. 2011, Roche et al. 2014). The implications of these detections (as well as nondetections) were often difficult to interpret due to slit and narrow-band flux losses. Sometimes the same quasar observed with narrow-band imaging and long-slit spectroscopy yielded conflicting results.

The search for these Ly $\alpha$  nebulae had a significant step forward with the new integral field spectrographs (IFS) mounted on 8-m-class telescopes, particularly Multi Unit Spectroscopic Explorer (MUSE) on the VLT. IFS enabled 3D morphology/kinematics of the Ly $\alpha$  halos (Drake et al. 2019). The most comprehensive search for Ly $\alpha$  halos to date is the REQUIEM (Reionization Epoch QUasar InvEstigations with MUSE) survey (Farina et al. 2019), targeting

31  $z > 5.7$  quasars with VLT/MUSE. REQUIEM revealed 12 Ly $\alpha$  nebulae with a range of luminosities and morphologies extending up to 30 kpc. Recently, Drake et al. (2022) reported that the Ly $\alpha$  morphology and kinematics seem decoupled from the gas in the host galaxies as traced by [CII] emission. This result might imply that the observed Ly $\alpha$  halos are being powered by the central SMBH instead of tracing star formation, in line with recent simulations (Costa et al. 2022). Nevertheless, the resonant nature of the Ly $\alpha$  line makes it difficult to disentangle the AGN/star-formation contribution completely. IFS observations of additional nonresonant lines (e.g., H $\alpha$  with JWST) will be needed to confirm these results.

## 5.2. Quasar Host Galaxy Observations: Sites of Massive Galaxy Evolution

Given the extreme luminosities and inferred BH masses of these quasars, we would expect that they reside in hosts with significant stellar mass already in place (Kormendy & Ho 2013). However, the brightness of their central accreting BHs has prevented direct detection of the underlying starlight at (observed) optical and NIR wavelengths even with the *Hubble Space Telescope* (HST; e.g., Mechtley et al. 2012, Marshall et al. 2020). JWST’s unprecedented resolution, sensitivity, and wavelength coverage should overcome most of the shortcomings of previous attempts, as Marshall et al. (2021) have demonstrated with simulations. Several cycle 1 JWST programs attempt to reveal the stellar light of  $z \gtrsim 6$  quasar hosts for the first time.

The radiation at observed FIR to millimeter wavelengths of  $z \gtrsim 6$  quasars is dominated by the reprocessed emission from cool/warm dust in the host galaxy. These wavelengths provide the best window to study host galaxy properties, minimizing contamination from the quasar’s accretion disk emission. Pioneering works pushed the limits of millimeter and radio facilities to characterize the dust and the molecular and atomic gas in the first bright  $z \gtrsim 6$  quasars discovered (e.g., Bertoldi et al. 2003; Walter et al. 2003; Maiolino et al. 2005; Beelen et al. 2006; Wang et al. 2007, 2008). These studies were only sensitive to the most luminous systems and found that about one-third of high-redshift quasar host galaxies have luminosities comparable with those of hyperluminous IR galaxies ( $L_{\text{FIR}} \sim 10^{13} L_{\odot}$ ). Assuming the dust heating came from starburst activity, this suggested enormous star-formation rates (SFRs) of 100–1,000  $M_{\odot} \text{ year}^{-1}$ . Therefore, these early studies showed that early SMBH growth can be accompanied by extended, intense star formation and large reservoirs of dense and enriched molecular gas.

Rapid progress has been made in FIR observations of high-redshift quasar host galaxies with the advent of ALMA and major upgrades on the NOEMA interferometers (conveniently located in different hemispheres). The greatest advances can be divided into three major areas: (a) sensitivity, (b) resolution, (c) multiline tracers of the ISM.

**5.2.1. Sensitivity.** The [CII] $_{158 \mu\text{m}}$  fine-structure line, which is the primary coolant of the cold neutral atomic medium, has become the workhorse for studies of  $z \gtrsim 6$  quasar hosts. This was the natural choice as [CII] is one of the brightest emission lines in star-forming galaxies, and its frequency at  $z > 6$  is conveniently located in a high-transmission atmospheric window visible with ALMA and NOEMA. [CII] detections using the early generation of interferometers were challenging. By the time of the review of Carilli & Walter (2013), there were only two  $z \gtrsim 6$  quasars with [CII] detections, whereas now that number is  $\sim 80$ . [CII] line and IR continuum luminosity measurements provide independent estimates of SFR. **Figure 8** shows a recent compilation of the [CII] and IR luminosities and SFRs for  $z \gtrsim 6$  quasar hosts.

Early ALMA results demonstrated the ALMA’s ability to study [CII] emission from quasar hosts of both UV bright and UV faint  $z \gtrsim 6$  quasars (Wang et al. 2013, Willott et al. 2013). These studies motivated the push to larger samples, marking the transition from studies of individual interesting sources to the first statistical samples. Decarli et al. (2018) and Venemans et al. (2018)

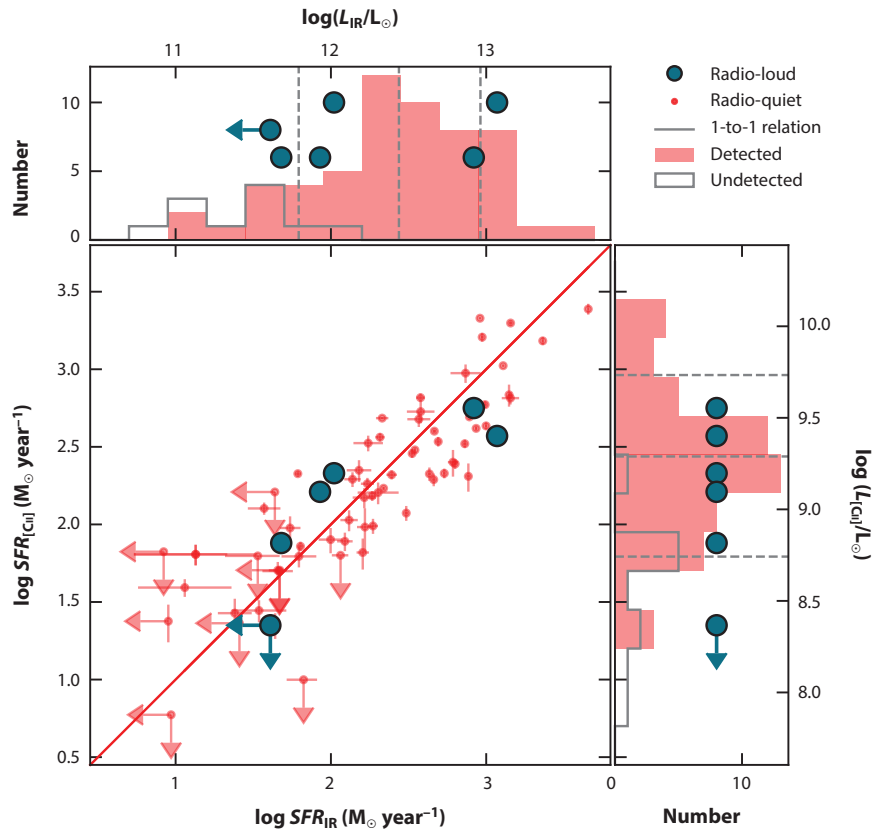


**Figure 8**

Star-formation distributions for radio-quiet (*small points*) and radio-loud (*circles*) quasars at  $z \gtrsim 6$ , derived from [CII] and IR luminosities. Figure adapted from Khusanova et al. (2022).

presented results from an ALMA snapshot survey of a large sample of luminous  $z \sim 6$  quasars to study their FIR continuum and [CII] properties. Remarkably, even with an integration time of  $\lesssim 15$  min on ALMA, the detection rate is  $\gtrsim 90\%$  for these quasars. They found typical [CII] luminosities of  $10^9$ – $10^{10} L_\odot$ , FIR luminosities of  $0.3$ – $13 \times 10^{12} L_\odot$ , and estimated dust masses of  $10^7$ – $10^9 M_\odot$  with SFRs ranging from 50 to  $2,700 M_\odot \text{ year}^{-1}$ . ALMA also enabled detections of FIR continuum and [CII] emission in a significant number of UV-faint quasars at high redshift (e.g., Izumi et al. 2018, 2019). Overall, there are only weak correlations between the bolometric luminosity of quasars (dominated by emission from accretion disk in the rest-frame UV/optical) and the FIR luminosity of the quasar hosts (dominated by star formation).

**5.2.2. Resolution.** The unprecedented spatial resolution of ALMA allowed imaging of the ISM of  $z > 6$  quasar host galaxies at subkiloparsec resolution for the first time. The first studies at kiloparsec scales ( $\sim 0.2$ – $0.3$  arcsec) revealed interesting morphological characteristics. For example, Shao et al. (2017) found ordered motion in a  $z = 6.13$  host that can be modeled with a rotating disk, Venemans et al. (2017a) report a remarkably compact ( $\lesssim 1$  kpc) host galaxy at  $z = 7.08$  that does not exhibit ordered motion on kiloparsec scales, and Bañados et al. (2019a) showed that a galaxy merger hosts a  $z = 7.54$  quasar.

Venemans et al. (2020) presented a survey of 27 host galaxies at  $z \sim 6$  imaged at kiloparsec scale with ALMA. They showed that the [CII] emission in the bright, central regions of the quasars have sizes of 1.0–4.8 kpc and are typically more extended than the dust continuum emission. The implied SFR densities at the center of these quasar hosts are a few hundred  $M_{\odot} \text{ year}^{-1} \text{ kpc}^{-2}$ , which is below the Eddington limit for star formation (although there are examples of host galaxies forming stars at near the maximum possible rate; e.g., Andika et al. 2020, Yue et al. 2021b). Neeleman et al. (2021) modeled the kinematics of these 27 host galaxies. They found a large diversity in the quasar host properties. About one-third of the galaxies show smooth velocity gradients consistent with emission from a gaseous disk. About one-third have no evident velocity gradients, with their kinematics dominated by random motion. The final one-third exhibit signatures of close companion interaction or galaxy merger activities (see Figure 9 for examples). The highest-resolution observations that currently exist for  $z > 6$  quasars are 400 pc for a quasar host at  $z = 6.6$  (Venemans et al. 2019) and 200 pc for a host galaxy at  $z = 6.9$  (Walter et al. 2022). These two studies highlight

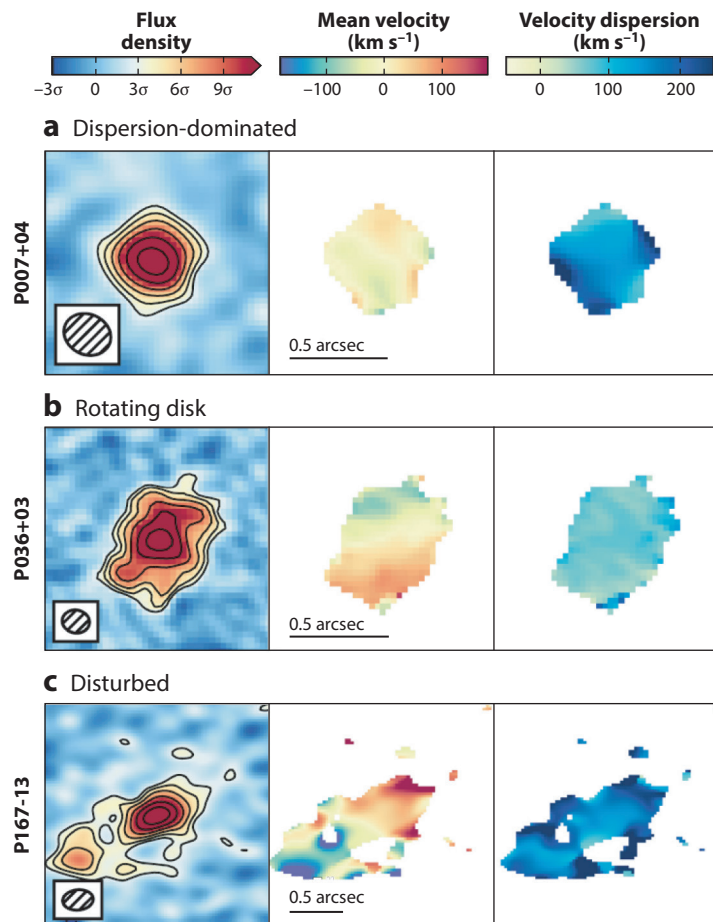


**Figure 9**

ALMA [CII] observations of quasar hosts reveal diverse morphologies and kinematics. The figure shows (a) a dispersion-dominated galaxy, (b) a galaxy consistent with a rotating disk, and (c) a disturbed galaxy with an ongoing merger. Figure adapted from Neeleman et al. (2021).

the power of ALMA by revealing complex morphologies, [CII] cavities in the gas distribution, and in one case very compact dust continuum and [CII] emission, reaching extreme densities in the central 200 pc from the SMBH. We expect that observations at comparable resolution or higher will be an active area of investigation in the near future.

A key result of these morphological studies is that the population of host galaxies of luminous early quasars is diverse. Although, on average, they are sites of massive galaxy assembly, they also appear to be in different evolutionary phases. Apparently, the peak of quasar activity is not tied to a particular stage of early galaxy formation in those systems.

**5.2.3. Multiline diagnostics.** Even though the [CII] emission line is important for redshift determination and gas dynamics (as discussed above), it cannot constrain the physics of the ISM by itself. A suite of emission lines tracing various phases of the ISM is required to characterize the physical conditions such as temperature, ionization, density, and metallicity. At the time of writing, this is an area of rapid development, and about a dozen quasar hosts have been detected in more than one tracer. Some of the main targeted lines (in addition to [CII]) include the following:

- The neutral carbon emission [CI] 369  $\mu\text{m}$  line, which traces the atomic medium in the external shells of molecular clouds (e.g., Yang et al. 2019a, Pensabene et al. 2021)
- Two transitions of the [NII] line (205  $\mu\text{m}$  and 122  $\mu\text{m}$ ), which is a pure tracer of the ionized medium and can be used to measure the fraction of [CII] associated with the neutral medium (e.g., Novak et al. 2019, Li et al. 2020)
- The [OI] 146  $\mu\text{m}$  line, which is sensitive to the temperature of the atomic gas in the galaxy (e.g., Li et al. 2020, Meyer et al. 2022b)
- The [OIII] 88  $\mu\text{m}$  line, which provides critical diagnostics for the conditions of star formation and the properties of massive stars (e.g., Walter et al. 2018, Hashimoto et al. 2019, Novak et al. 2019)
- Several rotational CO transitions, considered as the main probe of the molecular gas in dense star-forming regions (e.g., Gallerani et al. 2014, Venemans et al. 2017b, Novak et al. 2019, Yang et al. 2019a, Pensabene et al. 2021, Decarli et al. 2022, Li et al. 2022b)
- Several water lines that arise in the warm, dense phase of the ISM and a number of OH molecular lines that are usually associated with outflows of dense material (e.g., Yang et al. 2019a; Pensabene et al. 2021, 2022)

A combination of these different tracers yields molecular gas masses in the range  $M_{\text{H}_2} \sim 10^{10} - 10^{11} M_{\odot}$ , and ISM metallicities comparable with the solar value. Generally, the observed luminosities are better modeled by photodissociation regions instead of X-ray-dominated regions (see the review by Wolfire et al. 2022). The current small sample of quasars with multiple ISM tracers is highly biased toward objects bright in [CII]. We expect that the characterization of physical conditions of the ISM in early massive galaxies will be expanded to much larger samples.

### 5.3. Constraints on Galaxy Mass and Black Hole/Galaxy Coevolution

Dynamical masses of the quasar hosts can be measured using spatially and kinematically resolved line observations (see Section 5.2). The dynamical mass enclosed within a radius  $R$  is typically expressed as:

$$M_{\text{dyn}} = \frac{v_{\text{circ}}^2}{G} R, \quad 11.$$

where  $G$  is the gravitational constant, and  $v_{\text{circ}}$  is the maximum circular velocity of the gas disk. Obtaining  $v_{\text{circ}}$  is not trivial, as it requires knowing the inclination angle of the galaxy. Estimates

of dynamical masses combined with robust BH masses (Section 4.1) make it feasible to push BH/galaxy coevolution studies to the highest accessible redshifts.

Wang et al. (2010) measured dynamical masses using CO emission from 8 quasar hosts at  $z \sim 6$ . Assuming an average inclination angle of 40 deg and  $R = 2.5$  kpc, they found that the  $z \sim 6$  quasars have, on average, SMBHs a factor of 15 more massive than expected from the local BH–bulge mass relation. This result suggests that BHs in high-redshift quasars either got a major head-start or grew faster than their host galaxies; if the  $M$ – $\sigma$  relation existed at  $z \sim 6$ , then it would show a strong cosmic evolution. Numerous subsequent works have focused on the correlation of SMBH mass and galaxy dynamical mass at these redshifts (e.g., Wang et al. 2016, Decarli et al. 2018). Most of these studies had to assume an inclination angle and/or an average size for the emitting gas. Neeleman et al. (2021) carried out careful dynamic modeling of their [CII] observations (including inclination and size). They found a mean dynamical mass of  $\sim 5 \times 10^{10} M_{\odot}$  for a sample of luminous  $z \sim 6$  quasars with  $\sim 10^9 M_{\odot}$  BHs. As shown in **Figure 10**, this places them about one order of magnitude above the local relation. It is important to note that the relationship could be strongly affected by potential biases from selection and by using gas tracers (Volonteri & Stark 2011, Huang et al. 2018). Indeed, observations of low luminosity quasars show a narrower [CII] line width (e.g., Willott et al. 2017, Izumi et al. 2018), placing them close to the local relation.

Habouzit et al. (2022) analyzed the coevolution of SMBHs and their host galaxies in six cosmological simulations with different models for SMBH growth. Although the simulations are all

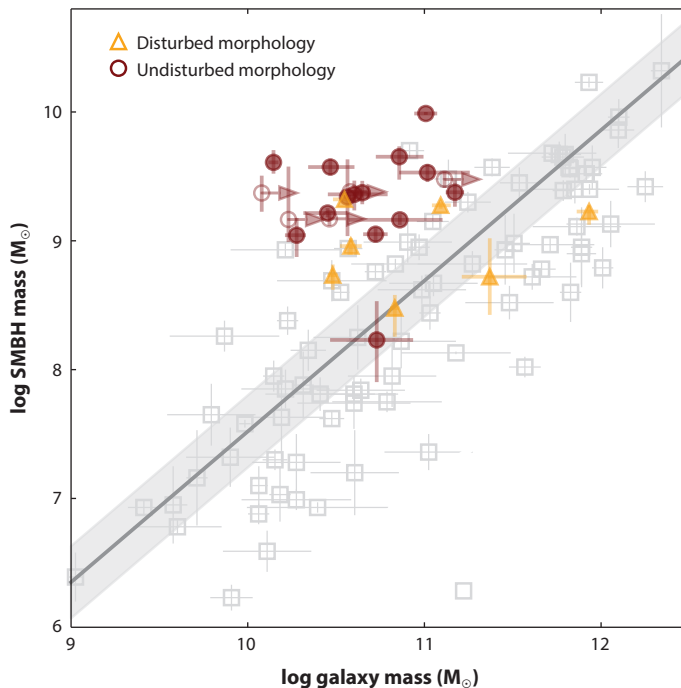


**Figure 10**

Black hole mass versus host dynamical mass for  $z \gtrsim 6$  quasars. The gray points are local galaxies, and the shaded region is the best-fit local relation (Kormendy & Ho 2013). The  $z \gtrsim 6$  sample is divided by their [CII] morphology (see *legend*), and it is generally above the local relation. Figure adapted from Neeleman et al. (2021). Abbreviation: SMBH, supermassive black hole.

consistent at  $z \sim 0$ , they diverge at  $z > 5$ , highlighting the importance of obtaining robust observational constraints at these redshifts. Li et al. (2022a) argued that to robustly confirm whether the highest-redshift quasar population resides above the local BH–bulge mass relation, an improvement in the accuracy of mass measurements and an expansion of the current sample to lower BH masses is required. We expect that JWST will enable significant advances for BH and host galaxy masses.

## 5.4. Evidence of Quasar Feedback

Central accreting SMBHs play an important role in shaping galaxy evolution (see the review by Fabian 2012). Indeed, to reproduce the observed distribution of galaxy masses at  $z = 0$ , simulations require that strong AGN feedback was already in place at  $z \sim 6$  (e.g., Kaviraj et al. 2017). Below, we list some of the observational evidence (with caveats) that these feedback mechanisms are taking place in the  $z \gtrsim 6$  quasar population.

**5.4.1. UV line shifts.** High-redshift quasars show asymmetric shape and velocity offset of high-ionization lines, in particular the C IV line. The low-redshift quasar population shows an overall blueshifted C IV line ( $\sim 800 \text{ km s}^{-1}$ ) compared to the systemic redshift of the quasar (e.g., traced by H $\beta$ ; Shen et al. 2011). This shift is generally understood in the context of a strong accretion disk wind that contributes to the high-ionization lines (e.g., Richards et al. 2011). At  $z > 6$ , the C IV line velocity shift is much stronger ( $\sim 1,800 \text{ km s}^{-1}$ ; Schindler et al. 2020). Meyer et al. (2019) suggested that this redshift evolution can be explained by the C IV winds being launched from the disk with an increased torus opacity at this redshift.

**5.4.2. Broad absorption line quasars.** A fraction of quasars show broad and highly blue-shifted absorption features in their rest-frame UV transitions. BAL features trace ionized winds in the BLR and are recognized signatures of SMBH feedback. Bischetti et al. (2022) used high-quality spectra of quasars from the XQR30 survey to show that up to  $\sim 50\%$  of luminous quasars at  $z \sim 6$  exhibit BAL features (with outflow velocities up to 17% of the speed of light), compared to about 20% observed in low-redshift samples. Yang et al. (2021) studied 37 quasars at  $6.3 < z < 7.64$  and reported a BAL fraction of  $\sim 24\%$ , which is smaller than the Bischetti et al. (2022) work but still slightly greater than what is observed at lower redshifts. This potential evolution of the BAL fraction could be a result of the strong feedback associated with the rapid BH growth and galaxy assembly in the early Universe.

**5.4.3. Ly $\alpha$  halos.** The existence of extended Ly $\alpha$  nebulae around  $z \gtrsim 6$  quasars was discussed in Section 5.1. Recently, Costa et al. (2022) performed a suite of cosmological, radiation-hydrodynamic simulations to understand the origin and properties of the observed Ly $\alpha$  halos. The simulations unambiguously require quasar-powered outflows to match the observed properties at  $z \gtrsim 6$ , providing indirect evidence for AGN feedback.

**5.4.4. Radio jets.** Only six galaxies hosting radio-loud quasars at  $z \gtrsim 6$  have been studied with ALMA and NOEMA (Rojas-Ruiz et al. 2021, Khusanova et al. 2022). Assuming no AGN contribution, their [C II]- and FIR-derived star-formation properties are consistent with those reported for the much more studied radio-quiet quasars (c.f. Decarli et al. 2018, Venemans et al. 2020; see **Figure 8**). However, Rojas-Ruiz et al. (2021) and Khusanova et al. (2022) show indirect evidence that the FIR emission of radio-loud quasars can be strongly affected by synchrotron emission. In that case, their IR-derived SFRs can be overestimated, implying that we might be witnessing negative AGN feedback at  $z > 6$ . However, more measurements of the FIR continuum and/or an enlarged sample are required to quantify the potential impact on the population.

**5.4.5. Broad components of [CII] emission.** Broad wings ( $\gtrsim 1,000 \text{ km s}^{-1}$ ) in the [CII] emission lines are thought to be caused by AGN outflows. The observational evidence for these [CII] broad wings remains tentative, as different analyses of similar data sets provide inconsistent results. For example, Maiolino et al. (2012) and Cicone et al. (2015) reported a strong [CII] outflow in the host galaxy of the quasar J1148+5251 at  $z = 6.42$ . In contrast, Meyer et al. (2022b) found no evidence of a broad velocity component but reported that J1148+5251 has the most spatially extended [CII] emission ( $\sim 10 \text{ kpc}$ ) among  $z \sim 6$  quasar hosts. Izumi et al. (2021) reported a broad ( $\sim 1,000 \text{ km s}^{-1}$ ) [CII] wing in the spectrum of a quasar at  $z = 7.07$ , and Khusanova et al. (2022) reported a tentative [CII] broad component that could be as wide as  $\sim 1,400 \text{ km s}^{-1}$  in a BAL radio-loud quasar at  $z = 6.12$ . Bischetti et al. (2019) stacked the [CII] spectra of 48 quasars at  $4.5 < z < 7.1$  and reported a broad [CII] component, whereas Decarli et al. (2018) stacked the [CII] spectra of 23  $z \sim 6$  quasar hosts and found no evidence for a [CII] broad component. Novak et al. (2020) stacked the [CII] spectra using different techniques (spectral stacking and UV-plane stacking) and found no evidence for [CII] broad-line emission. Novak et al. (2020) argued that the results can depend on the stacking techniques and resolution (e.g., if the resolution is low, nearby companions can be confused with [CII] wings).

**5.4.6. OH absorption.** The hydroxyl molecule (OH) in absorption traces high-velocity molecular inflow or outflows (see the review by Veilleux et al. 2020). Herrera-Camus et al. (2020) report the first tentative detection ( $3\sigma$ ) of the OH 119- $\mu\text{m}$  doublet in absorption toward a  $z \gtrsim 6$  quasar, suggesting the presence of a molecular outflow. Outflow signatures from both atomic and molecular lines will be a focus of future high-quality ALMA observations.

## 5.5. Protoclusters and Large-Scale Structure

Theoretical models predict that  $z \gtrsim 6$  quasars should be highly biased tracers of the underlying dark matter distribution, signposting the first overdensities of galaxies on megaparsec scales, i.e., protoclusters (e.g., Costa et al. 2014, Overzier et al. 2009) (but some scatter is expected; see, e.g., Ren et al. 2021). Observationally, this has been challenging to demonstrate. Photometric selection around high-redshift quasars has found evidence for overdensities (e.g., Utsumi et al. 2010, Morselli et al. 2014), densities comparable with random fields (e.g., Bañados et al. 2013, Simpson et al. 2014, Mazzucchelli et al. 2017a), and even underdensities (e.g., Kim et al. 2009).

There are currently two  $z \gtrsim 6$  quasar fields with robust overdensities (i.e., including spectroscopic confirmation) on megaparsec scales (Mignoli et al. 2020, Overzier 2022; see **Figure 11**). These are SDSS J1030+0524 at  $z = 6.3$  and SDSS J0836+0054 at  $z = 5.8$ . The works by Stiavelli et al. (2005), Kim et al. (2009), Simpson et al. (2014), Balmaverde et al. (2017), and Decarli et al. (2019b) were crucial for confirming the overdense environment of J1030+0524. Similarly, Zheng et al. (2006), Ajiki et al. (2006), and Bosman et al. (2020) were fundamental for confirming the large-scale structure around J0836+0054. Recently, Yue et al. (2021a) report the first quasar pair known at  $z \sim 6$  (with a projected separation  $< 10 \text{ kpc}$ ), implying a rich environment that still awaits confirmation at larger scales.

ALMA observations of  $z \sim 6$  quasar hosts (see Section 5.2) have serendipitously detected a population of [CII]-bright companion galaxies in the immediate environment of  $\sim 20\text{--}50\%$  of the targeted quasars (Decarli et al. 2017, Neeleman et al. 2019, Venemans et al. 2020; see also **Figure 9c**). The large fraction of such quasar–galaxy pairs exceeds by orders of magnitude the expectations based on the current constraints of the number density of [CII]-bright galaxies at these redshifts. Three out of five quasar companions with deep HST observations remain undetected (Decarli et al. 2019a, Mazzucchelli et al. 2019), implying a significant part of a potential

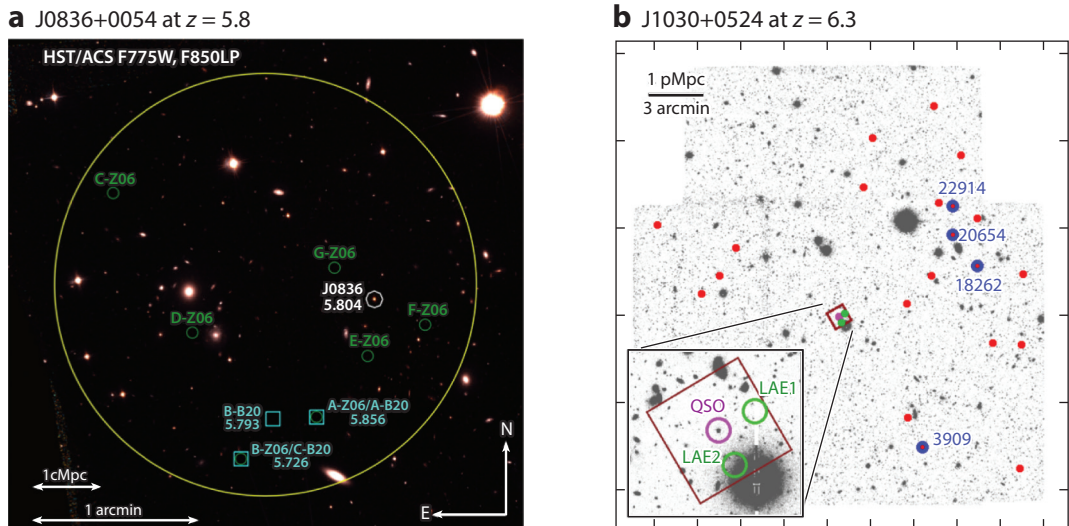


**Figure 11**

The two  $z \gtrsim 6$  quasars with robust overdensities on  $\gtrsim 1$ -Mpc scales. (a) Field around J0836+0054 at  $z = 5.8$ . Cyan squares (green circles) show spectroscopically confirmed (photometrically selected) galaxies at a redshift consistent with the quasar. Figure adapted from Overzier (2022). (b) Field around J1030+0524 at  $z = 6.3$ . Red dots show photometrically selected galaxies at a redshift consistent with the quasar. Blue and green circles are spectroscopically confirmed galaxies at a redshift consistent with the quasar. Figure adapted from Mignoli et al. (2020). Abbreviations: HST/ACS, *Hubble Space Telescope/Advanced Camera for Surveys*; LAE, Lyman- $\alpha$  emitter; QSO, quasi-stellar object.

large-scale structure might be obscured. The two HST-detected companions show tentative evidence of AGN activity (Connor et al. 2019, Vito et al. 2019a; but see also Vito et al. 2021).

The field of view of ALMA is too small to study whether these gas-rich companions exist in large numbers over megaparsec scales as predicted by simulations. MUSE observations of one of these quasar/companion fields reveal two additional Lyman- $\alpha$  emitters (LAEs) in close proximity, strengthening the case for an overdensity (Meyer et al. 2022a). It is likely that the next leap on our understanding of the environment of the highest-redshift quasars will come with JWST. JWST's deep imaging, multiobject, and slitless spectroscopy capabilities will provide a new opportunity to probe the galaxy population in  $z \gtrsim 6$  quasar environments to unprecedented depth over the megaparsec scales.

## 6. QUASARS AS PROBES OF COSMIC REIONIZATION

Quasars are both agents and powerful probes of the cosmic reionization history. As rare but luminous sources with hard ionizing spectra, they contribute to the overall photon budget driving reionization together with stellar photons from galaxies. Absorption measured in quasar spectra from foreground gas has yielded many of the most sensitive constraints on the density, ionization, and chemical enrichment of this tenuous intergalactic material. Although quasars' utility as reionization probes has been understood since foundational work by Gunn & Peterson (1965), it has taken 40–50 years for quasar surveys to uncover objects deep into the reionization epoch and fully exploit the information that their absorption spectra encode (Fan et al. 2006b).

Although absorption studies have yielded many of the most precise constraints on the IGM opacity and neutral hydrogen fraction, they are subject to limitations on both systematic accuracy and physical interpretation. These limitations arise from multiple sources, but the most significant

factors discussed below are (a) uncertainty in the quasar’s intrinsic/unabsorbed spectral continuum, (b) the large on-resonance oscillator strength of H $\text{I}$  Ly $\alpha$ , which leads to a wide gap in sensitivity between neutral fractions of  $X_{\text{H I}} \sim 10^{-4}$  (where resonance absorption saturates) and  $\sim 10^{-1}$  (where damping wings appear), and (c) computational challenges of simulating representative volumes with inhomogeneous and rapidly evolving radiation fields.

## 6.1. Active Galactic Nuclei and the Ionizing Photon Budget

Quasar accretion produces a hard ionizing spectrum, making the AGN population a contributing source to the budget of photons needed for reionization. However, as detailed in the recent review by Robertson (2021) and references therein, there is an emerging consensus that AGNs play a subdominant role compared to galaxies as an overall driver of the phase transition, even when one extrapolates observed LFs to thresholds fainter than current detection limits. Jiang et al. (2022) further reinforced this conclusion by placing an upper limit on the contributions of low-luminosity AGNs to reionization using deep HST survey data. Finkelstein & Bagley (2022) have synthesized measurements across the literature of galaxy+AGN UV LFs, to estimate their relative contributions to the ionizing photon budget, using strong assumptions about the ionizing radiation escape fractions of each population. They estimate that AGNs supply  $\sim 10\%$  of the total ionizing photon budget at  $z \sim 5$ , which is roughly the lower limit of redshifts considered in our review. They found that this fraction drops rapidly toward higher redshift because of differential downward evolution in the QLF relative to galaxies. By  $z \sim 7$ , they estimate that AGNs contribute only 0.3–1.0% of all ionizing photons, declining by yet another order of magnitude by  $z \sim 9$ . In contrast, Giallongo et al. (2019) suggested that AGN contributions to the UV background can still be significant at  $z \sim 5.6$  based on X-ray-selected objects.

The quantitative uncertainties in these analyses are still considerable; Finkelstein et al. (2019) found a  $10\times$  higher contribution from AGNs at  $z \sim 7$  using different assumptions. Much of this may be attributed to uncertainties in the faint-end slope of the QLF. Still, the qualitative picture that reionization is heavily dominated by star-forming galaxies appears to remain fairly robust with respect to these uncertainties. The fractional contribution of quasars and AGNs increases toward lower redshift because of their rapidly rising number densities, such that they are more likely to dominate the metagalactic UV background in the at  $z < 4$  postreionization Universe. New surveys with the *Roman Space Telescope* and JWST should revolutionize this field, providing both deep, NIR color-selected objects deep into the EoR and sensitive spectra to confirm the AGN nature of faint candidates and separate them from star-forming galaxies.

## 6.2. Neutral Hydrogen Absorption in the Diffuse Intergalactic Medium

The optical depth from neutral Hydrogen in a matter-dominated Universe (appropriate for the redshifts considered here) is

$$\tau(\lambda_{\text{obs}}) = \frac{\pi e^2 f_{12}}{m_e c} \left( \frac{c}{H_0 \Omega_{\text{H}}^{1/2}} \int_0^z \frac{n_{\text{H I}}(z)}{(1+z)^{5/2}} \phi(c/[\lambda_0(1+z)]) dz \right). \quad 12.$$

The leading fraction has units of cross section per unit frequency in terms of the dimensionless oscillator strength  $f_{12}$ , which is an atomic constant determined for each ion ( $f_{12} = 0.416$  for Ly $\alpha$ ). The expression in brackets reflects a column density, i.e., an integral of the radial line element, weighted by the H $\text{I}$  density field. The function  $\phi(\nu)$  is a unity-normalized line shape. It is typically approximated as a Voigt profile, which consists of a deep Gaussian line core whose width is determined by internal velocities, convolved with a much wider but also much weaker Lorentzian wing. This so-called damping wing arises from an energy–time uncertainty in the Ly $\alpha$  transition, leading

to a small but nonzero absorption cross section in the rest frame for photons far from the resonance wavelength  $\lambda_{\text{rest}} = 1215.67 \text{ \AA}$ . Equation 12 indicates that the optical depth at each observed wavelength  $\lambda_{\text{obs}}$  contains contributions from neutral hydrogen at every intervening foreground redshift.

However, because  $\phi(v)$  is so sharply peaked around line resonance, the integral is almost always dominated by matter at the redshift where  $\lambda_{\text{obs}}/(1+z) = \lambda_{\text{rest}}$ . Directly at this resonance wavelength, the Ly $\alpha$  cross section is very large—roughly  $4 \times 10^{-14} \text{ cm}^2$ . Furthermore, the mean baryonic density increases toward high redshift as

$$\bar{n}_{\text{H}}(z) \sim \frac{\Omega_{\text{b}} \rho_{\text{c}}}{\mu m_{\text{H}}} (1+z)^3 = 8.6 \times 10^{-5} \left( \frac{1+z}{7} \right)^3 \text{ cm}^{-3}, \quad 13.$$

which increases both the total gas column density and the HI recombination rate, favoring a higher neutral gas fraction  $X_{\text{HI}}$ . Collectively these lead to a very large Ly $\alpha$  optical depth of  $\tau \sim 10^5$  if the IGM is 100% neutral.

However, observations show  $\tau = O(\sim 1)$  at  $2 < z < 4$ ; the presence of transmitted flux implies that the Ly $\alpha$  forest is only neutral at the  $X_{\text{HI}} \sim 10^{-5}$  level. The optical depth increases toward high redshift in tandem with the neutral fraction, but by the time the neutral fraction reaches  $X_{\text{HI}} \sim 10^{-4}$ , the optical depth already exceeds  $\tau > 5$ , at which point >99% of the background quasar’s light is absorbed. On-resonance line absorption is simply too strong to provide useful measurements of the neutral fraction  $X_{\text{HI}}$  above this value.

In contrast, the atomic cross section for a photon with wavelength in the Lorentzian damping wing is suppressed by 5–6 orders of magnitude relative to the peak at line center—even at small velocity offsets (100–200  $\text{km s}^{-1}$ ). The eponymous damped Lyman alpha (DLA) phenomenon is therefore only seen in small, rare high-overdensity environments with large column densities ( $N_{\text{HI}} > 10^{20}$ ) at  $z < 5$ .

Reionization is characterized by an increasing neutral fraction in the diffuse IGM, which eventually becomes strong enough to produce damping wings (Miralda-Escudé 1998). However, these are convolved with on-resonance absorption from HI at other redshifts, with the unique exception of the quasar’s immediate foreground, where the damping wing can extend redward of the Ly $\alpha$  emission line.

Bridging this gap between strong on-resonance absorption, whose measurements probe  $10^{-6} < X_{\text{HI}} < 10^{-4}$ , and weak off-resonance damping wings, which only emerge at  $X_{\text{HI}} > 10^{-1}$ , is a recurring theme for IGM measurements near the reionization epoch. On-resonance measurements are most useful in regions of locally enhanced ionization or at lower redshifts ( $z < 6.3$ ) toward the late stages of reionization. Damping wing measurements are most powerful at early times and higher neutral fractions seen for  $z > 7$ . Observational constraints are much less precise for the epochs in the range of  $6.3 < z < 6.8$ , when the neutral fraction evolved from 0.01% to 10%—the Ly $\alpha$  line absorption is saturated, but damping wings have not yet emerged.

**6.2.1. Numerical simulations.** Cosmological simulations play an essential role in interpreting the spectra of reionization-epoch quasars and placing their associated transmission measurements into a broader physical context. We refer the reader to an excellent recent review (Gnedin & Madau 2022) on theoretical and numerical reionization models for a comprehensive overview of key methods and simulation projects.

Briefly, simulations must confront several intersecting challenges in the attempt to reproduce the quasar spectral observables summarized below, together with LFs of reionization-era galaxy populations. An idealized simulation should have the following:

- A large box ( $L > 100$  cMpc) to cover many scale lengths of the galaxy–galaxy autocorrelation function and to sample the rare high-density peaks that could plausibly host  $M > 10^9 M_\odot$  SMBHs.
- Sufficient spatial and mass resolution to model disk galaxies realistically and resolve low-mass halos that produce light and heavy elements as well as small-scale features in the Ly $\alpha$  forest and Lyman limit systems that act as ionizing radiation sinks.
- Ray tracing of emergent radiation from individual galaxies to account for spatial variations in the density and ionizing background, shadowing from optically thick absorbers, or the timing of reionization.
- Full and self-consistent coupling of radiation to hydrodynamics to capture the effect of ionization heating, pressure smoothing, and adiabatic cooling on the evolving density field and ionization fraction. These will also impact the formation of subsequent stars and galaxies.

Computational limits prevent practical simulations from meeting all four of these requirements simultaneously, though rapid progress in recent years has allowed some groups to progress from analytic or seminumerical efforts to meet two or even three of the above bullets in single simulations. The Gnedin & Madau review contains a helpful classification of leading numerical projects according to their box sizes, hydro prescriptions, treatment of the UV background, and radiation–hydro coupling.

Although most large-scale simulations focus on reproducing global reionization signals such as the volume-averaged neutral fraction, a separate numerical tool kit has evolved specifically to interpret observations of proximity zones (Section 6.3.1) and damping wings (Section 6.3.2) produced in the immediate foreground of luminous quasars (see **Figure 12**).

These investigations begin with global simulations of the reionization-era IGM and introduce the effect of a high-luminosity quasar by hand in the simulation volume. A large parent simulation is searched for high-mass halos ( $M \geq 1\text{--}2 \times 10^{11} M_\odot$ ) representative of hosts where SMBHs are first thought to form. A bright quasar is then inserted at the center of the halo, emitting ionizing photons with a luminosity scaled to the absolute 1450-Å magnitude of known quasars and extrapolated to the Lyman edge using carefully constructed template SEDs. The simulation is then evolved forward to follow expansion of the ionization front or proximity zone into the IGM. Multiple sightlines are drawn through the simulation box, terminating at the quasar’s host halo, and simulated transmission spectra are extracted using the density, temperature, ionization, and velocity cubes.

This methodology has been adapted by several groups to place joint constraints on quasar lifetimes and the IGM neutral fraction at  $z > 7$  (Bolton et al. 2011, Keating et al. 2015, Davies et al. 2018b, Cen & Haiman 2000), and to estimate the ages of  $z \sim 6$  quasars from their proximity zone sizes (Bolton & Haehnelt 2007, Eilers et al. 2017, Chen & Gnedin 2021). In ionized proximity zones, the simulations can also be used to calibrate methods to reconstruct the fluctuating density field near the central host (Chen et al. 2022).

Essentially the simulations are used to generate statistical realizations of the matter distribution around massive quasar host halos, capturing nonlinear physics and scale-dependent correlations in a way that analytic PDFs of the optical depth and/or excursion set formalism cannot accomplish.

A completely separate class of simulations is beginning to address challenging questions about heavy element enrichment of the early IGM and CGM (Keating et al. 2016), for comparison with observation of heavy element absorption in  $z > 6$  quasar spectra. These simulations rely on sub-grid feedback prescriptions for metal production, which are then transported with standard hydro treatments as at lower redshift. Translation from metal abundances into observable column densities is more complicated than for H I, because the ionization balance of multilevel ions depends on

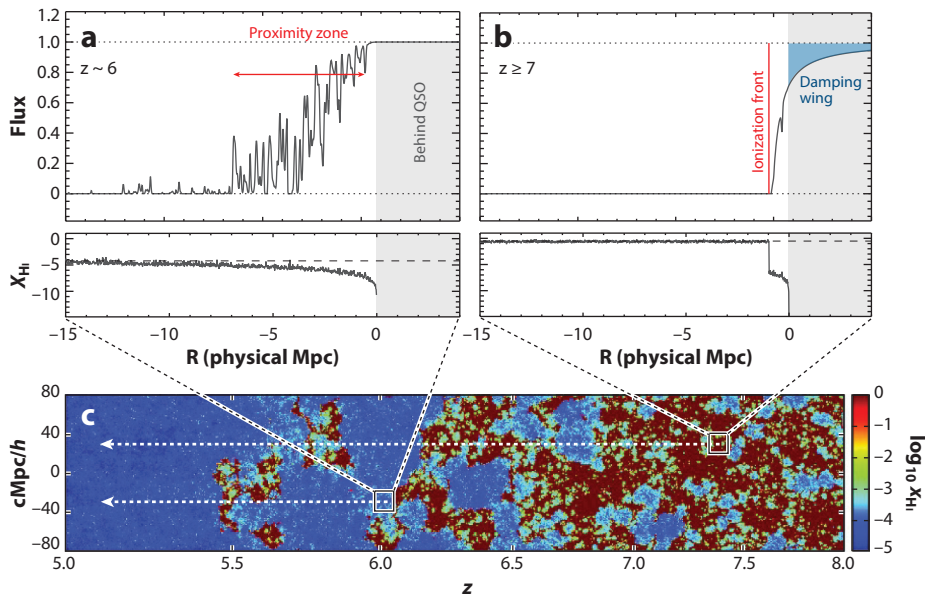


**Figure 12**

Observable properties and interpretation of proximity zones (*a*) and damping wings (*b*). In the simulation panel (*c*), each box represents the location of a background QSO whose sightline extends to the left. Proximity zones are studied at  $z \sim 5.8\text{--}6.5$  and represent regions of enhanced ionization from the QSO in an already ionized IGM. There is no absorption redward of the QSO's Ly $\alpha$  emission line (marked with a *gray shaded region*), and a region of low optical depth extends  $R_p \sim 5\text{--}10$  proper Mpc. Damping wings have only been detected at  $z \gtrsim 7$ , and represent ionization fronts penetrating into an IGM with a  $O(\sim 0.1)$  neutral fraction, shown with red color scale in the simulation. On-resonance absorption is saturated up to and very near the QSO's emission redshift, and the off-resonance damping wing (*shaded blue*) extends redward of Ly $\alpha$  in the QSO's rest frame. Constraints on the IGM neutral fraction come from this blue-shaded zone, as well as the very short run of unsaturated pixels between the QSO's systemic redshift and the end of the proximity zone. Figure adapted with permission from the simulations of Kulkarni et al. (2019a). Abbreviations: IGM, intergalactic medium; QSO, quasi-stellar object.

the UV background at other, often harder energies than the Lyman edge. A notable early effort in multifrequency treatment of an inhomogeneous background is the Technicolor Dawn simulation (Finlator et al. 2018), which tracks 24 separate frequencies and measures ionization balances of C IV and Si IV in the  $z > 5.5$  Universe, though with a much smaller box size ( $L \sim 12$  cMpc) than the aforementioned simulations designed to capture quasar host halos.

**6.2.2. Transmission measurements.** Before the discovery of  $z \gtrsim 6$  quasars, the evolving Ly $\alpha$  forest optical depth, which gradually increases with  $z$ , had been measured extensively at lower redshifts (Rauch et al. 1997, Becker et al. 2007) and interpreted as a product of the  $\bar{n} \propto (1+z)^3$  density field together with a smoothly evolving UV ionizing radiation background (Becker & Bolton 2013). Early discoveries of  $z > 6$  SDSS quasars (Fan et al. 2001) led to a reexamination of underlying assumptions about smooth evolution in  $X_{\text{HI}}$  approaching reionization. In particular, deep medium-resolution spectroscopy of one of the very first such objects—SDSS J1030+0524 at  $z = 6.3$ —revealed a region of Ly $\alpha$  forest absorption consistent with zero flux at wavelengths corresponding to  $5.95 < z < 6.16$  (Becker et al. 2001). This work has been interpreted as the first detection of a robust Gunn–Peterson absorption trough and has been followed by many similar

analyses to improve how the IGM opacity is quantified (Pentericci et al. 2002, Fan et al. 2006b, Becker et al. 2007, Bosman et al. 2018, Eilers et al. 2018, Yang et al. 2020a).

The simplest absorption indicator from a conceptual standpoint is the Ly $\alpha$  opacity,  $\tau = -\ln(I/I_0)$ , where  $I_0$  represents an estimate of the unabsorbed continuum flux level. Deeper spectra of SDSS J1030+0524 and many subsequently discovered objects consistently uncover similar spans of total absorption in Ly $\alpha$  resonance line at  $z > 6$ , implying a large lower bound on  $\tau$  limited only by the S/N ratio of the spectral data. This highlights an important challenge in such measurements: The physical information is contained in measuring flux that is not seen. The logarithmic nature of optical depth means that even in spectra with S/N  $\sim 100$ , one can measure limits of  $\tau \gtrsim 4$  (per pixel) at best, and the zero points can be affected by systematic errors in data reduction, including accurate subtraction night sky emission and correction for telluric absorption. Comparison of observations of the same quasars observed with different instruments and reduced with different pipelines indicate discrepancies at the 1–2% flux level, for a mean transmitted flux of 0.5–1.0% at  $z \sim 6$  (McGreer et al. 2011, Eilers et al. 2018).

Additional dynamic range can often be achieved by observing Ly $\beta$  or higher-order transitions from the Lyman series. These have progressively decreasing oscillator strengths and require correspondingly larger H $\text{I}$  column to saturate, allowing access to larger values of  $\tau$ . This advantage is offset by complications arising from unknown blending with Ly $\alpha$  forest absorption at lower redshift and uncertainty in extrapolating the intrinsic quasar continuum from Ly $\alpha$  to Ly $\beta$ .

Measurements of the Ly $\alpha$  opacity are always smoothed to suppress noise and minimize the effect of differing spectral dispersion and resolution among instruments used in the observations. Following Fan et al. (2006b), most early studies have used observationally motivated redshift bins of  $\Delta z = 0.15$  for ease of comparison, defining the effective optical depth  $\tau_{\text{eff}} = -\ln \langle F \rangle$  over the smoothing interval. More recent studies advocate for a physically motivated bin size of 50 cMpc, because a constant redshift interval evolves by  $\sim 40\%$  in comoving length over  $5 < z < 7$ , where such measurements are made (Becker et al. 2015, Eilers et al. 2018). The two values ( $\Delta z = 0.15$  and 50 cMpc) are comparable at  $z \sim 7$ . **Figure 13a** presents a recent summary of Ly $\alpha$  optical depth measurements.

Average  $\tau$  measurements are simply the first moment of an underlying optical depth distribution, which contains richer information and has therefore been measured extensively and presented as a cumulative distribution function (CDF) of optical depth. Evolution of the CDF is characterized by three phases, again reflecting the logarithmic nature of the measurements. At  $z \sim 5.0$ – $5.3$ , the distribution is fairly narrow and centered around  $\tau \sim 2$ , corresponding to a Ly $\alpha$  forest with significant ( $\sim 90\%$ ) absorption at line resonance, but not yet fully saturated. At  $5.5 < z < 6.0$ , the CDF widens to span  $2 < \tau < 6$ , as an increasing number of smoothed windows exhibit saturated absorption (i.e., zero transmitted flux or high  $\tau$ ), but many significant transmission/low neutral fraction windows remain. Above  $z > 6$ , it becomes increasingly rare to find unsaturated windows with  $\tau < 4$ , and the distribution once again narrows because spectral S/N renders the  $\tau > 6$  regime inaccessible.

Several groups have explored alternative ionization metrics that use counts of transmission spikes in the Ly $\alpha$  forest, motivated by the many challenges of measuring optical depths in realistic, heavily absorbed data. Garaldi et al. (2019) constructed distribution functions  $d^2N/dLdz$ , capturing the density of spikes per comoving megaparsec and unit redshift, above a threshold line flux. These can be counted in spectra of varying resolution and S/N using similar techniques, as are used for blind searches for metal absorption lines in quasar spectra. Their analysis indicates that, after accounting for instrumental broadening and noise that suppress the spike count in realistic observed  $5 < z < 6$  spectra by an order of magnitude, the observed spike counts are roughly

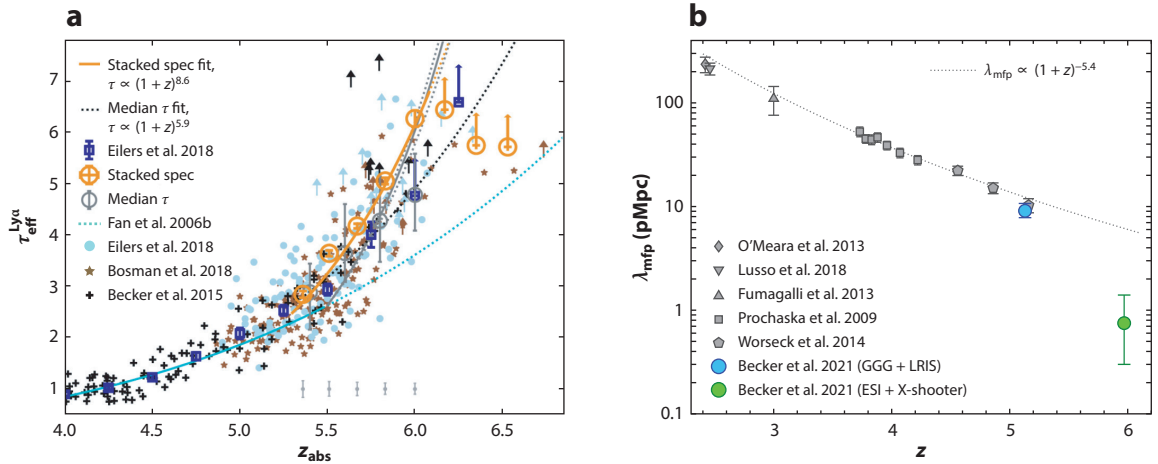


**Figure 13**

(a) Evolution of the Ly $\alpha$  optical depth with redshift based on spectroscopy of large quasar samples. The optical depth increases smoothly toward high redshift at  $z < 5.5$ , then appears to evolve more strongly, with the emergence of complete Gunn–Peterson absorption troughs (upper limits). Panel adapted from Yang et al. (2020a). (b) Evolution of the mean free path for ionizing photons, illustrating the rapid evolution approaching  $z \sim 6$ . Panel adapted from Becker et al. (2021).

consistent with their self-consistent simulations of the postreionization IGM transmission. In the simulation boxes, transmission spikes arise from regions that are underdense in hydrogen and galaxies, but overionized relative to expectations from equilibrium with the average radiation field, likely because of proximity to local ionizing sources.

At  $z > 6$  one expects transmission spikes to be exceedingly rare, so the detection even of single spikes implies the existence of early ionized cavities. Searches for spikes in high-redshift spectra have yielded several detections at  $6 < z < 6.3$  that provide upper bounds on the local optical depth, complementing the lower bounds derived from measurements of saturated spectral regions (e.g., Yang et al. 2020a).

A very different way to conceptualize reionization is as a rapid increase in the mean free path (mfp) of ionizing photons. Although this is physically equivalent to an increase in the volume-averaged ionization fraction, this alternative framing allows a different analysis approach that does not require high-S/N measurements of localized pixels or spikes. Instead, samples of quasar spectra are stacked after shifting into the rest frame. Then a low-dimensional parametric model is fit to the shape of the stacked spectrum below the Lyman limit at  $912 \text{ \AA}$ , corresponding to a probabilistic flight length of ionizing photons traveling from the quasar toward Earth. This model was originally developed at lower redshift to study the evolution of the ionizing background far from the background quasar. At high redshift, additional complexity must be added to the model to account for local ionization effects near the quasar, because the mfp can approach the length scale of proximity zones of enhanced ionization around the quasar.

**Figure 13b** presents the measurements of IGM mfp using the most recent stacking analyses from Becker et al. (2021). It suggests a rapid change in the mfp from 8–10 pMpc at  $z = 5.1$  to 0.75–1.5 pMpc at  $z = 6.0$  (the range reflects potential fluctuations from cosmic variance/sample size and also uncertainty in the correlation between the H $\text{I}$  opacity and ionization rate). This evolution is much stronger than would be inferred from extrapolation of the evolving mfp at lower redshifts, as one would expect in the late stages of a phase transition like reionization.

**6.2.3. Dark gaps and the late stages of reionization.** The inverse phenomenon of Ly $\alpha$  transmission spikes—which trace the first environments to complete reionization at  $z > 6$ —is that several quasar sightlines exhibit long, dark gaps of zero flux at  $z < 6$ . These gaps are now understood to represent residual islands of neutral matter during late-stage reionization. As first explored by Becker et al. (2015) after the discovery of a  $> 110$ -cMpc dark span toward the quasar ULAS J0148+0600, measurements of gap length have the advantage of being relatively insensitive to the details of estimating the quasar continuum or absolute flux levels. Long gaps are not seen at  $z \sim 5$ , and indeed recent work by Zhu et al. (2021) finds that 90% of quasar spectra at  $z \sim 6$  have a dark gap of 30 cMpc or longer, but only 15% do at  $z = 5.6$ .

Gap statistics have generated significant theoretical interest, as they appear to be inconsistent with numerical models approximating the ionizing UV background field as spatially uniform at  $z = 5.5 - 6$  (Zhu et al. 2021). Various mechanisms have been proposed to explain the phenomenon, including (a) upward fluctuations in gas density (yielding a higher recombination rate and neutral fraction), (b) downward fluctuations in the ionizing radiation background, or (c) upward fluctuations in galaxy number density, leading to lower-than-average temperatures (D’Aloisio et al. 2015). The latter scenario is less intuitive, arising from a subtle effect in which regions of high galaxy density reionize early and then have more time to cool off from the associated photoionization heating. These first areas to reionize have a lower temperature than surrounding regions that reionize later and have not yet cooled. Because the H I recombination rate scales as  $T^{-0.7}$ , cooler regions that reionized earliest would have higher neutral fraction and the opacity characteristic of dark gaps.

This yields a testable prediction to distinguish between dark gap models arising from UV background and temperature-driven fluctuations (Davies et al. 2018a). Galaxy surveys along sightlines with gaps should see an enhancement in galaxy counts relative to the field if the gaps arise in cool regions that reionized early; conversely there should be a galaxy deficit if the gaps arise in islands of enhanced neutral fraction and/or low-ionizing radiation background (two effects that are not straightforward to distinguish). Christenson et al. (2021), Becker et al. (2018), and Ishimoto et al. (2022) conducted narrowband Ly $\alpha$  surveys in fields centered on well-known dark gaps to test this prediction and found an underdensity of LAEs within  $20b^{-1}$  Mpc of the quasar sightline, favoring a scenario in which the dark gaps represent residual neutral islands persisting in the late-reionization Universe. Spectroscopic galaxy surveys have been difficult and expensive at these redshifts from the ground, but early observations with JWST indicate that prospects are very favorable for correlating galaxies observed in rest-frame optical emission lines with the IGM Ly $\alpha$  opacity.

Overall, a consistent picture emerges from a suite of distinct IGM observations using quasar spectra, including (a) the average Ly $\alpha$  optical depth and its CDF, (b) dark gaps, (c) transmission spikes, and (d) the mfp. The first three of these four measurements result from on-resonance Ly $\alpha$  absorption, and the fourth measures the Lyman continuum, making them all most useful toward the tail end of reionization at  $5.5 < z < 6.3$ , when the volume-averaged neutral fraction is  $\sim 10^{-4}$ , but with significant spatial fluctuations. Taken together there is evidence that large neutral islands persisted well after  $z \sim 6$ , possibly in regions of low galaxy density and ambient ionizing radiation. During this time, there was a tenfold increase in the mfp for ionizing photons, eventually reaching cosmological length scales of 10 pMpc or more. The earliest regions to fully reionize can be traced by transmission spikes at  $z \sim 6.3$  and are likely to reside in regions of low gas density that happen by chance to fall near a source of ionizing radiation.

**6.2.4. Thermal signatures.** Ionizing sources emit a spectrum of radiation including photons with energy above the  $E > 13.6$  eV hydrogen ionization potential. The excess photon energy heats the postreionization IGM, which subsequently cools over time due to adiabatic cosmic

expansion. Such heating and cooling is clearly seen during the reionization of  $\text{HeII}$  at lower redshift (Walther et al. 2019); an even larger effect should be present for hydrogen reionization. Unfortunately unlike  $\text{HeII}$ , it is not possible to measure heating from hydrogen reionization in real time, because Gunn–Peterson absorption fully blankets the signal at the redshifts of interest. Nevertheless, the temperature of the IGM at lower redshift—after reionization is complete—still encodes information about the past thermal history.

High-resolution quasar spectra are excellent thermometers of the IGM, because thermal gas motions projected along the line of sight smooth or broaden absorption features. At lower redshifts, where individual unblended lines can be resolved in the  $\text{Ly}\alpha$  forest, temperature maps directly to line profile width through the Voigt profile parameter  $b = \sqrt{2kT/m_{\text{ion}}}$ , though this signature is convolved with similar broadening from turbulence and bulk gas motions.

At  $z > 4.5$  it becomes impossible to distinguish individual lines, so the IGM’s temperature signal must be measured statistically. Effectively, thermal effects impose a low-pass filter on the power spectrum, smoothing out small-scale structure in the pattern of  $\text{Ly}\alpha$  transmission. The band limit of this filter is partly a proxy for the instantaneous temperature, but it also retains a memory of past heating, which is partly manifested through a pressure (i.e., Jeans) broadening beyond the normal Hubble flow. These effects are calibrated by statistical comparison to cosmological simulations.

The simulations are generally run on a grid that varies the mean temperature of the IGM at specified redshifts  $T_0(z)$ , the slope  $\gamma$  of the IGM’s temperature–density relation  $T(\Delta) = T_0\Delta^\gamma$ , and the thermal energy injected into the IGM during reionization  $u_0$ , in units of electronvolts per baryon. Synthetic spectra are drawn directly from simulation volumes and run through identical analysis software as the true quasar spectra to ascertain which combination of  $T_0$ ,  $\gamma$ , and  $u_0$  produce 1D flux power spectra most closely matching observed values.

Using these methods, Boera et al. (2019) find IGM temperatures of  $T_0 = 7,000\text{--}8,000$  K at  $4.2 < z < 5.0$ , which is where the effective optical depth of the forest is  $1 < \tau_{\text{eff}} < 2$ , making the method most sensitive. Toward higher redshifts where Gunn–Peterson saturation begins to manifest, thermal measurements become increasingly challenging. However, recent constraints have been extracted by fitting the widths of emission line spikes, indicating slightly higher  $T_0 = 10,000\text{--}12,000$  K at earlier times  $z = 5.3\text{--}5.9$  as expected according to the paradigm of heating and adiabatic cooling (Gaikwad et al. 2020).

The simulations can also explore a range of different reionization histories to see which parameters best reproduce the postreionization power spectrum. Toy models of instantaneous reionization provide joint constraints on the redshift of thermal injection and its amplitude, favoring  $z \sim 8\text{--}10$  as the reionization redshift, and peak postreionization temperatures of  $T = 10,000\text{--}20,000$  K depending on the choice of ionizing background spectrum. Temperature constraints on the reionization history are limited because the IGM tends to rapidly cool back to its ionization equilibrium temperature, washing out the signal from the initial thermal impulse. As mentioned above, the rapid thermal broadening is accompanied by a pressure broadening that also manifests in the power spectrum and is somewhat longer lived. It is not possible to fully disentangle pressure and temperature smoothing effects from line-of-sight measurements. However, measurements made using pairs of adjacent quasar sightlines can break this degeneracy, because they only measure smoothing on a transverse spatial scale by construction (Rorai et al. 2017).

In summary, though the power spectrum and thermal history cannot provide precision constraints on the timing of hydrogen reionization, they support a general result that by  $z \sim 5$ , the initial thermal energy injected into the IGM has already cooled substantially, by perhaps a factor of 2–3. This sets a lower bound on the elapsed time between the period of thermal energy injection and  $z \sim 4\text{--}5$ , where the measurements are made. This in turn implies that the peak heating

associated with reionization occurred at  $7 < z < 10$ , which is broadly consistent with CMB results reported by the Planck Collab. et al. (2020).

### 6.3. Neutral Hydrogen Absorption in the Quasar Environment

Each quasar spectrum offers the opportunity to study radiative feedback in the neighborhood of a luminous source of ionizing photons: the background object itself. At  $2 < z < 3$ , a clear deficit is seen in the density of Ly $\alpha$  forest lines as a quasar’s emission redshift is approached (Murdoch et al. 1986, Bajtlik et al. 1988). For these lower redshifts, where the ambient IGM is clearly optically thin, the so-called proximity effect reflects a local enhancement of ionization in an already highly ionized medium and can be used to derive estimates of the quasar’s ionizing flux over the metagalactic background.

This measurement becomes increasingly valuable at high redshift, because the diffuse IGM is optically thick to Ly $\alpha$  absorption. However, the observational manifestation of interactions between quasar radiation and the IGM differs according to whether the surrounding medium has already undergone reionization—in which case one observes a proximity zone—or the surrounding medium still has a high neutral fraction—in which case one observes a damping wing. Both phenomena are now well established; in the sections below, we aim to clarify the distinction between the two, reconcile some differences in definitions, and clarify at which redshifts each one is most powerful.

#### 6.3.1. Proximity zones and the effects of quasar radiation on recently reionized matter.

At  $z_{\text{em}} \sim 5.9\text{--}6.5$ , on-resonance (Gunn–Peterson) Ly $\alpha$  has sufficient column density to fully absorb a quasar’s continuum. However, the volume-averaged neutral fraction is only  $\sim 10^{-4}$  during late-stage reionization, so a quasar’s local ionization boost can suppress the local Ly $\alpha$  opacity to optically thin values  $\tau < 1$ , allowing some flux to transmit at wavelengths just blueward of the Ly $\alpha$  emission line. In exact analogy to the classic proximity effect at lower redshift, these proximity zones at  $z \sim 6$  trace a local ionization enhancement in an already ionized medium. They should not be confused with Strömberg spheres, because the outside medium has a neutral fraction  $X_{\text{HI}} \ll 1$ .

The size of a quasar’s proximity zone depends on its ionizing photon luminosity, its lifetime (i.e., how long it has been shining in a UV-bright phase), and the density and ionization of the surrounding medium. By convention, observers have defined the proximity zone as the total path from  $z_{\text{em}}$  to where a quasar’s spectral flux density remains  $>10\%$  of the continuum level, after smoothing by a boxcar window of width  $20 \text{ \AA}$  (Fan et al. 2006b). Although observationally convenient and consistent, this definition is not motivated by any physical transition or process. It is loosely related to a radius of enhanced ionizing background, but at a 10% flux threshold the enhancement is still very strong—the quasar contribution exceeds the ambient field by an order of magnitude (Eilers et al. 2017). In select cases, Ly $\alpha$  and Ly $\beta$  measurements may be compared in order to improve dynamic range, in analogous fashion to IGM measurements (Mesinger & Haiman 2004), and this probes the sharpness of the boundary of enhanced ionization fraction.

Uniformly selected samples have yielded typical proximity zone sizes of 2–6 pMpc, with a strong (expected) dependence on quasar luminosity and comparatively weak dependence on redshift in the range of  $6.0 < z < 6.5$  (Eilers et al. 2017, 2020). Intriguingly, after adjusting proximity zone sizes to normalize out the effect of quasar luminosity, Eilers et al. (2017) found that  $\sim 10\%$  of their sample had exceptionally small proximity zones. They argued that the most likely explanation is that we are observing these quasars before their radiation field has reached ionization equilibrium with the surrounding IGM; i.e., their current UV-luminous period is  $t < 100,000$  years old, with extreme objects even at  $t < 10,000$  years (Eilers et al. 2021). Stacking analysis of multiple quasars’ near zones indicates that the median quasar lifetime is larger by approximately an

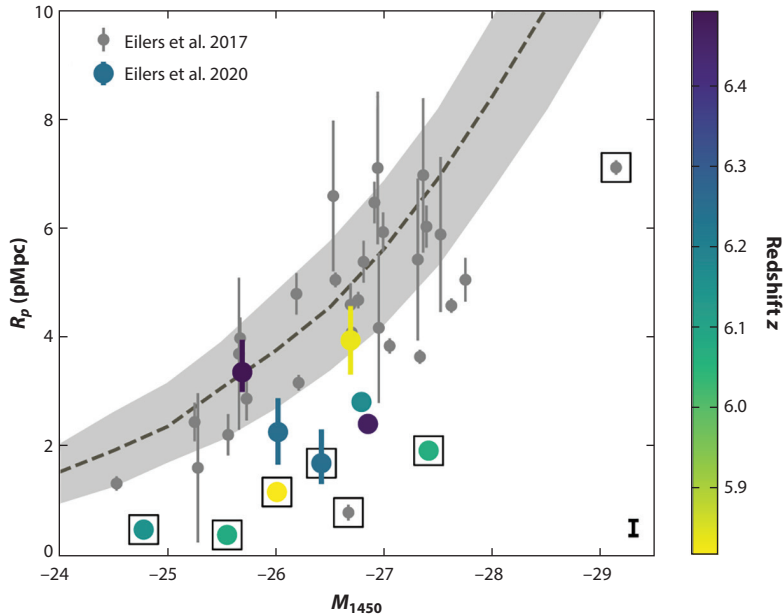


**Figure 14**

The size distribution of proximity zones at  $5.9 < z < 6.4$  (Eilers et al. 2020), versus their host quasar’s absolute magnitude or luminosity. Shaded region shows expectations from a numerical simulation assuming the quasar has reached ionization equilibrium with its surroundings. This matches a representative sample of quasars at these redshifts (*gray points*), but separate samples have been identified with small proximity zones that have been interpreted as evidence of recent UV accretion episodes. Quasars with extremely small proximity zones are indicated by the black boxes.

order of magnitude (Morey et al. 2021). **Figure 14** presents a summary of proximity zone size measurements, along with young quasars identified through this type of measurement.

If this interpretation is correct, then proximity zone size distributions can be used to constrain the UV duty cycle of early quasars. The size is sensitive only to the age of the most recent or current UV-bright episode, which is not necessarily the first in its history. However, the growth timescale problem for building SMBHs at  $z > 6$  is well known (see Section 4, and Volonteri 2010), and this challenge is only exacerbated for any accretion duty cycle below unity. It may be that the usual assumed correspondence between robust accretion and UV-bright episodes may need revision, and significant BH growth can occur during a dusty, obscured phase.

**6.3.2. Intergalactic medium damping wings.** As one penetrates deeper into the reionization epoch near  $z \sim 7$ , the ambient neutral fraction increases and the corresponding length scale of proximity zones becomes smaller. When the neutral fraction approaches 1–10%, the effects of off-resonance Ly $\alpha$  damping wings become significant (Miralda-Escudé 1998). Details of this process have been reviewed by Mortlock (2016). Briefly, high column densities of neutral hydrogen in the nearby foreground of a quasar lead to a nonnegligible probability that a photon emitted redward of Ly $\alpha$  in the quasar’s rest frame will still be absorbed by neutral intergalactic matter en route to Earth. This last fact is critical—in the far-foreground Ly $\alpha$  forest region there is an unresolvable degeneracy at any wavelength between off-resonance damping wing absorption from neutral gas and on-resonance absorption from ionized gas at a different redshift. In contrast, absorption redward of the Ly $\alpha$  emission line can only come from off-resonance interactions.

The IGM damping signature is expected around quasars meeting two conditions: They have recently turned on, and they are embedded in an IGM with high global neutral fraction. In contrast to  $z \sim 6$  proximity zones that have already been preionized by surrounding galaxies, the  $z \sim 7$  quasars with damping wings are driving true ionization fronts into the surrounding IGM with a size that increases with the quasar’s active phase lifetime and ionizing photon flux and decreases with larger overdensity.

The strength of a damping wing is most sensitive to the neutral fraction of matter just outside the quasar’s ionization front. Gas closer to the quasar is inside the ionization front, so its neutral fraction is too low to produce off-resonance Ly $\alpha$  absorption wings. Gas that is far outside the ionization front can produce off-resonance absorption, but its line-of-sight velocity offset is too large for the off-resonance wing to produce appreciable optical depth redward of Ly $\alpha$  emission.

Damping wing measurements are significantly affected by systematic uncertainties in modeling the detailed shape of quasars’ intrinsic Ly $\alpha$  profile. Different groups have tackled this challenge using training sets of low-redshift SDSS or HST/COS (Cosmic Origins Spectrograph) spectra from which the Ly $\alpha$  emission profile and unabsorbed continuum can be estimated more reliably. The objective is to predict the unabsorbed Ly $\alpha$  emission line shape and forest continuum (and associated uncertainties) using pixels to the red of the quasar’s Ly $\alpha$  emission line.

Multiple groups have used principal component analysis (Mortlock et al. 2011, Davies et al. 2018c), machine/deep learning models (Liu & Bordoloi 2021), neural networks (Ďurovčiková et al. 2020), covariance matrices (Greig et al. 2017, 2022), stacking of nearest-neighbor observed spectra (Simcoe et al. 2012, Bosman & Becker 2015, Bosman et al. 2021), or other hybrid approaches to train and validate continuum+Ly $\alpha$  software on lower-redshift quasars. Most methods also calculate some envelope of formal uncertainty on the continuum estimate before applying them to  $z \sim 7$  quasar spectra. When comparing different reconstruction techniques in the Ly $\alpha$ /Ly $\beta$  forest region and around the Ly $\alpha$  emission line, the difference between continuum models for the same object using different codes often exceeds expectations from their formal error estimates, indicating the presence of residual systematics. It has therefore been important to test observations of the same objects taken using different instruments and analysis software to build confidence in the fundamental conclusion about damping wing strengths and the neutral fraction. **Figure 15** illustrates some of the different techniques used for predicting the quasar intrinsic spectrum in the damping wing region of a quasar at  $z = 7.0$ .

Although it is impossible to know if any particular continuum realization is “correct,” a consensus is indeed emerging that certain specific objects—most notably ULAS J1342+0928 ( $z = 7.54$ ; Bañados et al. 2018), DESJ0252–0503 ( $z = 7.00$ ; Wang et al. 2020), J1007+2115 ( $z = 7.51$ ; Yang et al. 2020b) and ULAS J1120+0641 ( $z = 7.09$ ; Mortlock et al. 2011)—show strong evidence for IGM damping wings for all continuum models explored in the literature. Various analyses derive slightly different IGM neutral fractions for the same objects on account of modeling differences (Bolton et al. 2011; Davies et al. 2018b; Greig et al. 2019, 2022). But a robust result remains that 67% of known quasars at  $z > 7$  have (a) negligible proximity zone sizes, and (b) flux measurements at wavelengths slightly redder than the Ly $\alpha$  emission line that fall below all continuum reconstructions based on low-redshift quasars. This combination of small proximity zone and damping wing has not been measured in a single quasar at  $z < 7$ , despite the much larger sample sizes available for testing.

Because most of the damping wing is generated just outside the ionized bubble, there is a risk that the same signature could arise from chance alignment of a classical DLA absorber (i.e., from the ISM of a bound protogalaxy) near the quasar in an otherwise ionized IGM (Section 6.5). Indeed there are examples of such proximate DLAs in the literature, including several at  $z > 6$ . The a priori odds of such a chance alignment are small but were considered carefully in studies

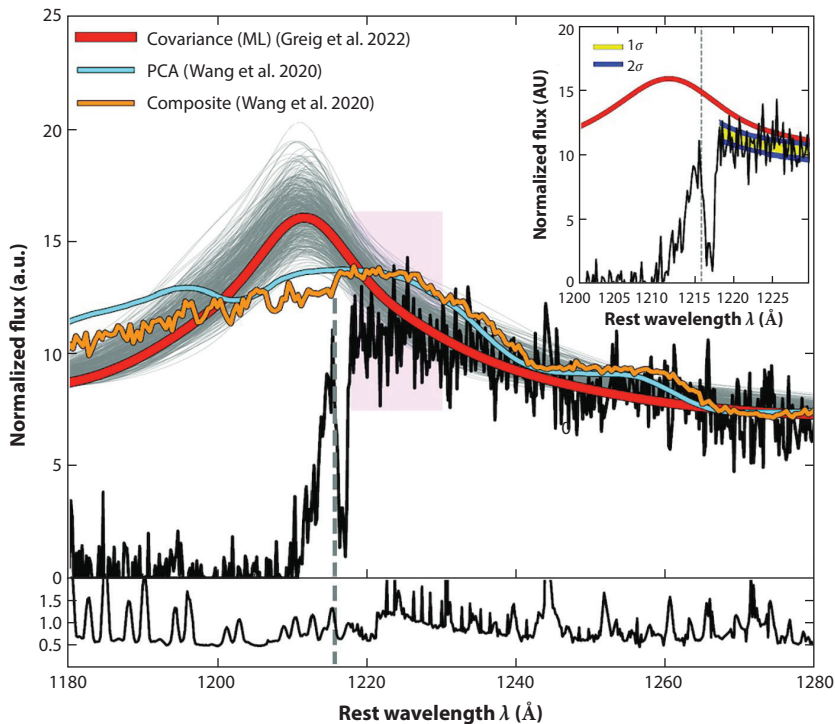


**Figure 15**

Damping wing measurements for J0252–0503 ( $z = 7.00$ ). Quasar spectrum is shown by a black curve, and three continuum models are shown for the damping wing analysis. The quasar’s systemic redshift is shown with a vertical dashed line. Figure adapted from Greig et al. (2022). Abbreviations: ML, machine learning; PCA, principle component analysis.

of the first damping wing (Simcoe et al. 2012). There are two arguments now suggesting that this phenomenon is not affecting IGM measurements at  $z > 7$ . First, none of the four sightlines listed above exhibit heavy element absorption at the redshift of the putative DLA, to very sensitive limits. Second, the presence of damping wings in multiple new  $z > 7$  discoveries points to a global phenomenon, as the joint probability of seeing proximate DLAs in all of these becomes lower still. With very high-S/N data it is in principle possible to distinguish between DLA absorption from the condensed CGM/ISM of a protogalaxy and an extended patch of neutral but gravitationally unbound IGM using the damping profile alone. However, no studies at present have claimed such a detection.

A final unknowable factor in damping wing analysis is the spatial distribution of gas density and accompanying fluctuations in ionization inside and outside the proximity zone. Early papers used analytic models based on distribution functions of overdensity and assumed that the gas was in ionization equilibrium with a uniform background radiation field (Mortlock et al. 2011, Simcoe et al. 2012). Later and more sophisticated treatments have drawn distributions of sightlines from cosmological simulations to capture the line-of-sight variations in density and ionization (Greig et al. 2019). Large simulation boxes are required for this method, to identify the rare, high-mass halos in which early quasars are thought to reside. Many sightlines are constructed that terminate by design at the high-mass halo, to generate many realizations of the damping wing for different viewing orientations.

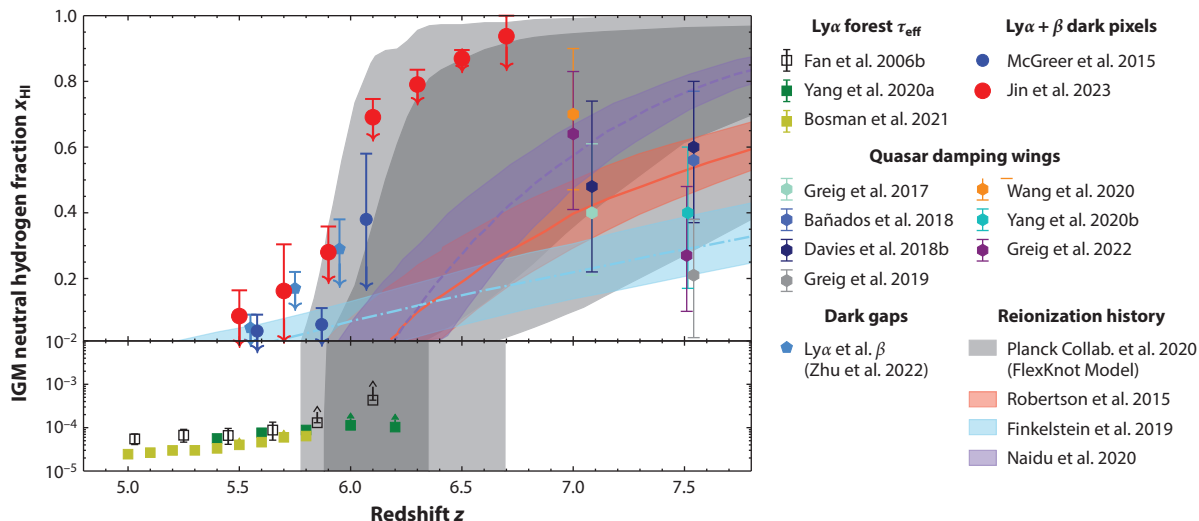


**Figure 16**

Summary of quasar absorption constraints on the reionization history (all data points). The dark (light) gray-shaded region is the  $1\sigma$  ( $2\sigma$ ) constraint from the cosmic microwave background (Planck Collab. et al. 2020). The red, blue, and purple shaded regions display the  $1\sigma$  reionization histories from the Robertson et al. (2015), Finkelstein et al. (2019), and Naidu et al. (2020) models, respectively. See Jin et al. (2023), and references therein for more details. Figure adapted from Jin et al. (2023). Abbreviation: IGM, intergalactic medium.

In summary, among all quasar absorption methods, IGM damping wings yield the only two-sided constraint on  $X_{\text{HI}}$  at  $z > 5.7$  and are therefore one of our most important probes of reionization history. They are nevertheless subject to substantial, and probably unresolvable, systematic uncertainties concerning quasar continuum shape and details of the density and ionization fields around each quasar. Nevertheless, a tentative consensus has emerged that for the majority of objects yet discovered at  $7.0 < z < 7.5$ , the near-zone size and damped absorption rule out models with global ionization fractions  $X_{\text{HI}} < 1\%$  or  $X_{\text{HI}} \approx 100\%$ , instead favoring values from 20–80%. Adding more objects will potentially increase confidence in the result but may not reduce its fractional uncertainty to better than  $\pm 40\%$ , because the uncertainty envelope is dominated by model assumptions and is therefore not random.

Still this result is extremely significant because any measurement placing  $X_{\text{HI}} \sim 50\%$  (or at a similar order of magnitude) represents a working definition of the reionization midpoint. **Figure 16** summarizes the various reionization constraints from different quasar absorption observations, compared with both constraints from the measurements of CMB polarization (Robertson et al. 2015) and a number of empirical reionization history models. Optical depth measurements provide one-sided lower limits on  $X_{\text{HI}}$  at  $z < 6.3$ , transmission spikes provide one-sided upper limits at  $5.5 < z < 6.5$ , and damping wings provide two-sided constraints with large errors at  $7 < z < 7.5$ . This combination of limits and measurements permits models with a range of reionization histories with midpoints centered anywhere from  $6.5 < z < 8.0$ . Future 21-cm experiments will potentially measure these values with more precision and accuracy; these quasar constraints will help such experiments optimize their redshift window. Still, when expressed in terms of lookback time rather than redshift, quasar absorption constraints correspond to a 1–2% measurement of the timing of reionization, to  $94.5_{-0.5}^{+0.9}\%$  lookback, or  $760_{-120}^{+80}$  Myr after the Big Bang.

## 6.4. Heavy Element Enrichment of Intervening Quasar Absorbers

The radiative feedback that drove reionization was accompanied by chemical feedback that can also be observed in the spectra of high-redshift quasars. At  $z > 6$ , large samples of high-resolution quasar spectra taken with VLT/XSHOOTER, GMT/FIRE (Folded-port InfraRed Echellette), Keck/NIRES (Near-Infrared Echellette Spectrometer), and the Gemini Observatory’s GNIRS (Gemini North Near-IR Spectrograph) have revealed foreground heavy element absorption lines redward of Ly $\alpha$  where the quasar’s continuum can be easily modeled. Because H $\alpha$  is saturated in the Ly $\alpha$  forest at  $z > 6$ , metal absorption lines provide the only accessible information about diffuse gas at these epochs.

Absorption strength in these papers is sometimes reported as column density  $N_{\text{ion}}$  and other times as a rest-frame equivalent width  $W_r$ . The IR spectrographs listed above have intrinsic resolutions of  $\Delta v \sim 50 \text{ km s}^{-1}$  or coarser, which is insufficient to resolve the fine 5–10  $\text{km s}^{-1}$  velocity structure seen in metal-line absorbers at lower redshift. Equivalent width measurements are therefore conservative and will be consistently measured across all spectrographs. Column densities are easier to interpret physically but must be approached with care, accounting for the possibility of unresolved saturation in the line core or blending of unresolved components. The detection sensitivity of current spectrographs limits metal-line analyses to column densities characteristic of circumgalactic gas at lower redshift. Deeper spectra or statistical stacks will be needed to search for metals in the diffuse IGM.

Early studies of heavy element enrichment in the reionization epoch (Ryan-Weber et al. 2006, Simcoe 2006, Becker et al. 2009, Simcoe et al. 2011, D’Odorico et al. 2013) focused on the C $\text{IV}$  doublet, which is the most ubiquitous IGM metal line at lower redshifts and a tracer of highly ionized circumgalactic gas. At  $z > 5.5$ , C $\text{IV}$  shifts into the  $J$  band. Most surveys focus on a similar set of observables, including the comoving absorption density  $dN/dX$ <sup>1</sup>, and the equivalent width distribution  $d^2N/dXdW$ .

These surveys established that the frequency of C $\text{IV}$  absorbers decreases toward higher redshift, such that individual C $\text{IV}$  systems become rare at  $z > 6$ —most sightlines have no C $\text{IV}$  doublets in this range. For example, Codoreanu et al. (2018) surveyed deep spectra of four quasar sightlines, finding a four-fold decrease in comoving line density  $dN/dX$  between  $z = 4.8$  and  $z = 5.7$ , and zero detections above  $z > 6$ , which is consistent with earlier but smaller studies in the literature (Simcoe et al. 2011). There is very tentative evidence of a steepening in the column density distribution function (CDDF)  $f(N) = d^2N/dNdX$ , because of differential evolution of the strongest C $\text{IV}$  absorbers at high redshift. However, these analyses still utilize modest numbers of sightlines ( $< 10$ ), so shot noise and saturation become significant limitations at the high- $W_r$  end. There are now relatively large samples of high-quality spectra for  $z > 6.5$  quasars, which should lead to improved estimates of the CDDF and C $\text{IV}$  evolution in the near future.

Evolving enrichment levels are sometimes summarized in terms of the C $\text{IV}$  contribution to closure density  $\Omega_{\text{CIV}}$ , which is a mass-weighted integral of the CDDF. Like  $dN/dX$  or the normalization of  $f(N)$ ,  $\Omega_{\text{CIV}}$  declines toward higher redshift. Although it is convenient to express global metal enrichment in terms of this single number, the power-law slope  $f(N) \propto N^{-1.5}$  of the CDDF is shallower than  $\alpha = -2$ , implying that the integral  $\int Nf(N)dN$  diverges toward high column densities. The single strongest absorber in any sample therefore dominates the integral, meaning that by construction  $\Omega_{\text{CIV}}$  is affected by shot noise and pathlength searched.

---

<sup>1</sup>The quantity  $dX = dz\sqrt{\Omega_M(1+z)^3 + \Omega_\Lambda}$  is equivalent to a redshift path at  $z = 0$ , but accounts for pure cosmological evolution in the comoving radial line element. A population of absorbers with constant product  $n(z)\sigma$  of comoving space density  $n(z)$  and absorption cross section  $\sigma$  will have a constant  $dN/dX$  at all redshifts.

The disappearance of C<sub>IV</sub> at high redshift could be driven by either a decline in heavy element abundances or a change in ionization. If abundance evolution predominates, one might also expect to see a decline in the frequency of low-ionization species such as Mg<sub>II</sub>, O<sub>I</sub>, Si<sub>II</sub>, C<sub>II</sub>, or Fe<sub>II</sub>. However, there have been robust detections of all these low-ionization lines at  $z > 6$ , suggesting an important change in the ionization state of metal absorption line systems coincident with the reionization of intergalactic hydrogen.

The first detections of low-ionization metal absorption at  $z > 6$  focused on the O<sub>I</sub> 1302, C<sub>II</sub> 1334, and Si<sub>II</sub> 1260 lines, which have rest wavelengths only slightly to the red of Ly $\alpha$  and can therefore be detected in high-resolution optical (rather than IR) spectra (Becker et al. 2011). However, the small offset between these and Ly $\alpha$  also leaves a very short search path-length per sightline; if they are too far in the quasar’s foreground, these lines fall within the H<sub>I</sub> Gunn–Peterson trough and become impossible to detect.

With improved IR spectra it became possible to search systematically for low-ionization Mg<sub>II</sub> doublets at  $z > 6$ , albeit with complex selection windows caused by broadband atmospheric absorption between the *J/H* and *H/K* bands, discrete telluric absorption, and bright hydroxyl emission lines. After accounting for these effects, Mg<sub>II</sub> surveys find trends consistent with the other neutral ions—there is no clear evolution in the comoving line density  $dN/dX$  for systems with  $W_r > 0.3 \text{ \AA}$  (although if one restricts to very strong absorbers, there is a slight excess at  $z \sim 3$ ; Matejek & Simcoe 2012, Chen et al. 2017).

The statistical decrease in C<sub>IV</sub> frequency together with statistical nonevolution of low-ionization species requires that as reionization is approached, one should eventually find individual absorbers with C<sub>II</sub>, O<sub>I</sub>, Si<sub>II</sub>, and Mg<sub>II</sub> but no detection of a highly ionized C<sub>IV</sub> phase. This is indeed the case; in fact such low-ionization-only systems predominate at  $z > 6$ , composing over two-thirds of all metal-line absorbers (Cooper et al. 2019).

In sharp contrast, low-ionization-only absorbers are exceedingly rare at all redshifts  $z < 5.5$ , indicating a qualitative change in the CGM’s observable properties during the reionization epoch. At  $2 < z < 4$ , O<sub>I</sub>, C<sub>II</sub>, and Si<sub>II</sub> are much more rare than C<sub>IV</sub>; nearly every known low-ionization absorber is accompanied by stronger C<sub>IV</sub> and Si<sub>IV</sub> lines offset by  $< 100 \text{ km s}^{-1}$ , and there are many examples of C<sub>IV</sub> with no low-ionization lines (Cooper et al. 2019). Because absorption surveys are cross-section selected, the canonical interpretation is that ionized C<sub>IV</sub> traces a widespread low-density CGM, whereas O<sub>I</sub>, C<sub>II</sub>, and Si<sub>II</sub> trace cooled and condensed clumps in the ISM of a nearby galaxy or small, cold precipitates embedded in the warm ionized CGM (Stern et al. 2016). The evolution of the number density of heavy element absorption systems is summarized in **Figure 17**.

The observational disappearance of the ionized CGM implies that during this epoch in which galaxies are in early assembly, their circumgalactic gas has not yet been enriched to observable levels and/or the ambient radiation field is insufficient in intensity or hardness to maintain a high degree of ionization. Unfortunately, it is impossible to calculate abundances directly at  $z > 6$ , because H<sub>I</sub> column density measurement is prevented by the Gunn–Peterson trough. However, the number density of these low-ionization metal lines is similar to extrapolations of  $dN/dX$  for DLAs and sub-DLAs (Becker et al. 2019, Cooper et al. 2019) and is either flat or slightly increasing at earlier times. If one assumes H<sub>I</sub> column densities in this range ( $N_{\text{HI}} > 10^{19.8}$ ), the detected low-ionization lines are consistent with a metallicity of  $[C/H] \sim -2.3$ , in a warm neutral medium. If there exists a warm ionized medium of similar metallicity in pressure equilibrium with the warm neutral phase, it would be clearly detected in C<sub>IV</sub>. If the heavy elements seen in low-ionization lines are produced locally to that environment, this implies that those metals have not yet been mixed into the ionized CGM. Evidently the galactic environments traced by  $z > 6$  metal absorbers bear some resemblance to metal-poor DLAs at lower redshifts, but they are at an early and immature stage of chemical evolution and mixing.

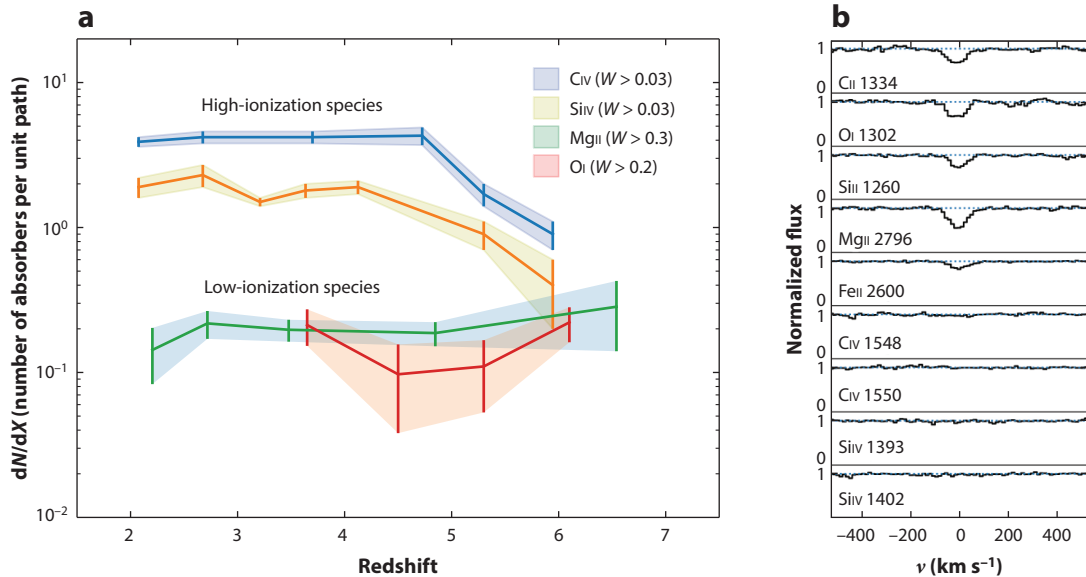


**Figure 17**

(a) Evolution in number density  $dN/dX$  of heavy element absorption systems, illustrating the different behavior between highly ionized species CIV and SiIV, which decline with increasing redshift, and low-ionization species MgII and OI, which do not decline. (b) A stack of  $z > 5.7$  absorbers selected individually by MgII detection, which shows other low-ionization lines but no evidence of CIV or SiIV.

## 6.5. Metal Absorption in the Vicinity of Quasi-Stellar Object Hosts

At all redshifts one can find a rare but important class of metal absorbers in the immediate foreground of their respective quasar hosts (Prochaska et al. 2008). These proximate DLAs (pDLAs) have a special importance, and four have been discovered at  $z > 6$ . They are the only discrete absorbers in the reionization epoch for which it is possible to constrain  $N_{\text{HI}}$  directly using the off-resonance wing. Because DLAs with  $N_{\text{HI}} > 10^{20.3} \text{ cm}^{-3}$  are self-shielded and largely neutral, the pDLAs therefore also permit direct measurement of heavy element abundances with no ionization correction needed.

The pDLAs are distinguished from IGM damping wings on the basis of coincident metal absorption. They are also found at lower redshift than the four  $z > 7$  IGM damping wing candidates—two pDLAs are at  $z \sim 6.3 - 6.4$  (Bañados et al. 2019b, Andika et al. 2022), one is at  $z \sim 6$  (Davies 2020), and one is at  $z = 5.93$ , which is 40 kpc from a galaxy detected with ALMA at coincident redshift (D’Odorico et al. 2018). At these redshifts, no other quasars have exhibited metal-free damping wings, and many observations of transmission spikes indicate that reionization is well underway (Yang et al. 2020a).

The pDLAs studied by Bañados et al. (2019b) and D’Odorico et al. (2018) have abundances near  $0.001 Z_{\odot}$ , which would place them among the most metal poor DLAs known at lower redshift (Cooke et al. 2011). Neither shows evidence for anomalies in relative abundances, as might be expected from a medium enriched with Population III supernova debris. High-ionization CIV and SiIV are not reported in either system, which is consistent with the discussion in the previous section about the disappearance of the high-ionization CGM phase. This has been cited as evidence that the pDLA originates outside of the quasar host, where the UV radiation field should be enhanced and an ionized medium would be expected.

The evidence so far suggests that pDLAs in the reionization epoch are representative of randomly intervening metal absorbers at similar redshift.

## 7. SUMMARY

Since the first discoveries of reionization-era quasars more than twenty years ago, tremendous progress has been made in extending the frontiers of quasar research deeper into the cosmic dawn, in characterizing and understanding these objects in the context of early SMBH growth and galaxy formation, and in using them as beacons to shed light on the evolution of the IGM and the history of cosmic reionization.

### SUMMARY POINTS

1. The current frontier of quasar research is at  $z \sim 7.6$ , with a large statistical sample assembled at redshifts up to 7. High-redshift quasar selection is a challenging data mining problem because of the rarity of the targets, the limited training sets, and the overwhelmingly large number of contaminant sources, both astrophysical and instrumental. We provide a database of the properties of all published quasars at  $z > 5.3$  as a **Supplemental Database** that accompanies this review.
2. The rapid evolution of the quasar luminosity function has been well established. However, the exact shape of the luminosity function is still uncertain, both at the high-luminosity end due to small number statistics and at the low-luminosity end due to limitations of deep surveys. In sharp contrast, early quasars “look” almost identical to their low-redshift counterparts in spectral properties. Even the earliest known quasars have a well-established AGN structure.
3. There are more than 100  $z \gtrsim 6$  quasars with robust black hole (BH) mass measurements. Their masses range from  $\sim 4 \times 10^7 M_\odot$  to  $\sim 10^{10} M_\odot$ . The BHs are growing at high Eddington ratios ( $\lambda_{\text{Eff, median}} = 0.79$  and  $\lambda_{\text{Eff, mean}} = 0.92$ ), with mild evidence of an increase of the accretion rate for  $z \gtrsim 6.5$  quasars in comparison to luminosity-matched quasar samples at lower redshifts.
4. The UV stellar light in  $z \sim 6$  quasar hosts remains undetected, whereas (sub)millimeter observations have revealed the existence of copious amounts of gas and cold dust in many of these galaxies. Quasar hosts are massive, star-forming galaxies showing diverse morphology and kinematics; their average dynamical mass appears lower than that based on the local scaling relation between BH and galaxy masses.
5. Ly $\alpha$  absorption in quasars’ foreground IGM provides many of the most stringent constraints on the history of reionization, though the details of the observations vary with redshift. Toward the end of reionization at  $z < 6$ , counts of transmission spikes, dark gaps, and pixel optical depths indicate that the Universe is mostly ionized but may harbor substantial islands of neutral matter as late as  $z \sim 5.3$ . At  $z > 7$ , four quasars have been discovered with prominent, metal-free damping wings that are thought to represent off-resonance absorption from an IGM with a neutral fraction of  $> 10\%$  and possibly as high as 80%.
6. Heavy element absorption is seen in quasar spectra well into the EoR, tracing chemical feedback from stars whose radiation is also transforming the global ionization balance. It appears that these absorbers are high-redshift, low-metallicity analogs of DLA absorbers

Supplemental Material >

observed at lower redshift. However, the highly ionized phase of the circumgalactic medium (CGM), seen universally in CIV at  $z < 6$ , abruptly vanishes in the EoR. This indicates that either the metals in the CGM are undergoing their own ionization transition or the ionized phase of the CGM has not yet been enriched with heavy elements at  $z > 6$ .

## FUTURE ISSUES

1. With the new facilities planned for the next decade, we expect the quasar redshift frontier to reach redshift 9–10, when the first generation of luminous quasars is forming. A key challenge will be the spectroscopic confirmation of these faint high-redshift sources.
2. Supermassive BH mass measurements using the H $\beta$  line with the *James Webb Space Telescope* (JWST) and gas-dynamical estimates with the Atacama Large Millimeter (submillimeter) Array (ALMA; and eventually the Next Generation Very Large Array) will provide more accurate measurements than what is currently possible. These results will be crucial for testing whether the current methods calibrated at low redshift (e.g., M<sub>HI</sub> single-epoch virial mass) still hold at the highest accessible redshifts. To measure the BH masses of the progenitors of the currently observed  $z = 6$ –7 quasar population, near-IR spectroscopic follow-up with the Extremely Large Telescopes (ELTs) will be key.
3. JWST will likely be able to finally reveal stellar light from  $z \gtrsim 6$  quasar hosts. ALMA will continue playing a critical role in understanding and characterizing the ISM of quasar host galaxies via multiline diagnostics.
4. New quasar samples uncovered by *Euclid* and the *Roman Space Telescope* and observed with JWST and ELTs should substantially improve confidence in  $z \geq 7$  measurements of IGM damping wings. They will allow studies even deeper into the past.
5. JWST already shows promise of being transformative for surveys of galaxies in fields in which high-redshift quasars have been used to constrain the IGM density field. This may open the possibility of studying cross-correlations among Ly $\alpha$ , metals, and galaxies.

## DISCLOSURE STATEMENT

The authors are not aware of any affiliations, memberships, funding, or financial holdings that might be perceived as affecting the objectivity of this review.

## ACKNOWLEDGMENTS

We dedicate this review to the memory of Professor Maarten Schmidt, who passed away in September 2022 at the age of 92. Maarten identified the first quasar, 3C273, in 1963. His groundbreaking work on quasars transformed our understanding of the distant Universe and inspired generations of quasar astronomers.

The authors thank Thomas Connor, Xiangyu Jin, Yana Khusanova, Chiara Mazzucchelli, Marcel Neeleman, Jan-Torge Schindler, Feige Wang, and Jinyi Yang for permission to use or adapt their figures; Irham Andika, Silvia Belladitta, Alessandro Caccianiga, Kuenley Chiu,

Emanuele Farina, Anniek Gloudemans, Linhua Jiang, Nobunari Kashikawa, George Khorunzhev, Yongjung Kim, Yoshiki Matsuoka, Israel Matute, Ian McGreer, Christopher Onken, Sophie Reed, Suhyun Shin, Daniel Stern, Bram Venemans, Jonah Wagenweld, Feige Wang, Lukas Wenzl, Chris Willott, Zhang-Liang Xie, and Jinyi Yang for providing their quasar spectra in digital form; Xiangyu Jin, Jan-Torge Schindler, Feige Wang, and Jinyi Yang for reformatting their published figures for this review; and George Becker, Roberto Decarli, Alyssa Drake, Zoltan Haiman, Yoshiki Matsuoka, Daniel Mortlock, Michael Strauss, Marianne Vestergaard, Feige Wang, Jinyi Yang, and the editor Joss Bland-Hawthorn for their thoughtful comments on an earlier draft of the review.

X.F. acknowledges support from US National Science Foundation grant AST 19-08284.

## LITERATURE CITED

- Aihara H, Armstrong R, Bickerton S, et al. 2018. *Publ. Astron. Soc. Jpn.* 70:58
- Ajiki M, Taniguchi Y, Murayama T, et al. 2006. *Publ. Astron. Soc. Jpn.* 58:499–502
- Andika IT, Jahnke K, Bañados E, et al. 2022. *Astron. J.* 163(6):251
- Andika IT, Jahnke K, Onoue M, et al. 2020. *Ap. J.* 903:34
- Bahk H, Woo JH, Park D. 2019. *Ap. J.* 875:50
- Bajtlik S, Duncan RC, Ostriker JP. 1988. *Ap. J.* 327:570–83
- Balmaverde B, Gilli R, Mignoli M, et al. 2017. *Astron. Astrophys.* 606:A23
- Bañados E, Mazzucchelli C, Momjian E, et al. 2021. *Ap. J.* 909:80
- Bañados E, Novak M, Neeleman M, et al. 2019a. *Ap. J. Lett.* 881:L23
- Bañados E, Rauch M, Decarli R, et al. 2019b. *Ap. J.* 885:59
- Bañados E, Venemans B, Walter F, et al. 2013. *Ap. J.* 773(2):178
- Bañados E, Venemans BP, Decarli R, et al. 2016. *Ap. J. Suppl. Ser.* 227:11
- Bañados E, Venemans BP, Mazzucchelli C, et al. 2018. *Nature* 553(7689):473–76
- Bañados E, Venemans BP, Morganson E, et al. 2015. *Ap. J.* 804(2):118
- Barnett R, Warren SJ, Cross NJG, et al. 2021. *MNRAS* 501(2):1663–76
- Barnett R, Warren SJ, Mortlock DJ, et al. 2019. *Astron. Astrophys.* 631:A85
- Barth AJ, Martini P, Nelson CH, Ho LC. 2003. *Ap. J. Lett.* 594(2):L95–98
- Becker GD, Bolton JS. 2013. *MNRAS* 436(2):1023–39
- Becker GD, Bolton JS, Madau P, et al. 2015. *MNRAS* 447(4):3402–19
- Becker GD, D’Aloisio A, Christenson HM, et al. 2021. *MNRAS* 508(2):1853–69
- Becker GD, Davies FB, Furlanetto SR, et al. 2018. *Ap. J.* 863:92
- Becker GD, Pettini M, Rafelski M, et al. 2019. *Ap. J.* 883(2):163
- Becker GD, Rauch M, Sargent WLW. 2007. *Ap. J.* 662:72–93
- Becker GD, Rauch M, Sargent WLW. 2009. *Ap. J.* 698(2):1010–19
- Becker GD, Sargent WLW, Rauch M, Calverley AP. 2011. *Ap. J.* 735(2):93
- Becker RH, Fan X, White RL, et al. 2001. *Astron. J.* 122(6):2850–57
- Beelen A, Cox P, Benford DJ, et al. 2006. *Ap. J.* 642(2):694–701
- Belladitta S, Moretti A, Caccianiga A, et al. 2020. *Astron. Astrophys.* 635:L7
- Bertoldi F, Carilli CL, Cox P, et al. 2003. *Astron. Astrophys.* 406:L55–58
- Bischetti M, Feruglio C, D’Odorico V, et al. 2022. *Nature* 605(7909):244–47
- Bischetti M, Maiolino R, Carniani S, et al. 2019. *Astron. Astrophys.* 630:A59
- Boera E, Becker GD, Bolton JS, Nasir F. 2019. *Ap. J.* 872:101
- Bolton JS, Haehnelt MG. 2007. *MNRAS* 374(2):493–514
- Bolton JS, Haehnelt MG, Warren SJ, et al. 2011. *MNRAS* 416:L70–74
- Bosman SEI, Becker GD. 2015. *MNRAS* 452(2):1105–11
- Bosman SEI, Ďurovčíková D, Davies FB, Eilers AC. 2021. *MNRAS* 503(2):2077–96
- Bosman SEI, Fan X, Jiang L, et al. 2018. *MNRAS* 479:1055–76
- Bosman SEI, Kakiichi K, Meyer RA, et al. 2020. *Ap. J.* 896:49
- Boyle BJ, Shanks T, Croom SM, et al. 2000. *MNRAS* 317(4):1014–22

- Brandt WN, Guainazzi M, Kaspi S, et al. 2001. *Astron. J.* 121(2):591–597
- Carilli CL, Shao Y. 2018. In *Monograph 7: Science with a Next Generation Very Large Array*, ed. E. Murphy, ngVLA Sci. Advis. Council. *ASP Conf. Ser.* 517:535–49. San Francisco: ASP
- Carilli CL, Walter F. 2013. *Annu. Rev. Astron. Astrophys.* 51:105–61
- Cen R, Haiman Z. 2000. *Ap. J. Lett.* 542(2):L75–78
- Chambers KC, Magnier EA, Metcalfe N, et al. 2016. arXiv:1612.05560
- Chen H, Eilers AC, Bosman SEI, et al. 2022. *Ap. J.* 931:29
- Chen H, Gnedin NY. 2021. *Ap. J.* 911:60
- Chen SFS, Simcoe RA, Torrey P, et al. 2017. *Ap. J.* 850(2):188
- Christenson HM, Becker GD, Furlanetto SR, et al. 2021. *Ap. J.* 923:87
- Cicone C, Maiolino R, Gallerani S, et al. 2015. *Astron. Astrophys.* 574:A14
- Codoreanu A, Ryan-Weber EV, Garca LÁ, et al. 2018. *MNRAS* 481(4):4940–59
- Cohn JH, Walsh JL, Boizelle BD, et al. 2021. *Ap. J.* 919(2):77
- Connor T, Bañados E, Stern D, et al. 2019. *Ap. J.* 887(2):171
- Connor T, Bañados E, Stern D, et al. 2021. *Ap. J.* 911(2):120
- Cooke R, Pettini M, Steidel CC, Rudie GC, Nissen PE. 2011. *MNRAS* 417(2):1534–58
- Cooper TJ, Simcoe RA, Cooksey KL, et al. 2019. *Ap. J.* 882(2):77
- Costa T, Arrigoni Battaia F, Farina EP, et al. 2022. *MNRAS* 517(2):1767–90
- Costa T, Sijacki D, Trenti M, Haehnelt MG. 2014. *MNRAS* 439(2):2146–74
- D’Aloisio A, McQuinn M, Trac H. 2015. *Ap. J. Lett.* 813(2):L38
- Davies FB. 2020. *MNRAS* 494(2):2937–47
- Davies FB, Becker GD, Furlanetto SR. 2018a. *Ap. J.* 860(2):155
- Davies FB, Hennawi JF, Bañados E, et al. 2018b. *Ap. J.* 864(2):142
- Davies FB, Hennawi JF, Bañados E, et al. 2018c. *Ap. J.* 864(2):143
- Davies FB, Hennawi JF, Eilers AC. 2019. *Ap. J. Lett.* 884:L19
- De Rosa G, Decarli R, Walter F, et al. 2011. *Ap. J.* 739(2):56
- De Rosa G, Venemans BP, Decarli R, et al. 2014. *Ap. J.* 790(2):145
- Decarli R, Dottì M, Bañados E, et al. 2019a. *Ap. J.* 880(2):157
- Decarli R, Mignoli M, Gilli R, et al. 2019b. *Astron. Astrophys.* 631:L10
- Decarli R, Pensabene A, Venemans B, et al. 2022. *Astron. Astrophys.* 662:A60
- Decarli R, Walter F, Venemans BP, et al. 2017. *Nature* 545(7655):457–61
- Decarli R, Walter F, Venemans BP, et al. 2018. *Ap. J.* 854(2):97
- Decarli R, Walter F, Yang Y, et al. 2012. *Ap. J.* 756(2):150
- DESI Collab., Abareshi B, Aguilar J, et al. 2022. *Astron. J.* 164:207
- Di Matteo T, Croft RAC, Feng Y, Waters D, Wilkins S. 2017. *MNRAS* 467(4):4243–51
- Diamond-Stanic AM, Fan X, Brandt WN, et al. 2009. *Ap. J.* 699:782–99
- D’Odorico V, Cupani G, Cristiani S, et al. 2013. *MNRAS* 435(2):1198–232
- D’Odorico V, Feruglio C, Ferrara A, et al. 2018. *Ap. J. Lett.* 863(2):L29
- Drake AB, Farina EP, Neeleman M, et al. 2019. *Ap. J.* 881(2):131
- Drake AB, Neeleman M, Venemans BP, et al. 2022. *Ap. J.* 929:86
- Duras F, Bongiorno A, Ricci F, et al. 2020. *Astron. Astrophys.* 636:A73
- Đurovčíková D, Katz H, Bosman SEI, et al. 2020. *MNRAS* 493(3):4256–75
- Eddington AS. 1926. *Nature* 106:14–20
- Eilers AC, Davies FB, Hennawi JF. 2018. *Ap. J.* 864:53
- Eilers AC, Davies FB, Hennawi JF, et al. 2017. *Ap. J.* 840:24
- Eilers AC, Hennawi JF, Davies FB, Simcoe RA. 2021. *Ap. J.* 917:38
- Eilers AC, Hennawi JF, Decarli R, et al. 2020. *Ap. J.* 900:37
- Endsley R, Stark DP, Lyu J, et al. 2022. *MNRAS* 520(3):4609–20
- Fabian AC. 2012. *Annu. Rev. Astron. Astrophys.* 50:455–89
- Fabian AC, Walker SA, Celotti A, et al. 2014. *MNRAS* 442:L81–84
- Fan X. 1999. *Astron. J.* 117(5):2528–51
- Fan X, Barth A, Banados E, et al. 2019a. *Bull. Am. Astron. Soc.* 51(3):121

Fan X, Carilli CL, Keating B. 2006a. *Annu. Rev. Astron. Astrophys.* 44:415–62  
 Fan X, Hennawi JF, Richards GT, et al. 2004. *Astron. J.* 128(2):515–22  
 Fan X, Narayanan VK, Lupton RH, et al. 2001. *Astron. J.* 122(6):2833–49  
 Fan X, Strauss MA, Becker RH, et al. 2006b. *Astron. J.* 132:117–36  
 Fan X, Strauss MA, Schneider DP, et al. 1999. *Astron. J.* 118:1–13  
 Fan X, Wang F, Yang J, et al. 2019b. *Ap. J. Lett.* 870(2):L11  
 Farina EP, Arrigoni-Battaia F, Costa T, et al. 2019. *Ap. J.* 887(2):196  
 Farina EP, Schindler JT, Walter F, et al. 2022. *Ap. J.* 941:106  
 Finkelstein SL, Bagley MB. 2022. *Ap. J.* 938:25  
 Finkelstein SL, D’Aloisio A, Paardekooper JP, et al. 2019. *Ap. J.* 879:36  
 Finlator K, Keating L, Oppenheimer BD, Davé R, Zackrisson E. 2018. *MNRAS* 480(2):2628–49  
 Fumigalli M, O’Meara JM, Prochaska JX, Worseck G. 2013. *Ap. J.* 775:78  
 Gaikwad P, Rauch M, Haehnelt MG, et al. 2020. *MNRAS* 494(4):5091–109  
 Gallerani S, Ferrara A, Neri R, Maiolino R. 2014. *MNRAS* 445(3):2848–53  
 Garaldi E, Gnedin NY, Madau P. 2019. *Ap. J.* 876:31  
 Ghisellini G, Celotti A, Tavecchio F, Haardt F, Sbarrato T. 2014. *MNRAS* 438(3):2694–700  
 Giallongo E, Grazian A, Fiore F, et al. 2019. *Ap. J.* 884:19  
 Gloude-mans AJ, Duncan KJ, Röttgering HJA, et al. 2021. *Astron. Astrophys.* 656:A137  
 Gnedin NY, Madau P. 2022. *Living Rev. Comput. Astrophys.* 8:3  
 Goto T, Utsumi Y, Furusawa H, Miyazaki S, Komiyama Y. 2009. *MNRAS* 400(2):843–50  
 Greig B, Mesinger A, Bañados E. 2019. *MNRAS* 484(4):5094–101  
 Greig B, Mesinger A, Davies FB, et al. 2022. *MNRAS* 512(4):5390–403  
 Greig B, Mesinger A, Haiman Z, Simcoe RA. 2017. *MNRAS* 466(4):4239–49  
 Gunn JE, Peterson BA. 1965. *Ap. J.* 142:1633–36  
 Habouzit M, Onoue M, Bañados E, et al. 2022. *MNRAS* 511(3):3751–67  
 Haiman Z, Rees MJ. 2001. *Ap. J.* 556:87–92  
 Hashimoto T, Inoue AK, Tamura Y, et al. 2019. *Publ. Astron. Soc. Jpn.* 71(6):109  
 Herrera-Camus R, Sturm E, Graciá-Carpio J, et al. 2020. *Astron. Astrophys.* 633:L4  
 Hewett PC, Warren SJ, Leggett SK, Hodgkin ST. 2006. *MNRAS* 367(2):454–68  
 Hopkins PF, Richards GT, Hernquist L. 2007. *Ap. J.* 654(2):731–53  
 Huang KW, Di Matteo T, Bhowmick AK, Feng Y, Ma CP. 2018. *MNRAS* 478(4):5063–73  
 Ighina L, Moretti A, Tavecchio F, et al. 2022. *Astron. Astrophys.* 659:A93  
 Inayoshi K, Visbal E, Haiman Z. 2020. *Annu. Rev. Astron. Astrophys.* 58:27–97  
 Ishimoto R, Kashikawa N, Kashino D, et al. 2022. *MNRAS* 515(4):5914–26  
 Ivezić Ž, Kahn SM, Tyson JA, et al. 2019. *Ap. J.* 873(2):111  
 Iwamuro F, Kimura M, Eto S, et al. 2004. *Ap. J.* 614:69–74  
 Iwamuro F, Motohara K, Maihara T, et al. 2002. *Ap. J.* 565:63–77  
 Izumi T, Matsuoka Y, Fujimoto S, et al. 2021. *Ap. J.* 914:36  
 Izumi T, Onoue M, Matsuoka Y, et al. 2019. *Publ. Astron. Soc. Jpn.* 71(6):111  
 Izumi T, Onoue M, Shirakata H, et al. 2018. *Publ. Astron. Soc. Jpn.* 70(3):36  
 Jiang L, Fan X, Bian F, et al. 2009. *Astron. J.* 138:305–11  
 Jiang L, Fan X, Brandt WN, et al. 2010. *Nature* 464(7287):380–83  
 Jiang L, Fan X, Hines DC, et al. 2006. *Astron. J.* 132(5):2127–34  
 Jiang L, Fan X, Vestergaard M, et al. 2007. *Astron. J.* 134(3):1150–61  
 Jiang L, McGreer ID, Fan X, et al. 2016. *Ap. J.* 833(2):222  
 Jiang L, Ning Y, Fan X, et al. 2022. *Nature Astronomy* 6:850–56  
 Jin X, Yang J, Fan X, et al. 2023. *Ap. J.* 942(2):59  
 Jolley EJD, Kuncic Z. 2008. *MNRAS* 386(2):989–94  
 Just DW, Brandt WN, Shemmer O, et al. 2007. *Ap. J.* 665(2):1004–22  
 Kato N, Matsuoka Y, Onoue M, et al. 2020. *Publ. Astron. Soc. Jpn.* 72(5):84  
 Kaviraj S, Laigle C, Kimm T, et al. 2017. *MNRAS* 467(4):4739–52  
 Keating LC, Haehnelt MG, Cantalupo S, Puchwein E. 2015. *MNRAS* 454:681–97

- Keating LC, Puchwein E, Haehnelt MG, Bird S, Bolton JS. 2016. *MNRAS* 461:606–26
- Khusanova Y, Bañados E, Mazzucchelli C, et al. 2022. *Astron. Astrophys.* 664:A39
- Kim S, Stiavelli M, Trenti M, et al. 2009. *Ap. J.* 695(2):809–17
- Kormendy J, Ho LC. 2013. *Annu. Rev. Astron. Astrophys.* 51:511–653
- Kulkarni G, Keating LC, Haehnelt MG. 2019a. *MNRAS* 485:L24–28
- Kulkarni G, Worseck G, Hennawi JF. 2019b. *MNRAS* 488:1035–65
- Kurk JD, Walter F, Fan X, et al. 2007. *Ap. J.* 669:32–44
- Lai S, Bian F, Onken CA, et al. 2022. *MNRAS* 513(2):1801–19
- Lang D, Hogg DW, Jester S, Rix HW. 2009. *Astron. J.* 137(5):4400–11
- Lawrence A, Warren SJ, Almaini O, et al. 2007. *MNRAS* 379(4):1599–617
- Leipski C, Meisenheimer K, Walter F, et al. 2014. *Ap. J.* 785(2):154
- Li J, Silverman JD, Izumi T, et al. 2022a. *Ap. J. Lett.* 931:L11
- Li J, Venemans BP, Walter F, et al. 2022b. *Ap. J.* 930:27
- Li J, Wang R, Cox P, et al. 2020. *Ap. J.* 900(2):131
- Liu B, Bordoloi R. 2021. *MNRAS* 502(3):3510–32
- Liu Y, Wang R, Momjian E, et al. 2021. *Ap. J.* 908(2):124
- Lusso E, Fumagalli M, Rafelski M, et al. 2018. *Ap. J.* 860:41
- Lyu J, Rieke G. 2022. *Universe* 8(6):304
- Lyu J, Rieke GH, Shi Y. 2017. *Ap. J.* 835(2):257
- Maiolino R, Cox P, Caselli P, et al. 2005. *Astron. Astrophys.* 440(2):L51–54
- Maiolino R, Gallerani S, Neri R, et al. 2012. *MNRAS* 425:L66–70
- Maiolino R, Juarez Y, Mujica R, Nagar NM, Oliva E. 2003. *Ap. J.* 596(2):L155–58
- Maiolino R, Schneider R, Oliva E, et al. 2004. *Nature* 431(7008):533–35
- Marshall MA, Mechtley M, Windhorst RA, et al. 2020. *Ap. J.* 900:21
- Marshall MA, Wyithe JSB, Windhorst RA, et al. 2021. *MNRAS* 506:1209–28
- Martocchia S, Piconcelli E, Zappacosta L, et al. 2017. *Astron. Astrophys.* 608:A51
- Matejek MS, Simcoe RA. 2012. *Ap. J.* 761(2):112
- Matsuoka Y, Iwasawa K, Onoue M, et al. 2019a. *Ap. J.* 883(2):183
- Matsuoka Y, Iwasawa K, Onoue M, et al. 2022. *Ap. J. Suppl. Ser.* 259:18
- Matsuoka Y, Onoue M, Kashikawa N, et al. 2016. *Ap. J.* 828:26
- Matsuoka Y, Onoue M, Kashikawa N, et al. 2019b. *Ap. J. Lett.* 872:L2
- Matsuoka Y, Strauss MA, Kashikawa N, et al. 2018. *Ap. J.* 869(2):150
- Mazzucchelli C, Bañados E, Decarli R, et al. 2017a. *Ap. J.* 834:83
- Mazzucchelli C, Bañados E, Venemans BP, et al. 2017b. *Ap. J.* 849(2):91
- Mazzucchelli C, Decarli R, Farina EP, et al. 2019. *Ap. J.* 881(2):163
- McGreer ID, Becker RH, Helfand DJ, White RL. 2006. *Ap. J.* 652:157–62
- McGreer ID, Jiang L, Fan X, et al. 2013. *Ap. J.* 768(2):105
- McGreer ID, Mesinger A, D’Odorico V. 2015. *MNRAS* 447:499–505
- McGreer ID, Mesinger A, Fan X. 2011. *MNRAS* 415(4):3237–46
- McQuinn M. 2016. *Annu. Rev. Astron. Astrophys.* 54:313–62
- Mechtley M, Windhorst RA, Ryan RE, et al. 2012. *Ap. J. Lett.* 756(2):L38
- Meja-Restrepo JE, Trakhtenbrot B, Lira P, Netzer H. 2018. *MNRAS* 478(2):1929–41
- Merloni A. 2019. In *The Messenger: Preparing for 4MOST. A Community Workshop Introducing ESO’s Next-Generation Spectroscopic Survey Facility*, Garching b. München, Germ., May 6–8, id. 23
- Mesinger A, Haiman Z. 2004. *Ap. J. Lett.* 611(2):L69–72
- Meyer RA, Bosman SEI, Ellis RS. 2019. *MNRAS* 487(3):3305–23
- Meyer RA, Decarli R, Walter F, et al. 2022a. *Ap. J.* 927(2):141
- Meyer RA, Walter F, Cicone C, et al. 2022b. *Ap. J.* 927(2):152
- Mignoli M, Gilli R, Decarli R, et al. 2020. *Astron. Astrophys.* 642:L1
- Miralda-Escudé J. 1998. *Ap. J.* 501:15–22
- Momjian E, Carilli CL, Bañados E, Walter F, Venemans BP. 2018. *Ap. J.* 861(2):86
- Momose R, Goto T, Utsumi Y, et al. 2019. *MNRAS* 488:120–34

Morey KA, Eilers AC, Davies FB, Hennawi JF, Simcoe RA. 2021. *Ap. J.* 921:88  
 Morselli L, Mignoli M, Gilli R, et al. 2014. *Astron. Astrophys.* 568:A1  
 Mortlock D. 2016. In *Understanding the Epoch of Cosmic Reionization: Challenges and Progress*, ed. A Mesinger. *Ap. Space Sci. Libr.* 423:187–226. Cham, Switz.: Springer  
 Mortlock DJ, Patel M, Warren SJ, et al. 2012. *MNRAS* 419:390–410  
 Mortlock DJ, Warren SJ, Venemans BP, et al. 2011. *Nature* 474(7353):616–19  
 Murdoch HS, Hunstead RW, Pettini M, Blades JC. 1986. *Ap. J.* 309:19–32  
 Naidu RP, Tacchella S, Mason CA et al. 2020. *Ap. J.* 892(2):109  
 Nanni R, Hennawi JF, Wang F, et al. 2022. *MNRAS* 515(3):3224–48  
 Nanni R, Vignali C, Gilli R, Moretti A, Brandt WN. 2017. *Astron. Astrophys.* 603:A128  
 Neeleman M, Bañados E, Walter F, et al. 2019. *Ap. J.* 882:10  
 Neeleman M, Novak M, Venemans BP, et al. 2021. *Ap. J.* 911(2):141  
 Ni Y, Di Matteo T, Gilli R, et al. 2020. *MNRAS* 495(2):2135–51  
 Novak M, Bañados E, Decarli R, et al. 2019. *Ap. J.* 881:63  
 Novak M, Venemans BP, Walter F, et al. 2020. *Ap. J.* 904(2):131  
 O’Meara M, Prochaska E, Worseck C, et al. 2013. *Ap. J.* 765(2):137  
 Onoue M, Bañados E, Mazzucchelli C, et al. 2020. *Ap. J.* 898(2):105  
 Onoue M, Kashikawa N, Matsuoka Y, et al. 2019. *Ap. J.* 880(2):77  
 Osmer PS. 1982. *Ap. J.* 253:28–37  
 Overzier RA. 2022. *Ap. J.* 926(2):114  
 Overzier RA, Guo Q, Kauffmann G, et al. 2009. *MNRAS* 394(2):577–94  
 Pacucci F, Loeb A. 2022. *MNRAS* 509(2):1885–91  
 Park D, Barth AJ, Woo JH, et al. 2017. *Ap. J.* 839(2):93  
 Park D, Woo JH, Treu T, et al. 2012. *Ap. J.* 747:30  
 Pensabene A, Decarli R, Bañados E, et al. 2021. *Astron. Astrophys.* 652:A66  
 Pensabene A, van der Werf P, Decarli R, et al. 2022. *Astron. Astrophys.* 667:A9  
 Pentericci L, Fan X, Rix HW, et al. 2002. *Astron. J.* 123(5):2151–58  
 Peterson BM, Ferrarese L, Gilbert KM, et al. 2004. *Ap. J.* 613(2):682–99  
 Planck Collab., Aghanim N, Akrami Y, et al. 2020. *Astron. Astrophys.* 641:A6  
 Plotkin RM, Shemmer O, Trakhtenbrot B, et al. 2015. *Ap. J.* 805(2):123  
 Pons E, McMahon RG, Banerji M, Reed SL. 2020. *MNRAS* 491(3):3884–90  
 Prochaska JX, Hennawi JF, Herbert-Fort S. 2008. *Ap. J.* 675(2):1002–13  
 Prochaska JX, Worseck G, O’Meara JM. 2009. *Ap. J. Lett.* 705(2):L113–17  
 Rauch M, Miralda-Escudé J, Sargent WLW, et al. 1997. *Ap. J.* 489:7–20  
 Reed SL, McMahon RG, Martini P, et al. 2017. *MNRAS* 468(4):4702–18  
 Ren K, Trenti M, Marshall MA, Di Matteo T, Ni Y. 2021. *Ap. J.* 917(2):89  
 Richards GT, Fan X, Newberg HJ, et al. 2002. *Astron. J.* 123(6):2945–75  
 Richards GT, Kruczek NE, Gallagher SC, et al. 2011. *Astron. J.* 141(5):167  
 Richards GT, Lacy M, Storr-Lombardi LJ, et al. 2006a. *Ap. J. Suppl. Ser.* 166(2):470–97  
 Richards GT, Strauss MA, Fan X, et al. 2006b. *Astron. J.* 131(6):2766–87  
 Robertson BE. 2021. *Annu. Rev. Astron. Astrophys.* 60:121–58  
 Robertson BE, Ellis RS, Furlanetto SR, Dunlop JS. 2015. *Ap. J. Lett.* 802(2):L19  
 Roche N, Humphrey A, Binette L. 2014. *MNRAS* 443(4):3795–808  
 Rojas-Ruiz S, Bañados E, Neeleman M, et al. 2021. *Ap. J.* 920(2):150  
 Rorai A, Hennawi JF, Oñorbe J, et al. 2017. *Science* 356(6336):418–22  
 Runnoe JC, Brotherton MS, Shang Z. 2012. *MNRAS* 422:478–93  
 Ryan-Weber EV, Pettini M, Madau P. 2006. *MNRAS* 371:L78–82  
 Scaramella R, Amiaux J, Mellier Y, et al. 2022. *Astron. Astrophys.* 662:A112  
 Schindler JT, Bañados E, Connor T, et al. 2023. *Ap. J.* 943:67  
 Schindler JT, Farina EP, Bañados E, et al. 2020. *Ap. J.* 905:51  
 Schmidt M. 1963. *Nature* 197(4872):1040  
 Schmidt M. 1968. *Ap. J.* 151:393–410

Schmidt M, Schneider DP, Gunn JE. 1995. *Astron. J.* 110:68–77

Schneider DP, Schmidt M, Gunn JE. 1989. *Astron. J.* 98:1951–59

Schneider DP, Schmidt M, Gunn JE. 1999. *Astron. J.* 117:40–55

Shao Y, Wang R, Jones GC, et al. 2017. *Ap. J.* 845(2):138

Shen X, Hopkins PF, Faucher-Giguère CA, et al. 2020. *MNRAS* 495(3):3252–75

Shen Y, Richards GT, Strauss MA, et al. 2011. *Ap. J. Suppl. Ser.* 194(2):45

Shen Y, Wu J, Jiang L, et al. 2019. *Ap. J.* 873:35

Simcoe RA. 2006. *Ap. J.* 653(2):977–87

Simcoe RA, Cooksey KL, Matejek M, et al. 2011. *Ap. J.* 743:21

Simcoe RA, Sullivan PW, Cooksey KL, et al. 2012. *Nature* 492(7427):79–82

Simpson C, Mortlock D, Warren S, et al. 2014. *MNRAS* 442(4):3454–61

Stark DP. 2016. *Annu. Rev. Astron. Astrophys.* 54:761–803

Stern J, Hennawi JF, Prochaska JX, Werk JK. 2016. *Ap. J.* 830(2):87

Stiavelli M, Djorgovski SG, Pavlovsky C, et al. 2005. *Ap. J. Lett.* 622:L1–4

Temple MJ, Hewett PC, Banerji M. 2021. *MNRAS* 508:737–54

Trakhtenbrot B, Netzer H. 2012. *MNRAS* 427(4):3081–102

Utsumi Y, Goto T, Kashikawa N, et al. 2010. *Ap. J.* 721(2):1680–88

Vanden Berk DE, Richards GT, Bauer A, et al. 2001. *Astron. J.* 122(2):549–64

Veilleux S, Maiolino R, Bolatto AD, Aalto S. 2020. *Astron. Astrophys. Rev.* 28:2

Venemans BP, Decarli R, Walter F, et al. 2018. *Ap. J.* 866(2):159

Venemans BP, Findlay JR, Sutherland WJ, et al. 2013. *Ap. J.* 779:24

Venemans BP, Neeleman M, Walter F, et al. 2019. *Ap. J. Lett.* 874(2):L30

Venemans BP, Walter F, Decarli R, et al. 2017a. *Ap. J.* 837(2):146

Venemans BP, Walter F, Decarli R, et al. 2017b. *Ap. J.* 845(2):154

Venemans BP, Walter F, Neeleman M, et al. 2020. *Ap. J.* 904(2):130

Vestergaard M, Osmer PS. 2009. *Ap. J.* 699:800–16

Vito F, Brandt WN, Bauer FE, et al. 2019a. *Astron. Astrophys.* 628:L6

Vito F, Brandt WN, Bauer FE, et al. 2019b. *Astron. Astrophys.* 630:A118

Vito F, Brandt WN, Ricci F, et al. 2021. *Astron. Astrophys.* 649:A133

Volonteri M. 2010. *Astron. Astrophys. Rev.* 18(3):279–315

Volonteri M, Stark DP. 2011. *MNRAS* 417(3):2085–93

Wagenveld JD, Saxena A, Duncan KJ, Röttgering HJA, Zhang M. 2022. *Astron. Astrophys.* 660:A22

Walter F, Bertoldi F, Carilli C, et al. 2003. *Nature* 424(6947):406–8

Walter F, Neeleman M, Decarli R, et al. 2022. *Ap. J.* 927:21

Walter F, Riechers D, Novak M, et al. 2018. *Ap. J. Lett.* 869(2):L22

Walther M, Oñorbe J, Hennawi JF, Lukić Z. 2019. *Ap. J.* 872:13

Wang F, Davies FB, Yang J, et al. 2020. *Ap. J.* 896:23

Wang F, Fan X, Yang J, et al. 2017. *Ap. J.* 839:27

Wang F, Fan X, Yang J, et al. 2021a. *Ap. J.* 908:53

Wang F, Yang J, Fan X, et al. 2018. *Ap. J. Lett.* 869:L9

Wang F, Yang J, Fan X, et al. 2019. *Ap. J.* 884:30

Wang F, Yang J, Fan X, et al. 2021b. *Ap. J. Lett.* 907:L1

Wang R, Carilli CL, Beelen A, et al. 2007. *Astron. J.* 134(2):617–27

Wang R, Carilli CL, Neri R, et al. 2010. *Ap. J.* 714:699–712

Wang R, Carilli CL, Wagg J, et al. 2008. *Ap. J.* 687(2):848–58

Wang R, Wagg J, Carilli CL, et al. 2013. *Ap. J.* 773:44

Wang R, Wu XB, Neri R, et al. 2016. *Ap. J.* 830:53

Warren SJ, Hewett PC, Irwin MJ, McMahon RG, Bridgeland MT. 1987. *Nature* 325(6100):131–33

Wenzl L, Schindler JT, Fan X, et al. 2021. *Astron. J.* 162(2):72

Willott CJ, Bergeron J, Omont A. 2017. *Ap. J.* 850:108

Willott CJ, Chet S, Bergeron J, Hutchings JB. 2011. *Astron. J.* 142(6):186

Willott CJ, Delorme P, Reylé C, et al. 2010. *Astron. J.* 139(3):906–18

Willott CJ, McLure RJ, Jarvis MJ. 2003. *Ap. J. Lett.* 587:L15–18  
Willott CJ, Omont A, Bergeron J. 2013. *Ap. J.* 770:13  
Wolf J, Nandra K, Salvato M, et al. 2021. *Astron. Astrophys.* 647:A5  
Wolfire MG, Vallini L, Chevance M. 2022. *Annu. Rev. Astron. Astrophys.* 60:247–318  
Worseck G, Prochaska JX, O’Meara JM. 2014. *MNRAS* 445(2):1745–60  
Wright EL, Eisenhardt PRM, Mainzer AK, et al. 2010. *Astron. J.* 140(6):1868–81  
Wu XB, Wang F, Fan X, et al. 2015. *Nature* 518(7540):512–15  
Yang J, Venemans B, Wang F, et al. 2019a. *Ap. J.* 880(2):153  
Yang J, Wang F, Fan X, et al. 2019b. *Astron. J.* 157(6):236  
Yang J, Wang F, Fan X, et al. 2020a. *Ap. J.* 904:26  
Yang J, Wang F, Fan X, et al. 2020b. *Ap. J. Lett.* 897:L14  
Yang J, Wang F, Fan X, et al. 2021. *Ap. J.* 923(2):262  
York DG, Adelman J, Anderson JE Jr., et al. 2000. *Astron. J.* 120(3):1579–87  
Yue M, Fan X, Yang J, Wang F. 2021a. *Ap. J. Lett.* 921(2):L27  
Yue M, Yang J, Fan X, et al. 2021b. *Ap. J.* 917(2):99  
Zeimann GR, White RL, Becker RH, et al. 2011. *Ap. J.* 736:57  
Zheng W, Overzier RA, Bouwens RJ, et al. 2006. *Ap. J.* 640(2):574–78  
Zhu Y, Becker GD, Bosman SEI, et al. 2021. *Ap. J.* 923(2):223  
Zhu Y, Becker GD, Bosman SEI, et al. 2022. *Ap. J.* 923(2):76